Unravelling Charge Storage and Degradation in Cathodes for Rechargeable Aluminium Batteries: A Synergistic Study of CoSe Cathodes and MXenes-Based Components

Zur Erlangung des akademischen Grades einer

DOKTORIN DER NATURWISSENSCHAFTEN

(Dr. rer. nat.)

von der KIT-Fakultät für Chemie und Biowissenschaften
des Karlsruher Instituts für Technologie (KIT)

genehmigte

Dissertation

von

Eliana Carolina Fuentes Mendoza M.Sc

Tag der mündlichen Prüfung: 19. Dezember 2025

1. Referent: Prof. Dr. rer. Nat. Helmut Ehrenberg

2. Referentin: Prof. Dr. Sonia Dsoke

Kurzfassung

Diese Dissertation präsentiert eine umfassende Untersuchung des elektrochemischen Verhaltens und der Degradationsmechanismen von Kobaltselenid-(CoSe)-Kathoden in wiederaufladbaren Aluminiumbatterien. Es wurde ein multifunktionaler Ansatz angewendet, der elektrochemische Tests, *ex situ*-Analysen sowie fortgeschrittene *in situ*- und *operando* -Charakterisierungstechniken auf Synchrotronbasis kombiniert.

Die Studie schließt kritische Wissenslücken in der Literatur und zeigt eine anfängliche Amorphisierung von CoSe sowie eine Phasenumwandlung von hexagonalem CoSe zu kubischem $CoSe_2$, begleitet von der Auflösung von $Co(AlCl_4)_2$, das migriert und sich auf der Aluminium-Anode abscheidet. Die Ladungsspeicherung erfolgt über die reversible Redoxreaktion von Se^{2-} zu Se^{-}, während Co^{2+} elektrochemisch inaktiv bleibt. Die Auflösung und Abscheidung von $Co(AlCl_4)_2$ tragen durch den Verlust aktiven Materials und die Kontamination der Anode zum Kapazitätsverlust bei, wie durch *ex situ*-SEM-EDX- und ICP-OES-Analysen bestätigt wurde.

Zur Untersuchung der in CoSe identifizierten Degradationspfade wird im zweiten Teil dieser Arbeit die multifunktionale Rolle von $Ti_3C_2T_X$ als passive Komponente untersucht. Die geschichtete Struktur der $Ti_3C_2T_X$-MXene wurde zunächst ausgewählt, um Separatoren zu modifizieren, da sie das Potenzial besitzt, den Transport gelöster Spezies zu unterdrücken. Aufgrund ihrer überzeugenden physikochemischen Eigenschaften, wie hoher Leitfähigkeit, einstellbarer Oberflächenchemie und mechanischer Stabilität, wurde $Ti_3C_2T_X$ weiter hinsichtlich seiner Rolle bei der Verbesserung der Leistung von Kathoden für RABs untersucht. $Ti_3C_2T_X$ wurde als Stromableiter und Separatoradditiv evaluiert, mit dem Ziel, die Elektrodenintegrität und Leitfähigkeit zu verbessern und den Verlust aktiver Materialien zu verringern. Obwohl $Ti_3C_2T_X$ -basierte Separatoren eine leichte Reduktion des Kobalt-Shuttlings zeigen, reicht dies nicht aus, um die Migration vollständig zu unterdrücken, was die Bedeutung einer zukünftigen Optimierung des Separator-Designs hervorhebt.

Dieser integrierte Ansatz unterstreicht die Bedeutung des Verständnisses sowohl der Mechanismen aktiver Materialien als auch der Wechselwirkungen passiver Komponenten, um die Leistungsfähigkeit und Stabilität chalcogenidbasierter Elektroden für RABs zu verbessern. Die Ergebnisse etablieren ein mechanistisches Rahmenkonzept, das die Grundlage für andere Übergangsmetall-Chalkogenid-Chemien legt und zukünftige Strategien zur Unterdrückung von Degradationsprozessen sowie zur Entwicklung langlebiger, leistungsstarker wiederaufladbarer Aluminiumbatterien aufzeigt.

Selbständigkeitserklärung

Hiermit versichere ich, dass ich die vorliegende Arbeit selbstständig verfasst habe, dass ich keine anderen als die angegebenen Quellen und Hilfsmittel benutzt habe, dass ich die wörtlich oder inhaltlich übernommenen Stellen als solche gekennzeichnet habe und, dass ich die Satzung des KIT zur Sicherung guter wissenschaftlicher Praxis in der jeweils gültigen Fassung beachtet habe.

Karlsruhe den 04 Januar 2026

Eliana Carolina Fuentes Mendoza

Acknowledgment

I would like to express my deepest gratitude to Prof. Helmut Ehrenberg and Prof. Sonia Dsoke for giving me the opportunity to pursue my PhD at IAM-ESS, for their valuable scientific guidance, and for their relentless effort to help make this research the best possible version of itself.

My sincere thanks go to Dr. Fabian Jeschull for his time, effort, and insightful discussions of my results. Thank you for helping me make sense of the system and for giving another chance to RABs.

I am also immensely grateful to Prof. Yury Gogotsi and the DNI group at Drexel University for hosting me as a visiting researcher for three months. Learning about the versatility and infinite possibilities of MXenes was both stimulating and deeply motivating.

This work would not have been possible without the support of the staff members and colleagues at IAM-ESS, especially Dr. Angelina Sarapulova, whose collaboration went far beyond professional commitment and who continued helping me even after I changed institutes; my HIWI Amirhossein Dorosti, whose indispensable work made achieving results possible, I could not have asked for a better right hand; Dr. Ramon Zimmermann, Dennis Triller, Dr. Eugen Zemlyanushin, Liuda Mereacre, Björn Schwarz, and many others for their invaluable help and insightful discussions.

I am particularly grateful to Dr. Mahla Talari and Dr. Noha Sabi for welcoming, guiding, and supporting me during my first years. I was incredibly lucky to have you in my workplace, and I am even happier to have you in my life after this journey, thank you for all the happiness.

On a personal note, this would not have been possible without the support of the Estrada Fuentes family. Diego and Lili, thank you for bringing into this world the cutest little person, mi bebota, Alana, who gives me reasons and motivation to succeed and be happy.

I am deeply grateful to my sisters Lili and Nata, who always asked how the thesis was going and kept motivating me even when they didn't understand what I was doing. *Las amo!* I will always be thankful to my mother, Meredith, for her immense love. I can feel it even when I can't see you, and everything I do is to make you proud. *Te adoro, Peshoshura de Madre.*

To all my friends: I am so lucky that I can't name all of you, because it would make this unreadable, but every conversation, every coffee, every motivational word was exactly what I needed to get through this experience.

To Santiago Estrada, and Leticia Cobo, thank you for your help in diagnosing and treating my ADHD, without you, this would have been impossible. To Sharloth Diaz, for helping me heal and cope with all the stress and dealing with all the meltdowns, you are the best!

Lastly, I have to leave my future husband for last because there will never be enough space to express all my gratitude. Thank you to my fiancé, Dr. Nicholas Jobbitt, for saving my sanity, for your love and kindness, for proofreading my papers and thesis, for your constructive criticism of my "ugly plots" and your gorgeous Python-improved versions, and for your millimetric eye for scientific detail. I would have never dared to dream of such help. Thank you for your supportive words, for giving me perspective and reminding me that this too shall pass, and for dealing with all the sadness and frustration. Thank you for loving the saddest version of me, even when I couldn't love myself. I look forward to growing old by your side. *Te amo, mi Cielo*.

Abstract

This dissertation presents a comprehensive investigation of the electrochemical behaviour and degradation mechanisms of cobalt selenide (CoSe) cathodes in rechargeable aluminium batteries. A multifaceted approach was employed, combining electrochemical testing, *ex situ* analysis, and advanced *in situ,* and *operando* synchrotron-based characterisation techniques.

The study addresses critical knowledge gaps in literature, revealing an initial amorphisation of CoSe and phase transition from hexagonal CoSe to cubic $CoSe_2$, accompanied by dissolution of $Co(AlCl_4)_2$ that migrate and deposit on the Al anode. The charge storage occurs at the CoSe amorphous lattice by the reversible redox reaction of Se^{2-} to Se^{1} while Co^{2+} remains electrochemically inactive. The dissolution and deposition of $Co(AlCl_4)_2$ contribute to capacity fade by loss of active material and anode contamination, as confirmed by *ex situ* SEM-EDX and ICP-OES analyses.

To address the degradation pathways identified in CoSe, the second part of this work investigates the multifunctional role of $Ti_3C_2T_X$ as passive components. The layered structure of $Ti_3C_2T_X$ MXenes was initially selected to modify separators due to its potential to suppress the shuttling of dissolved species. Its compelling physicochemical properties, such as high conductivity, tuneable surface chemistry, and mechanical stability, prompted further investigation into its role in improving the performance of cathodes for RABs. $Ti_3C_2T_X$ was evaluated as current collector and separator additives, with the aim of improving electrode integrity, conductivity, and mitigating active material loss. While $Ti_3C_2T_X$-based separators show slight reductions in $Co(AlCl_4)_2$ shuttling, it is not sufficient to suppress migration, highlighting importance of future optimisation of the separator design.

This integrated approach underscores the importance of understanding both active material mechanism and passive component interactions to enhance the performance and stability of chalcogenide-based electrodes for RABs. The findings establish a mechanistic framework laying the ground for other transition metal chalcogenides chemistries toward future strategies for suppressing degradation and enabling durable, high-performance rechargeable aluminium batteries.

Table of Content

List of Figures

List of Tables

Abbreviations

Al	Aluminium
$Al_2Cl_7^-$	Heptachloro-dialuminate anion
$AlCl_3$	Aluminium chloride
$AlCl_4^-$	Tetrachloroaluminate anion
BMImCl	1-butyl-3-methylimidazolium chloride
C Paper	Carbon paper
Ca	Calcium
CA	Chronoamperometry
Carr	Carrageenan
CEI	Cathode–electrolyte interphase
CNT	Carbon nanotubes
Co	Cobalt
CoSe	Cobalt selenide
$CoSe_2$	Cobalt diselenide
Cr_2N	Chromium nitride
$CrCl_3$	Chromium chloride
CV	Cyclic voltammetry
DI	Deionized
DTGA	Derivative thermogravimetric analysis
EIS	Electrochemical Impedance Spectroscopy
EMImCl	1-ethyl-3-methylimidazolium chloride
–F	Fluorine surface group
$FeCl_3$	Iron chloride
GCPL	Galvanostatic charge/discharge with potential limitation

HER	Hydrogen evolution reaction
ICP-OES	Inductively Coupled Plasma - Optical Emission Spectroscopy
ICSD	Inorganic Crystal Structure Database
IL	Ionic liquid
K	Potassium
Li	Lithium
LCO-$LiCoO_2$	Lithium cobalt oxide
LIBs	Lithium-ion batteries
LSV	Linear sweep voltammetry
Mg	Magnesium
Mo	Molybdenum
MOF	Metal-Organic Framework
Na	Sodium
Na Alg	Sodium alginate
NG	Natural graphite
Ni	Nickel
–O	Oxygen
OCV	Open circuit voltage
–OH	Hydroxyl surface group
PAN	Polyacrylonitrile
PEDOT	Poly(3,4-ethylenedioxythiophene)
PG	Pyrolytic graphite
PPMS	Physical Property Measurement System
PTFE	Poly(tetrafluoroethylene)
PVDF	Poly(vinylidene fluoride)
RABs	Rechargeable aluminium batteries
R_{ct}	Charge transfer resistance
Redox	Reduction and oxidation

R_{film}	Film resistance
R_s	Sheet resistance
RTILS	Room temperature ionic liquids
Se	Selenium
Se_2Cl_2	Selenium monochloride
SEM-EDX	Scanning Electron Microscopy and Energy-Dispersive X-ray
SRD	Synchrotron Radiation Diffraction
SS	Stainless steel
TGA	Thermogravimetric analysis
$Ti_3C_2T_X$	Titanium carbide MXenes
TiN	Titanium nitride
TiS_2	Titanium disulfide
W	Tungsten
XAS	X-Ray Absorption Spectroscopy
XRD	X-ray diffraction
Zn	Zinc
α	Coefficient of resistivity
ρ_0	Residual resistivity

Prologue: The Art of Unveiling Reality – A Scientific Investigation

We can't separate science from art because while science explains reality, art imitates it. This premise guides the journey illustrated in this thesis. Nowadays, scientists dive as deeply as possible into their fields, creating distance from the arts. However, if we look back on history, visionaries like Leonardo da Vinci demonstrated how closely these areas can work together. The combination of the rigorous, analytical, and objective approach of science with the intuitive and interpretive approach of art can lead to insights that neither discipline could achieve on its own, offering new perspectives and resonance.

The process of scientific research often mirrors the fascinating narratives found in crime literature. As stated by Hercule Poirot in Agatha Christie's The Murder of Roger Ackroyd, "The truth, however ugly in itself, is always beautiful in its setting, and to the scientific mind, an unsolved problem is a torment". For scientists, this torment fuels an incredible drive. It propels them through the identification of a research question or a scientific gap, the careful collection of clues, the formation of hypotheses about possible mechanisms, and the persistent pursuit of evidence to build a conclusive case. This rigorous process ultimately leads to not only professional but also personal satisfaction.

This thesis is more than a scientific investigation; it is a significant milestone in my intellectual journey, and as such, it also aims to reflect my scientific personality. Therefore, it presents a blend of rigorous scientific concepts and creative thinking. This approach is inspired by the historical arc of electrochemical research, from its early discoveries that inspired long-loved tales of creation, such as Frankenstein, to humanity's drive to understand and control natural forces.

Herein, we will collect our "leads", scrutinize our "suspects", and present our "evidence" to build a comprehensive case, aiming to unveil the complex charge storage and *degradation mechanisms within advanced battery materials, and explore innovative strategies for optimizing the overall battery cell.*

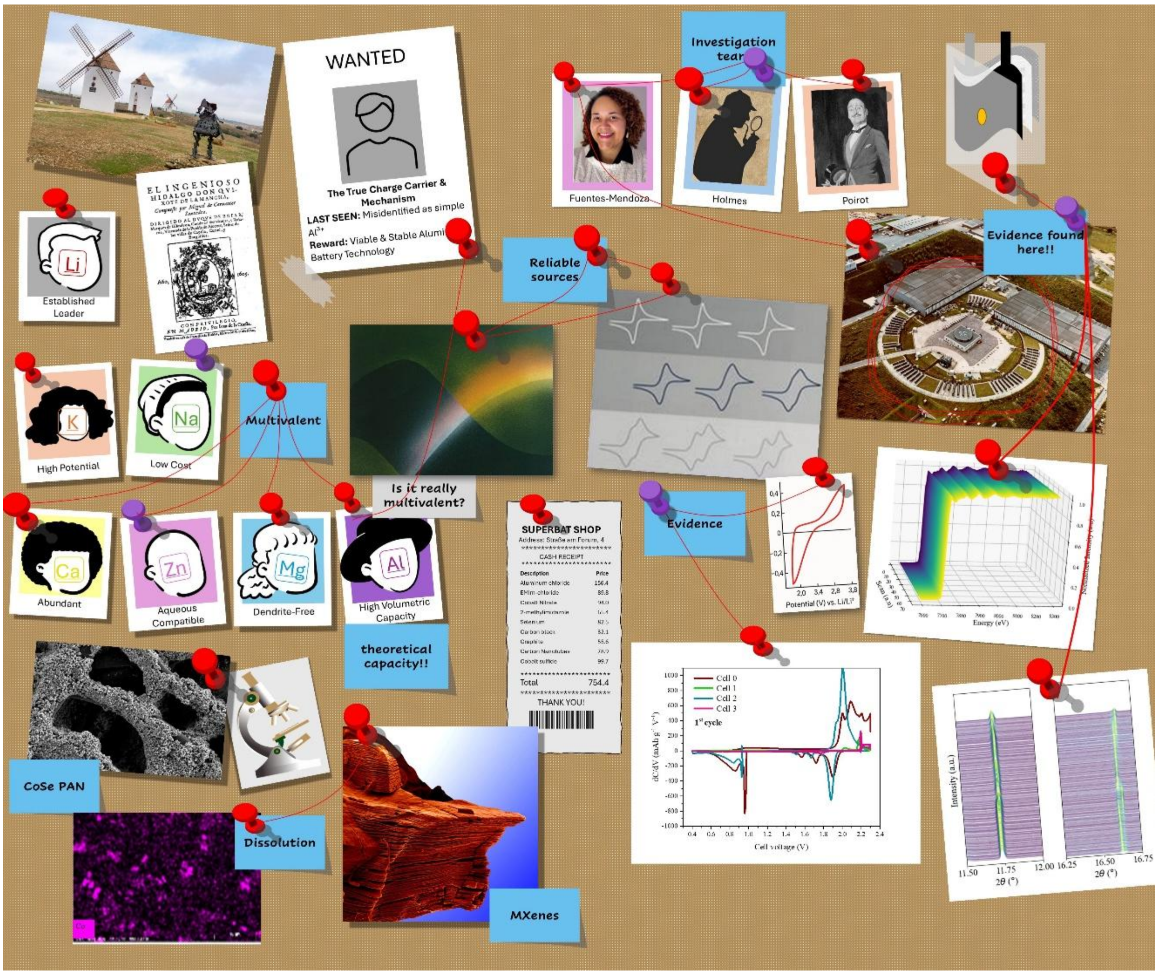

Unravelling Charge Storage and Degradation in Cathodes for Rechargeable Aluminium Batteries: A Synergistic Study of CoSe Cathodes and MXenes-Based Components

1 Introduction and Motivation: Toward Post-Lithium Storage

Have you noticed the growing number of homes equipped with solar panels, or the silent, monumental presence of wind turbines across the landscape? Don Quixote once mistook these colossal structures for giants and charged at them, but today we recognized them as vital allies in meeting the global effort to meet rising energy demands and combat climate change.

The scientific community stands at the forefront of this challenge, driven by the relentless increase in energy consumption, fuelled by ongoing industrialisation, post-pandemic recovery, population growth, and an increasingly consumerist lifestyle. This relentless demand, combined with the urgent need to reduce carbon emissions, has catalysed extensive scientific and technological efforts to revolutionize how we generate, distribute, and store energy.

The context for this research project is established by outlining the motivation for investigating rechargeable aluminium (Al) batteries (RABs) technology and defining the specific scientific questions addressed. This chapter is structured as follows:

- Section 1.1: Scientific motivation and the post-lithium (Li) vision.
- Section 1.2: Why aluminium? Abundance, safety and cost.
- Section 1.3: Research scope and hypotheses.

1.1 Scientific Motivation and the Post-Li Vision

The global energy sector faces pressure from a growing demand that often exceeds supply. This imbalance is particularly pronounced in regions experiencing chronic energy shortages, where blackouts disrupt daily life and essential services, as seen in the widespread outage across the Iberian Peninsula in April 2025. Reflecting on similar challenges in Beijing during the 1990s, physicist Yang Yang noted: “The power plants could not meet the high demand for electricity in the summer" [1]. To address such disruptions and their economic consequences, the energy industry is investing in advanced forecasting tools and infrastructure to better anticipate and manage fluctuations in energy consumption.

Renewable energy resources, characterized by their lower environmental impact and more equitable global distribution, have become central to energy transition strategies. Their growing adoption, driven by the urgent need for decarbonisation, has led to ambitious policy initiatives. For instance, Article 194 of the Treaty on the Functioning of the European Union mandates the member states to promote energy efficiency, savings, and the development of renewable forms of energy [2]. According to the International Energy Agency's 2023 report, renewable electricity generation is expected to increase by nearly 70% by 2028 compared to 2022, reaching approximately 14400 TWh [3].

Despite this progress, the intermittency and climate-dependence of renewable sources present significant challenges to grid stability. Energy storage systems are essential to overcoming these limitations, enabling consistent energy supply and cost optimisation by storing electricity during off-peak periods for use during peak demand [4].

Electrochemical energy storage systems, particularly Li-ion batteries (LIBs), have played a transformative role in portable electronics and are now pivotal to the energy transition. They offer high efficiency (70–90%), rapid response times, and scalability across applications [5]. However, their widespread application is limited by finite lifespans, degradation over charge-discharge cycles, and reliance on scarce and geopolitically sensitive materials such as lithium (Li) and cobalt (Co). These limitations raise concerns about long-term sustainability, cost, and environmental impact.

To address these challenges, it is essential to explore alternative battery chemistries based on materials that are abundant and globally distributed. Such alternatives could reduce costs, enhance energy security, and minimize environmental footprints. Among these, multivalent technologies, such as magnesium (Mg), calcium (Ca), and theoretically Al, offer the potential for higher energy densities than monovalent systems like LIBs [6], [7], [8]. This advantage is particularly relevant for applications requiring compact, high-capacity storage, including electric vehicles and grid-scale systems.

This research contributes to the broader post-Li vision by investigating RABs, which leverage Al's reduction and oxidation (redox) process to achieve high theoretical capacity. The work aligns with the goals of the Cluster of Excellence POLiS (Post-Lithium Storage), which is dedicated to developing next-generation battery technologies beyond Li [9]. Through a combination of experimental investigation and mechanistic analysis, this thesis advances the fundamental understanding of RAB systems and their potential role in future energy storage solutions.

1.2 Why Aluminium? Abundance, Safety, and Cost

Aluminium (Al) is increasingly explored as a candidate for next-generation energy storage due to its natural abundance, environmental stability, and recyclability. As the third most abundant element in the Earth's crust, Al offers significant advantages in terms of resource availability, helping to mitigate the geopolitical and supply chain risks associated with more scarce elements.

Its theoretical volumetric capacity of 8040 mAh cm^{-3} and gravimetric capacity of 2980 mAh g^{-1} are among the highest battery anode materials, and are attributed to its multivalent nature, enabling the transfer of three electrons per ion (Al^{3+}/Al^0 redox reaction), However, in practical battery systems, this full three-electron transfer is rarely achieved. Most Al-based systems operate via a one-electron redox process, significantly reducing the actual capacity. Moreover, Al's relatively high redox potential (−1.66 V vs. SHE) introduces a voltage penalty compared to more electropositive metals like Li or Mg. Thus, Al's viability hinges on whether its theoretical capacity can offset this voltage limitation [10]. Table 1.1.1, compares key properties of battery-relevant metals, illustrating that Al does not stand out in terms of redox potential or ionic radius. Its appeal lies in its abundance and potential energy density under ideal conditions.

Beyond its intrinsic properties Al's recyclability offers a compelling sustainability advantage. Unlike lithium, which requires complex and energy-intensive recycling processes, Al is widely recycled at scale with relatively low energy input. This makes Al-based systems attractive for circular economy models and environmentally conscious energy storage solutions.

Table 1.1 Relevant properties of Li, sodium (Na), potassium (K), Mg, Ca, zinc (Zn), and Al [10], [11], [12]

	Redox potential (V vs SHE)	**Ionic radius (pm)**	**Abundance in the Earth's crust (mg/kg)**	**Theoretical specific capacity (Ah g^{-1})**
Li	-3.05	90	20	3.86
Na	-2.71	116	23600	1.16
K	-2.92	152	20900	0.68
Mg	-2.37	86	23300	2.20
Ca	-2.87	114	41500	1.34
Zn	-0.76	88	70	0.82
Al	-1.66	68	82300	2.98

High-purity Al is required for RAB applications, raising costs to between 261.95 € kg^{-1} (99.99% purity) and 950.95 € kg^{-1} (99.9999% purity [13]. From a safety perspective, metallic Al is stable under ambient conditions unlike Li or Na, and the non-flammable nature of typical chloroaluminate ionic liquid (IL)-based electrolytes (in contrast to the flammable organic electrolytes used in LIBs) offers a substantial improvement in battery safety.

The combination of high theoretical capacity, low material cost, and enhanced safety positions RABs as a compelling alternative for large-scale energy storage. However, the development of competitive RABs presents challenges, and direct knowledge transfer from established LIBs technology is not straightforward. Key obstacles include:

- **Electrolyte corrosivity**: The acidic, highly corrosive nature of the chloroaluminate IL-based electrolytes, necessary to remove the stable native oxide layer on the Al anode and enable plating and stripping, leads to dissolution and undesirable side reactions involving active and passive cell components [14], [15]. This limits the choice of compatible electrodes, current collectors, and cell casing materials, impacting cell durability and safety[13].
- **Active species management**: Chloroaluminate IL-based electrolytes, often considered anolytes are directly involved in anodic plating and stripping. The active species (tetrachloroaluminate anion ($AlCl_4^-$) and heptachloro-dialuminate anion ($Al_2Cl_7^-$) are confined to the electrolyte [15]. The Al anode acts as a substrate for its plating/stripping and a buffer to maintain the electrolyte

composition [16]. The large size of these ions can induce significant volume changes in cathode materials, contributing to degradation [17], [18].

- **Cathode performance:** The limited practical capacity, poor rate capability, and rapid capacity fade of cathode materials remain significant bottlenecks. Graphite is currently the state-of-the-art cathode for non-aqueous RABs due to its good initial capacity and cycling stability [19]. Many other materials have exhibited low practical performance and poor cycling stability, indicating that reaction mechanisms are yet to be fully understood [20], [21], [22].

This research work aims to advance the understanding of charge storage mechanisms in promising cathode materials and to clarify the role of compatible passive components in ensuring long-term cell integrity and performance, critical knowledge gaps that must be bridged for RABs to achieve their full potential in the energy landscape.

1.3 Research Scope and Hypotheses

RABs represent a promising alternative to LIBs technologies, particularly for applications requiring high safety, low cost, and material abundance. However, their development remains at an early stage, and it would be premature to consider them a direct replacement for LIBs. Fundamental research is therefore essential, especially in understanding cathode behaviour and the interactions between active and passive components within the system.

This research work aims to contribute to the advancement of RABs by investigating the electrochemical behaviour of selected cathode materials and evaluating the role of passive components in enhancing overall cell performance. The research is guided by two broad hypotheses.

1.3.1 Hypothesis 1: Charge Storage Mechanism in Transition Metal Chalcogenide Cathodes

It is hypothesized that transition metal chalcogenides, such as cobalt selenide (CoSe), do not operate via simple insertion mechanisms in RABs. Instead, their charge storage behaviour is governed by more complex electrochemical processes, potentially involving conversion reactions and redox activity of non-metallic elements. These mechanisms are expected to influence capacity retention, rate capability, and long-term stability.

1.3.2 Hypothesis 2: Functional Roles of Layered Passive Components

It is further hypothesized that layered materials such as MXenes, specifically titanium carbides ($Ti_3C_2T_X$) can serve multifunctional roles in RABs beyond conventional passive support. Their integration into various cell components, such as current collectors, and separators, is expected to influence electronic conductivity, mitigate degradation pathways, and improve overall electrochemical performance. These effects are anticipated to be dependent on the specific application and operating conditions.

The detailed knowledge gaps and specific contributions arising from the investigation of these hypotheses are presented in Section 3.6, following a comprehensive review of the theoretical background and state-of-the-art developments in RAB technology.

In this dissertation a systematic test these hypotheses is executed through comprehensive experimental investigations and advanced characterisation techniques. Based on the findings, the initial predictions are evaluated, providing crucial insights into the fundamental mechanisms governing the electrochemical behaviour of these materials and their impact on RABs performance (capacity retention, rate capability, and cycle life) and reliability.

2 Theoretical Background: Principles of Battery Science

In essence, both science and art strive to understand and interpret reality, although they do it by different means. While science meticulously explains the mechanisms of the world, revealing its intricate truths through rigorous observation, experimentation, and logical deduction; art imitates, interprets, and reflects these very realities, offering new perspectives and profound emotional resonance.

In the context of scientific research, in this chapter a comprehensive review of the fundamental principles of battery science is be provided, outlining the established knowledge, historical milestones, and analytical tools indispensable for understanding the complex electrochemical systems that are the focus of this dissertation.

In this chapter a brief literature review on batteries is presented. It is structured as follows:

- Section 2.1: Historical evolution of batteries.
- Section 2.2: Fundamental electrochemical principles.
- Section 2.3: Determining battery performance.
- Section 2.4: Dynamic characterisation of battery electrodes.

2.1 Historical Evolution of Batteries

Batteries as we know them today are the result of centuries of scientific evolution and technological adaptation. From the ancient Persian Baghdad Battery to Volta’s zinc-silver stack soaked in salt-water, to Planté’s invention of the rechargeable lead–acid cell, the core principle (the transformation of chemical energy into electrical energy through redox reactions) has remained fundamentally unchanged. What has changed are the materials, architectures, and performance metrics, driven by societal needs: from high-power sources for military and medical applications, to lightweight and portable energy solutions for the growing consumer electronics market [23].

The success of LIBs is attributable to the contribution of several key scientists: Stanley Whittingham enabled the first commercial rechargeable Li battery by discovering titanium disulphide (TiS_2) cathode, John Goodenough proposed the use of oxides instead of sulphides to obtain greater potential leading the development of higher-potential cathodes like lithium cobalt oxide ($LiCoO_2$, LCO). Finally, Akira Yoshino introduced petroleum coke as an anode material demonstrating its ability to reversibly intercalate Li^+ ions. The collective contribution of these three scientists resulted in the LIBs that, as highlighted by the Nobel press release of 2019, “have revolutionized our lives since they first entered the market in 1991. They have laid the foundation of a wireless, fossil fuel-free society and are of the greatest benefit to humankind” [23], [24].

LIBs consist of a Li^+ ion conductive electrolyte soaked in a porous separator, situated between two electrodes. During operation, Li^+ ions reversibly migrate back and forth between these electrodes in a process often called “rocking chair” mechanism. A schematic representation of LIBs functioning is presented in Figure 2.1 [25].

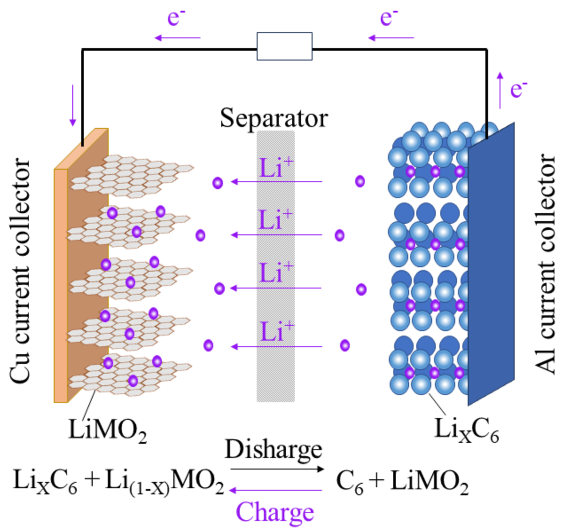

Figure 2.1 Scheme of the functioning process on LIBs [25]

As the currently dominant rechargeable battery technology, LIBs are primarily characterized by their high energy density, high operating voltage, and good cycling life. The performance landscape of various battery technologies is illustrated in Figure 2.2 which plots volumetric energy density against gravimetric energy density. LIBs demonstrate a significant advantage over other chemistries. They exhibit superior balance for gravimetric and volumetric energy densities. While Li metal batteries theoretically offer even higher energy densities, their practical application remains limited by significant safety concerns [26].

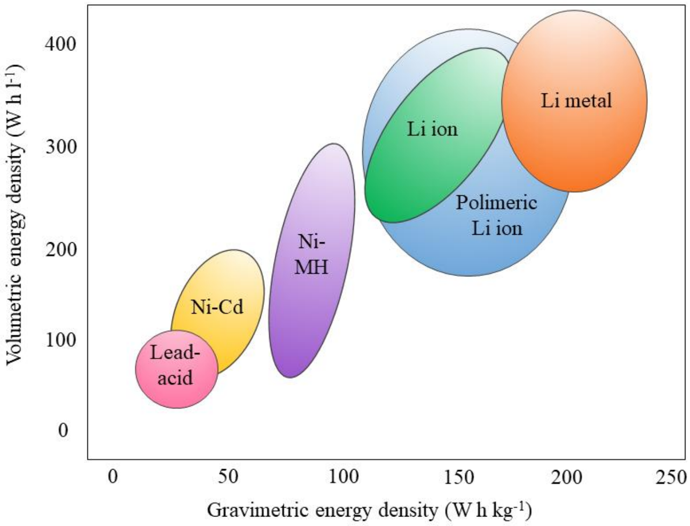

Figure 2.2 Energy density trade-off map of battery technologies [26]

Continuous research efforts are dedicated to further enhancing LIBs performance. However, despite these profound advancements, the inherent limitations of LIBs concerning cost, safety, and raw material sustainability, continue to drive the search for next-generation energy storage solutions, such as RABs.

2.2 Fundamental Electrochemical Principles

Batteries are electrochemical devices that transform stored chemical energy directly into electrical energy via redox reactions. This process is achieved by forcing the flow of electrons through an external circuit while the electrodes are connected via an electronically insulating yet ionically conductive electrolyte. The electrode where oxidation (loss of electrons) occurs is called anode and the electrode where reduction (gain of electrons) occurs is called cathode.

Based on the reversibility of their processes, batteries are classified as primary (irreversible, single use) or secondary (rechargeable, reversible). Given the environmental and renewable energy focus of this thesis, this research work is focused solely on the secondary batteries. In this system, the roles of the anode and cathode reverse depending on whether the battery is charging or discharging. In contrast, the terms positive electrode and negative electrode are based on the fixed electrical polarity of the terminals. For practicality, in this research work, the term ‘cathode’ refers to the positive electrode during discharge and the term ‘anode’ refers to the negative electrode during discharge.

2.2.1 Thermodynamics of Batteries

The fundamental driving force for an electrochemical reaction in a battery is the change in Gibbs free energy (ΔG), which represents the difference in chemical energy between the products and reactants of the overall cell reaction. The free energy change corresponds to the maximum electrical work $\mathrm{W_{elec}}$ that can be obtained from the reaction:

$$\mathrm{W_{elec}} = -\Delta G \qquad \text{(Eq 2.1)}$$

In an electrochemical cell, this electrical work is related to the amount of charge transferred (nF) and the cell potential (E) as:

$$\mathrm{W_{elec}} = nFE \qquad \text{(Eq 2.2)}$$

Where n is the number of moles of electrons transferred per mole of reaction and F is Faraday’s constant (96485 C mol^{-1}). Under standard conditions (298.15 K, 1 atm pressure for gases, and unit activity for all solutes and pure solids/liquids), the standard Gibbs free energy change ($\Delta G°$) relates to the standard cell potential ($E°$):

$$\Delta G° = -nFE° \qquad \text{(Eq. 2.3)}$$

For non-standard conditions, the reversible potential is related to the standard potential by the Nernst equation:

$$E_{\mathrm{Rev}} = E° - \frac{RT}{nF}\ln(Q) \qquad \text{(Eq 2.4)}$$

Where R is the ideal gas constant, T is the absolute temperature and Q is the reaction quotient, which represents the ratio of product activities to reactant activities raised to their stochiometric coefficients. For rechargeable batteries, the activities of products and reactants continuously change during charge and discharge. Consequently, the actual reversible potential (E_{Rev}) of a battery is not constant but varies significantly with its state of charge (SOC), as dictated by the Nernst equation. Thus, E represents the maximum reversible voltage that can be generated by the cell when there is no current flow [27].

2.2.2 Irreversibilities in Batteries

The Nernst equation defines the ideal, reversible potential. However, in real batteries, different irreversibilities lead to a deviation from this ideal potential. Overpotentials (η) arise from kinetic limitations at the electrodes, as well as resistive loss throughout the cell. These losses reduce the operating voltage during discharge, increase it during charge, and convert electrical energy into heat.

The total overpotential of a cell is the sum of the individual contributions from each cathode and the bulk resistance of the electrolyte and current collectors. The overall operating potential (E_{cell}) of a battery is the reversible potential (E_{Rev}) minus the overpotentials during discharge:

$$E_{\mathrm{cell}} = E_{\mathrm{Rev}} - \eta_{\mathrm{activation}}^{\mathrm{total}} - \eta_{\mathrm{concentration}}^{\mathrm{total}} - \eta_{\mathrm{ohmic}} \qquad \text{(Eq 2.5)}$$

or the sum during charge:

$$E_{\mathrm{cell}} = E_{\mathrm{Rev}} + \eta_{\mathrm{activation}}^{\mathrm{total}} + \eta_{\mathrm{concentration}}^{\mathrm{total}} + \eta_{\mathrm{ohmic}} \qquad \text{(Eq 2.6)}$$

The dominant irreversibility depends on the operating conditions. At low current densities, activation overpotential is often the most significant, at moderate current densities, it is the ohmic losses that become prominent; and at high current densities, the concentration overpotential are the most dominant.

2.2.2.1 Activation overpotentials ($\eta_{\mathrm{activation}}$)

Activation overpotentials are caused by the finite speed at which electrochemical reactions occur at the electrode surface. They are attributed to the energetic barrier that reactants must overcome to transform into products. This overpotential for a single electrode reaction is a function of the current density as described by the Buttler-Volmer equation:

$$i = i_0 \left(\exp\left(\frac{\alpha n F \eta_{\text{activation}}}{RT} \right) - \exp\left(- \frac{(1-\alpha) n F \eta_{\text{activation}}}{RT} \right) \right) \qquad \text{(eq 2.7)}$$

where i_0 is the exchange current density and α is the charge transfer coefficient (typically between 0 and 1). The exchange current density (i_0) represents the intrinsic kinetic activity of the electrode at equilibrium (when the net current is zero); it quantifies the rate at which oxidation and reduction reactions occur simultaneously [28].

At sufficiently high current densities, when the reverse reaction rate is negligible, the Buttler-Volmer equation simplifies to the Tafel equation:

$$\eta_{\text{activation}} = \frac{RT}{\alpha n F} \ln\left(\frac{i}{i_0} \right) \qquad \text{(Eq. 2.8)}$$

for the anodic current or:

$$\eta_{\text{activation}} = \frac{RT}{(1-\alpha) n F} \ln\left(\frac{|i|}{i_0} \right) \qquad \text{(Eq. 2.9)}$$

for the cathodic current.

2.2.2.2 Concentration overpotentials ($\eta_{\text{concentration}}$)

Concentration overpotentials are caused by the limited speed at which mass transport of reacting species occurs. This transport can occur through migration (due to electric field), diffusion (due to concentration gradients) or convection (due to fluid flow) processes. In batteries, these limitations are especially important as electrochemical reactions primarily take place at the electrode- electrolyte interface. When the reaction rate (current) is high, the consumption or generation of species at the electrode surface leads to significant differences between concentration of active species at the surface and the bulk.

This overpotential for a single electrode reaction is a function of the difference in concentration between the bulk electrolyte and the electrode surface. The overpotential becomes more significant as the current density approaches the limiting current density (i_L). It can be expressed as:

$$\eta_{\text{concentration}} = \frac{RT}{nF} \ln\left(1 - \frac{i}{i_L}\right) \qquad \text{(Eq. 2.10)}$$

where i_L is the maximum current density at which the reaction can proceed, defined by the maximum rate of mass transport of the reactant to the electrode surface (or product away from it). At i_L, the concentration of the reacting species at the electrode surface approaches zero [28].

2.2.2.3 Ohmic losses (η_{ohmic})

Finally, ohmic losses are caused by the inherent electrical resistance of all components within the cell. These include electronic resistance of the electrodes and current collectors, contact resistance between components, and the ionic resistance of the electrolyte, these losses manifest as a voltage drop proportional to the current flow, as defined by Ohm's law:

$$\eta_{\text{ohmic}} = i\, R_{\text{total}} \qquad \text{(Eq. 2.11)}$$

Where i is the current density and R_{total} is the total equivalent series resistance of the battery.

Collectively, these overpotentials contribute to the battery internal resistance (R_{int}), which a portion of the electrical energy into heat (Joule heating), contributing to the battery's thermal load heat [28].

In essence, an understanding of these fundamental electrochemical principles, the thermodynamics governing cell potential and the diverse origins of irreversibilities, are fundamental to comprehend battery operation. These principles not only provide the theoretical foundation for energy conversion within a battery but also explain the inherent limitations, efficiency losses, and degradation pathways that dictates a battery's practical performance characteristics.

2.3 Determining Battery Performance

The performance of a battery can be characterized by several key parameters.

2.3.1 Potential (E)

The potential of a battery (E) is a measure of the energy available to drive charge externally between the two electrodes. It represents the potential difference between the positive and negative electrodes, separated by the electrolyte. The unit of potential is Volts (V), equivalent to Joules per Coulomb (J/C). Being the driving force for charge transfer, it is one of the most critical to understand and optimize in battery design.

When a battery is connected to a high impedance voltmeter (ensuring negligible current flow), the measured value is the open circuit voltage (OCV). This OCV represents the reversible potential of the cell under equilibrium conditions.

2.3.2 Capacity

The theoretical capacity refers to the total quantity of electricity (charge) that a battery can store when fully charged and can deliver during discharge. It is expressed in units of Coulombs (C) or Ampere-hours (Ah). The theoretical capacity of a battery is determined by the amount of active material present and the number of electrons transferred per mole of active material. As governed by Faraday's law. For an active material, the theoretical specific capacity, expressed in mAh g^{-1}, can be calculated as:

$$C_{\mathrm{th}eoretical} = \frac{n \times F}{3.6 \times M_w} \times 1000 \text{ (mAh g}^{-1}\text{)} \qquad \text{(Eq. 2.12)}$$

Where n is the number of moles of electrons transferred per mole of active material, M_w is the molar mass of the active material (g mol^{-1}), and 3.6 converts Coulombs to mAh. In a full cell, the overall capacity is determined by the electrode that contains the least amount of active material or that reaches its capacity limit first.

For CoSe, for instance, would present a theoretical capacity of 583.05 mAh g^{-1} if its redox reaction involved a three-electron transfer (Al^{3+}/Al^{0}) process. However, the results of this research work provide evidence that the actual electrochemical mechanism does not proceed via simple Al^{3+} intercalation. Instead, it involves the participation of $AlCl_4^-$ species. This alternative mechanism and its implications will be discussed in detail in Chapters 6 and 7.

$$C_{CoSe} = \frac{1 \times F}{3.6 \times 137.9} \times 1000$$

$$C_{CoSe,1e^-} = 194.35\ \text{mAh g}^{-1}$$

$$C_{CoSe} = \frac{3 \times F}{3.6 \times 137.9} \times 1000$$

$$C_{CoSe,3e^-} = 583.05\ \text{mAh g}^{-1}$$

The practical capacity of a battery or half-cell is invariably lower than its theoretical value. This reduction rises from several factors including: incomplete utilisation of active material, occurrence of parasitic side reactions (i.e., solid electrolyte interphase (SEI) formation), and inherent irreversibilities of electrochemical reactions. These factors contribute to difference between charge and discharge capacities, leading to the definition of coulombic efficiency.

2.3.3 Coulombic Efficiency (CE)

Coulombic efficiency (CE), often referred to as charge efficiency or faradaic efficiency, quantifies the reversibility of charge and discharge processes in a battery, is defined as the ratio of the discharge capacity ($Q_{\text{discharge}}$) extracted from the battery to the charge capacity (Q_{charge}) put into it during a single cycle:

$$CE = \frac{Q_{\text{discharge}}}{Q_{\text{charge}}} \times 100\% \qquad \text{(Eq. 2.13)}$$

A coulombic efficiency of 100% indicates a perfectly reversible process with no charge losses. Often, the first cycle has a lower coulombic efficiency due to initial irreversible processes, such as the formation of SEI which consumes active material and electrolyte.

2.3.4 Cycling Stability

The cycling stability describes its ability to maintain performance metrics, such as capacity and efficiency, over a specified number of charge-discharge cycles. It provides crucial information about long-term irreversibilities and degradation mechanism, including active material dissolution, electrolyte decomposition, and structural changes within the electrodes [29].

2.3.5 C-Rate

The C-rate is a measure of the rate at which a battery is charged or discharged relative to its nominal capacity. The nominal capacity is the real capacity of a battery reflecting its expected performance under specific conditions, in research it is often the measured initial discharge capacity. A 1 C rate indicates the current required to fully discharge a battery in one hour. Conversely a 0.5 C rate would be discharged in two hours and a 2 C rate in half an hour.

The current (I) at a specific C-rate can be calculated using the battery´s nominal capacity (Q_{nominal}):

$$I = Q_{\text{nominal}} \times C_{\text{rate}} \qquad (\text{Eq. } 2.14)$$

Battery performance, including capacity and efficiency, is often measured and reported as a function of the applied C-rate.

2.3.6 Power (P) and Energy ($\mathcal{E}$) Capabilities

Power and energy capabilities are critical metrics for comparing batteries, especially for applications with dynamic load demands. These two parameters often represent a fundamental trade-off in battery design.

Power (P) is defined as the instantaneous rate at which electrical energy is delivered or consumed by the battery.

$$P(t) = E(t) \times I(t) \qquad (\text{Eq. } 2.15)$$

Where E is the instantaneous cell voltage and I is the instantaneous current.

The maximum power a battery can deliver is limited by its internal resistance and kinetic factors. Operating a battery beyond its recommended power limits can lead to significant voltage drops, excessive heat generation, and accelerated degradation mechanisms, thereby shortening its lifespan.

Power density quantifies the power output per unit mass (gravimetric power density, W kg^{-1}) or per unit volume (volumetric power density, W l^{-1}). It is a crucial metric for applications requiring rapid energy delivery or high current bursts.

The energy ($\mathcal{E}$) stored in a battery represents the total electrical work that can be delivered. It is expressed in Watt-hours (Wh), which is equivalent to Volts (V) by Ampere-hour (Ah), or in Joules (J). While its theoretical maximum is governed by the Gibbs free energy (see Section 2.2.1), the practical energy available is lower due to kinetic limitations, internal resistance, and voltage cutoffs.

When considering the contributions of both electrodes, the energy density of a full cell can be approximated by:

$$\mathcal{E} = \frac{\mathrm{C_A C_C}}{\mathrm{C_A + C_C}} \cdot \mathrm{V} \qquad (\mathrm{Eq.\,2.16})$$

Where C_A and C_C are the capacities of anode and cathode and V is the average operating voltage of the cell. In cases where both electrodes have similar capacity contribution, it can be simplified as:

$$\mathcal{E} \approx C \cdot \mathrm{V} \qquad (\mathrm{Eq.\,2.17})$$

This metric is vital for applications where battery weight or size are critical constraints, such as portable electronics and electric vehicles.

2.3.7 Energy Efficiency (EE)

While coulombic efficiency quantifies capacity losses during a cycle, energy efficiency provides a more comprehensive measure of the overall battery efficiency. It considers both capacity losses and voltage losses during charge and discharge.

$$EE = \frac{\mathcal{E}_{\mathrm{discharge}}}{\mathcal{E}_{\mathrm{charge}}} \times 100\% \qquad (\mathrm{Eq\ 2.18})$$

Where $\mathcal{E}_{\mathrm{discharge}}$ is the total energy extracted during discharge and $\mathcal{E}_{\mathrm{charge}}$ is the total energy put into the battery during charge. A high energy efficiency is critical for many applications, as it directly impacts the overall system efficiency and thermal management requirements.

2.4 Dynamic Characterisation of Battery Electrodes

Understanding the complexity of batteries demands a higher level of materials science insight and cutting-edge characterisation techniques. Researchers employ various methods to study the interactions and transformations taking place, broadly categorized by when the measurement is performed relative to the battery's operation: *ex situ*, *in situ*, and *operando* techniques. An analogy illustrating the crucial distinctions between these approaches is provided in Figure 2.3 highlighting how the environment of observation impacts the understanding of a system's true behaviour.

2.4.1 Ex situ

From the Latin “out of place”, involves measurements performed on battery components after the battery is disassembled and removed from its electrochemical environment, it also includes components that have never been assembled into battery (i.e., pristine electrode materials). This approach allows for a wide range of analytical techniques but can introduce artifacts, as it may alter the original state of the material.

2.4.2 In situ

From the Latin “in place”, refers to measurements performed on battery components within a functional cell, but not under active electrochemical cycling. This allows for real-time observations of changes as a function of time or voltage, effectively avoiding artifacts that might arise from disassembly.

2.4.3 Operando

From the Latin “in operation”, refers to a subset of *in situ* measurements. These are performed on battery components while the cell is actively undergoing electrochemical cycling. The collected data is directly correlated with the electrochemical measured state, providing unparalleled insight into dynamic chemical and structural changes as they occur.

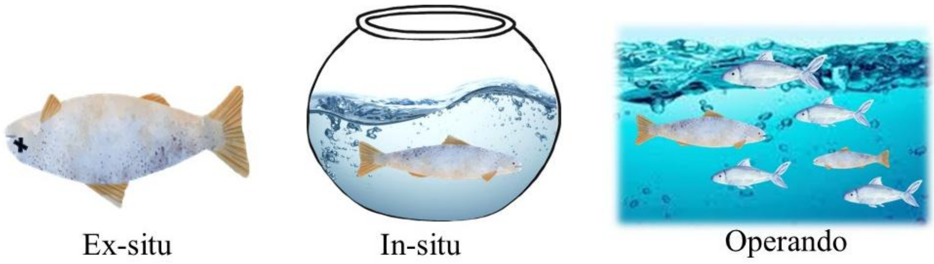

Figure 2.3 Analogy for the concepts of *ex situ*, *in situ*, and *operando*. Modified from [30]

To move beyond speculative interpretations and achieve a robust understanding of the intrinsic charge storage and degradation mechanisms in electrode materials, it is essential to employ *in situ* and *operando* characterisation techniques. These methods enable direct observation of structural, electronic, and chemical changes within the active material as the battery operates, offering insights into reaction pathways, phase evolution, and the origins of performance degradation.

As emphasized by Bak et al. [31], *in situ* and *operando* techniques surpass *ex situ* methods by capturing real-time data, allowing the study of non-equilibrium and transient processes. They enable the detection of intermediate species and prevent the relaxation, contamination, or loss of critical information during sample handling. Despite their advantages, practical limitations such as restricted access to synchrotron beamlines and specialized instrumentation make *ex situ* analysis an indispensable tool for preliminary investigations.

In this study, dynamic characterisation is achieved through a combination of *operando* X-ray diffraction (XRD) and X-ray absorption spectroscopy (XAS), each offering complementary insights into the structural and electronic evolution of the CoSe cathode.

2.4.4 X-ray Diffraction

XRD is an analytical technique used to study the crystal structure, phase composition, and lattice parameters of materials. It works by directing X-rays onto a sample and measuring the angles and intensities of the diffracted beams. The resulting diffraction pattern serves as a “fingerprint” of the material’s atomic arrangement, allowing for the identification of crystalline phases and detection of structural changes. Because each crystal structure produces a unique diffraction pattern according to Bragg’s Law (Eq. 2.9), XRD provides precise information about how atoms are organized within a solid.

$$n\lambda = 2\mathrm{d}\sin(\theta) \qquad \text{(Eq 2.9)}$$

Where n is the order of reflection, an integer (1, 2, 3, …) that represents how many wavelengths fit into the path difference between reflected X-rays, λ is the wavelength of the incident X-rays, d is the interplanar spacing, θ (theta) is the angle between the incident X-ray beam and the crystal plane [32].

The crystal structure of electrode materials is a primary determinant of battery performance. For instance, open lattice structures facilitate ion intercalation and deintercalation, enhancing rate capability and energy density [33]. Since initial studies on intercalation phenomena, XRD has been the most used technique for monitoring structural changes induced by ion insertion [34].

XRD provides information on lattice parameters, phase transitions, and strain effects, but is limited to crystalline materials. If the charge storage mechanism involves conversion to an amorphous phase, the diffraction pattern will reflect this transformation through peak broadening or disappearance.

2.4.5 X-ray Absorption Spectroscopy

XAS is an analytical technique used to probe the local atomic and electronic structure of materials. It works by measuring how a material absorbs X-rays as the X-ray energy is gradually increased through the binding energy of a specific core electron of an element. When the X-ray energy matches the binding energy, the core electron is excited to an unoccupied state or ejected, leading to a sharp increase in absorption known as the absorption edge. By analysing the fine structure of the absorption spectrum around this edge, researchers can extract detailed information about the oxidation state, coordination environment, and bond lengths of the absorbing atom [35].

XAS is divided into two main regions: X-ray Absorption Near Edge Structure (XANES) and Extended X-ray Absorption Fine Structure (EXAFS). XANES provides information about the oxidation state and electronic structure of the element, while EXAFS reveals data on the distances, coordination numbers, and types of neighbouring atoms.

Electrochemical reactions inherently involve changes in the oxidation states of the elements comprising the electrode material. These changes are critical for identifying which species participate in redox processes and for understanding the local chemical environment during cycling.

XAS is particularly well-suited for this purpose due to its element-specific sensitivity and ability to probe both the electronic state and local coordination geometry of the absorbing atom. While XAS is limited to elements with sufficiently high atomic numbers and may be affected by interference from other cell components, its capacity to provide a detailed fingerprint of the local electronic structure makes it indispensable for mechanistic studies.

3 State of the Art and Research Positioning-Chemistry of RABs

Like investigators at a complex crime scene, meticulously examining every piece of evidence is vital for resolving a murder case, understanding the true behaviour, and unlocking the full potential of RABs demands a thorough and critical examination of all available scientific information. In this chapter, therefore, a critical review of the current state of knowledge regarding materials and electrochemical mechanisms pertinent to rechargeable RABs is provided. It aims to systematically consolidate the existing understanding while rigorously assessing proposed theories and experimental findings.

In recent years, the increasing demand for sustainable and high-performance energy storage solutions has intensified the research for alternatives to conventional LIBs. This drive is fuelled by growing concerns regarding resource scarcity, safety issues, and environmental impact associated with Li-based systems. Among the emerging technologies, RABs have gained significant attention due to the intrinsic advantages of Al (Section 1.2).

However, unlike established LIBs, which primarily rely on well-understood intercalation mechanisms and electrolytes, RABs introduce distinct electrochemical complexities. The chemistry of RABs is still in its infancy, and the inherent corrosivity of its most employed chloroaluminate IL-based electrolyte significantly impedes their growth and widespread application. This has led to major challenges in material development, often resulting in systems where excellent theoretical performance is coupled with uncertain mechanisms, or where known mechanisms lead to disappointing practical outcomes. Consequently, a plethora of fundamental and practical questions persist, necessitating comprehensive resolution to enable the transition of RABs from laboratory curiosity to practical applications.

Throughout this review, electrochemical performance, proposed charge storage, and degradation mechanisms will be rigorously assessed, with special attention paid to inconsistencies and ambiguities within the existing literature. This chapter is structured to build a foundational understanding of RABs as follows:

- Section 3.1: Electrolyte.
- Section 3.2: Electrochemical mechanism at the anode.
- Section 3.3: Positive electrodes and mechanisms (emphasis is placed on graphite and cobalt selenides (CoSe and $CoSe_2$), which are thoroughly discussed as cathode materials central to this dissertation).
- Section 3.4: Passive components.
- Section 0: Knowledge gaps: contribution of this research work.

3.1 Electrolyte

The electrolyte is the cell component responsible for transporting ions from one electrode to the other. Therefore, it must exhibit high ionic conductivity and low viscosity to minimize diffusion resistance. An ideal electrolyte for RABs must allow for reversible Al plating and stripping and possess a wide electrochemical stability window to prevent degradation and ensure the long-term stability of all cell components.

Research in RABs has primarily focused on systems employing chloroaluminate IL-based electrolytes. Alternative systems, such as high-temperature molten salts and organic solvent-based electrolytes have faced significant drawbacks, including passive oxide film formation, hydrogen evolution, and severe anode corrosion [36]. While these systems offer promising attributes, such as enabling lower operating temperatures, their consistent challenges with reversibility and safety have shifted research focus. For these reasons, the subsequent discussion focuses exclusively on room-temperature ionic liquids, which have emerged as the most promising platform for RABs.

Room temperature IL (RTILs) are essentially molten salts that are liquid at or near ambient temperature, representing a significant advancement over high-temperature systems. Unlike conventional electrolytes, RTILs are free of molecular solvent, resulting in considerable higher concentration of active species. They also possess attractive properties for battery applications, including low flammability, negligible vapor pressure, high-ionic conductivity and wide electrochemical stability window.

Among RTILs, chloroaluminate systems, particularly aluminium chloride ($AlCl_3$):1-ethyl-3-methylimidazolium chloride (EMImCl), have become the most extensively studied and successful electrolytes. These are formed by mixing anhydrous $AlCl_3$ with EMImCl [37]. Despite remaining challenges like high corrosivity and material compatibility, $AlCl_3$:EMImCl continues to be the benchmark against which new electrolytes are often compared. Its excellent performance in early RABs studies solidified its significance and has been instrumental in the progress of RABs.

3.2 Electrochemical Mechanism at the Al Anode

In RABs, that employ a $AlCl_3$:EMImCl electrolyte, and graphite cathode, the charge storage operates via dual-ion mechanism. This mechanism differs from the well-known rocking-chair mechanism characteristic of LIBs. In RABs, it entails the reversible plating and stripping of metallic Al at the anode, which occurs concurrently with the insertion/deinsertion or conversion of the $AlCl_4^-$ anions at the cathode. This section will primarily focus on the electrochemical mechanism occurring at the Al anode, as the specific mechanism at the cathode is intimately linked to the nature of active material.

The reversible plating and stripping of Al at the anode surface has been extensively studied. As demonstrated by Gifford and Palmisano in 1988 plating and stripping processes is highly dependent on the precise $AlCl_3$:EMImCl molar ratio [37]. This dependency stems from the Lewis acid-base chemistry between $AlCl_3$ (a Lewis acid) and Cl^- (a Lewis base) within the ionic liquid.

In basic or neutral melts (where $AlCl_3$:EMImCl ≤ 1), the predominant species is the $AlCl_4^-$ anion. Crucially, effective Al plating is not observed under these conditions due to the absence of the active species. However, when an excess of $AlCl_3$ is present (in acidic melts where $AlCl_3$:EMImCl > 1), the ionic liquid transforms into a mixture containing both $AlCl_4^-$ and the crucial $Al_2Cl_7^-$. It is the $Al_2Cl_7^-$ anion that is essential for reversible

Al plating and stripping at the anode. Consequently, the capacity of the battery is directly related to the concentration of $Al_2Cl_7^-$ in the electrolyte.

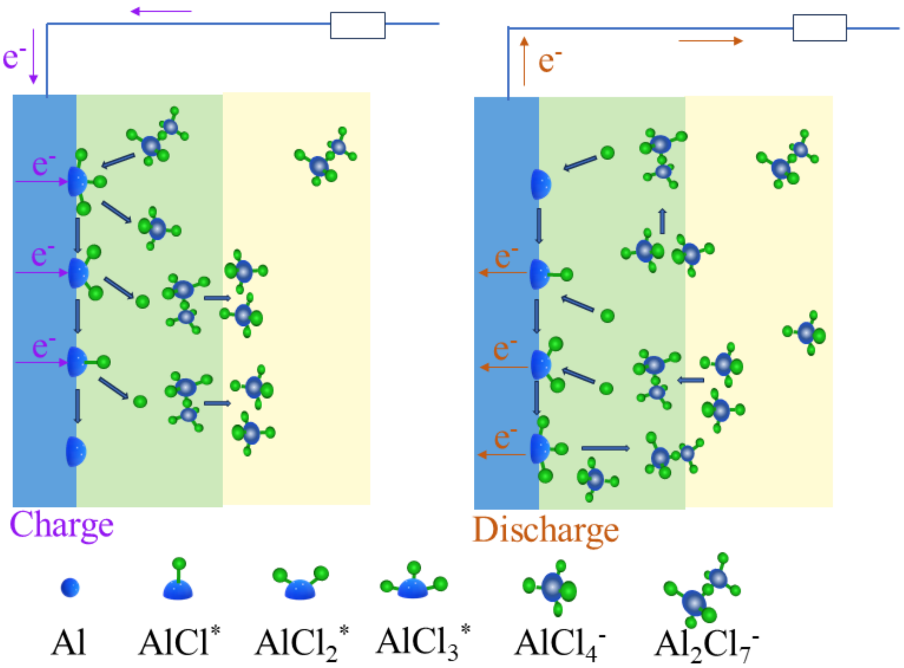

Figure 3.1 Mechanism of plating and stripping of Al in chloroaluminate IL based electrolyte [15]

The electrochemical plating of Al at the anode involves the reduction of Al_2Cl_7. The overall reaction is represented as:

$$4Al_2Cl_7^- + 3e^- \rightleftarrows Al + 7AlCl_4^- \qquad \text{(Chem. Eq. 3.1)}$$

While the overall process has a high activation energy (>400 kJ mol^{-1}), is believed to proceed via a series of intermediate steps involving adsorbed species. During plating, $Al_2Cl_7^-$ is reduced, potentially forming adsorbed intermediates such as $^*AlCl_3$, $^*AlCl_2$, and $^*AlCl$. These steps involve successive one-electron transfer reduction-dechlorination reactions:

$$Al_2Cl_7^- + e^- \rightleftarrows {}^*AlCl_3 + AlCl_4^- \qquad \text{(Chem. Eq. 3.2)}$$

$$^*AlCl_3 + e^- \rightleftarrows {}^*AlCl_2 + Cl^- \qquad \text{(Chem. Eq. 3.3)}$$

$$^*AlCl_2 + e^- \rightleftarrows {}^*AlCl + Cl^- \qquad \text{(Chem. Eq. 3.4)}$$

$$^{*}\mathrm{AlCl} \rightleftarrows \mathrm{Al} + \mathrm{Cl}^- \qquad \text{(Chem. Eq. 3.5)}$$

The chlorine ions released during these dechlorination steps are thought to react with other $Al_2Cl_7^-$ ions, leading to the formation of $AlCl_4^-$, which is then released into the bulk electrolyte. The stripping (discharging) mechanism proceeds via the reverse of these reactions [15]. A detailed scheme illustrating these plating and stripping processes is presented in Figure 3.1.

3.3 Positive Electrodes and Mechanisms

The cathode material is a critical component that dictates the overall performance, specific capacity and cyclability of RABs. It is important to note that while the process at the anode is efficient, capable of withstanding high current densities [38], the overall operation in RABs is typically limited by the positive electrode.

3.3.1 Current Collector Contributions and Misleading Capacities

Before exploring specific cathode material, it is crucial to acknowledge a significant challenge in early RABs research: the misattribution of capacity from corrosion reactions involving current collectors or cell case. Materials like stainless steel (SS), molybdenum (Mo) or nickel (Ni), can undergo corrosion or electrochemical dissolution in acidic chloroaluminate IL-based electrolyte, leading to inflated capacity values that do not originate from the active cathode material itself [13]. Therefore, a critical evaluation of reported electrochemical performance is always necessary and encouraged.

3.3.2 Charge Carriers and Diverse Energy Storage Mechanisms

The inherent redox properties and complex speciation of Al-containing ions in chloroaluminate IL-based electrolytes demonstrates a wide range of potential charge carriers. These include $AlCl_4^-$, $Al_2Cl_7^-$ anions and less common cationic species $AlCl_2^+$ $AlCl^{2+}$, and Al^{3+}. This chemical diversity allows for a broad spectrum of charge storage mechanisms at the cathode, with the specific mechanism depending on the nature, structure and chemical properties of the material.

While the reversible intercalation of $AlCl_4^-$ into layered host structure remains the most observed mechanism, mainly for graphite, charge storage is not limited to intercalation. Other distinct mechanisms include:

- **Coordination/ De-coordination:** active species, often involving $AlCl_2^+$ cations form reversible bonds with specific sites within a material's framework (i.e. phentathequinone [39], tetracyanoquinodimethane [40]).
- **Conversion:** involves a complete phase transformation of the active material upon reaction with the charge carrier (i.e. CuS@C [41], Ni_3S_2@Graphene[42]).
- **Complexation:** active species form reversible complexes with the electrode material, often involving redox centres. (i.e. fullerene C_{70} [43]).
- **Surface adsorption/pseudocapacitance:** charge is stored at the surface of the electrode material, with or without bulk interaction, most common at high current densities (i.e. hyper self-protonated polyaniline/single-walled carbon nanotubes (PANI(H^+)@SWCNT) [44]).

The active charge carrier and the resulting energy storage mechanism are intricate functions of the specific cathode material's design and its interaction with the electrolyte. Despite the theoretical appeal of high capacity Al^{3+} intercalation, its high charge density would lead to strong electrostatic interactions and sluggish kinetics, limiting its reversible accommodation in most conventional host lattices. Nonetheless, a select few materials such as the Chevrel phase Mo_6S_8 [45], [46] and certain MXenes like V_2CT_X [47] have been reported to accommodate Al^{3+} cations.

In this chapter we dive deeper into the proposed mechanisms for graphite, selenium and cobalt selenides. While for the remaining materials, their performance, mechanisms, and experimental conditions are summarized in Table 3.1.

3.3.3 Graphite

The charge storage mechanism of graphite is based on the reversible intercalation and deintercalation of $AlCl_4^-$ into the graphite layers, as presented in Figure 3.2. It has become a benchmark cathode for RABs, primarily due to the ground-breaking work by Lin et al. in 2015 [19]. This study demonstrated that graphite could achieve remarkable cycling stability in acidic $AlCl_3$:EMImCl electrolytes. Prepared using a Ni foam template, maintained a capacity of nearly 60 mAh g^{-1} at 4 A g^{-1} after 7500 cycles. It also exhibited a high average discharge plateau of around 2.0 V, high coulombic efficiency, excellent rate performance and long cycle stability.

A noteworthy observation in the work by Lin et al. was the reported decrease in the discharge capacity and overall reversibility when the current density was reduced from a high rate (4 A g^{-1}) to a much lower rate (100 mA g^{-1}). For a typical battery electrode operating primarily via diffusion-limited intercalation mechanism, lower current densities usually allow more complete and favourable ion insertion, leading to higher capacities and better reversibility. This anomalous behaviour, where performance appears superior at high rates, may suggest a significant contribution from capacitive or pseudocapacitive charge storage mechanism dominating at high current densities. At such rapid rates, charge transfer might primarily occur at the surface or near surface regions of the graphite. Conversely, at lower current densities, slower, less reversible bulk interactions might become more prominent, leading to an apparent reduction in the overall reversible capacity. This observation highlights the complexity of charge storage in RABs and the importance of thorough analysis to fully differentiate the contributions to the total capacity.

The charge storage mechanism has been demonstrated to be via a staging mechanism of $AlCl_4^-$ anions intercalating into graphite layers. This process involves the sequential insertion of anions between the layers, forming well-defined stages characterized by the number of layers between intercalant layers. *Operando* X-ray diffraction studies have revealed that intercalation is reversible up to stage 4 at room temperature, and can reach stage 3 at lower temperatures, indicating a higher degree of intercalation under cryogenic conditions. These staging transitions are critical for understanding the electrochemical behaviour and capacity limits of graphite in RABs, as they directly influence ion transport, voltage profiles, and structural stability during cycling. The bulky nature of $AlCl_4^-$ also contribute to fast charge/discharge capabilities, despite the limited depth of intercalation compared to monovalent ions [48].

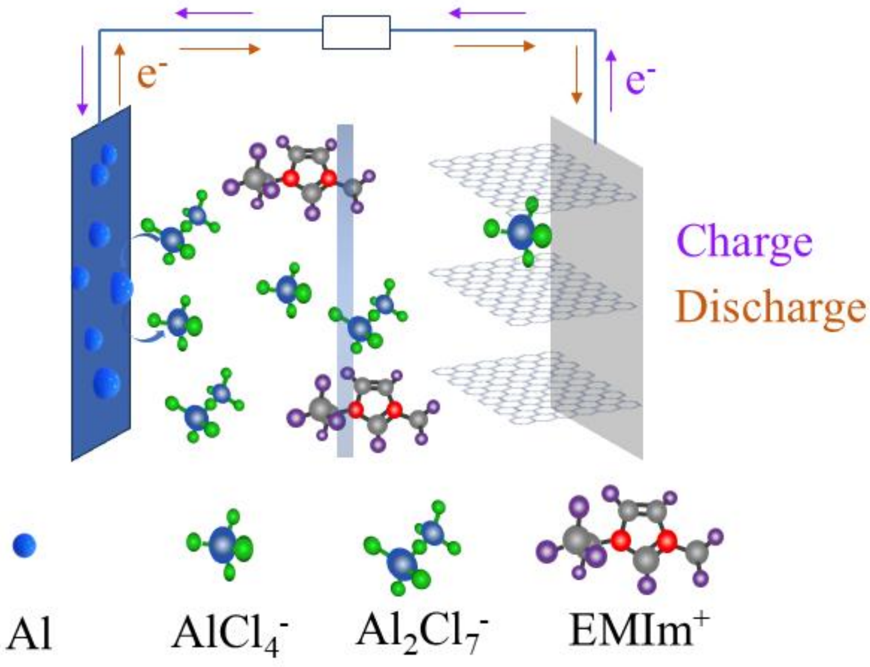

Figure 3.2 Scheme of charge storage mechanism in graphite cathodes

The stability of graphite upon cycling appears to depend on the source or type of graphite. The comparison of natural graphite (NG) to pyrolytic graphite (PG) demonstrates the dramatic expansion of NG cathode into loosely stacked flakes during charging, visible to the naked eye. This indicates inferior stability compared to PG, a difference attributed to stronger bonding between adjacent graphene sheets in PG that is absent in NG [19].

3.3.4 Selenium

The mechanism of elemental selenium (Se) cathodes has been studied in Al-Se batteries. It is generally proposed to be conversion reaction leading to soluble selenium monochloride (Se_2Cl_2), and various strategies have been reported to effectively trap this soluble product to prevent capacity fade.

For instance, the use of Se nanowires/CMK-3 composites demonstrated success in retaining the Se_2Cl_2 formed [49]. This material exhibited an initial specific capacity of 218 mAh g^{-1} at 100 mA g^{-1}. Nonetheless, a significant degradation was observed, with capacity decaying to 124 mAh g^{-1} after 50 cycles. This study was performed in coin cells, which were modified with poly(3,4-ethylenedioxythiophene) (PEDOT) and used carbon cloth as current collector [49]. Another strategy to retain soluble Se_2Cl_2 involved the use of combined Se/CMK-3 composite with CMK-3 modified separators [50]. This approach delivered a considerably high initial specific capacity of 1292 mAh g^{-1} at 1 A g^{-1}, which decreased to 651 mAh g^{-1} after 400 cycles. The exceptionally high specific capacity reported for system, considerably higher than many other reported cathodes for RABs, could be attributed to the mesoporous nature of CMK-3 and its excellent performance as an electrochemical capacitor material [51].

3.3.5 Cobalt Selenides

Two main phases of cobalt selenides have been reported as cathodes for RABs: hexagonal CoSe and cubic $CoSe_2$.

Earlier studies investigating CoSe as a cathode material for RABs initially proposed that its charge storage mechanism involved the intercalation of Al^{3+} ions [52].

$$\mathrm{CoSe} + 4\mathrm{Al_2Cl_7}^- + 3\mathrm{e}^- \rightleftarrows \mathrm{AlCoSe} + 7\mathrm{AlCl_4}^- \qquad (\mathrm{Chem.\,Eq.\,3.6})$$

This proposed mechanism, however, was accompanied by observations of rapid capacity degradation during the initial cycles. The *ex situ* X-ray diffraction (XRD) results presented evidence that appeared to contradict a reversible intercalation process. Specifically, upon charging, the XRD showed new phase formation, indicated by the emergence of new reflections at 12.71° and 27.01°, alongside amorphisation. Furthermore, these structural changes were not reversible, persisting after the discharge process.

Although the authors' interpretation suggested the changes were "caused by the irreversible intercalation of Al^{3+} ions into the CoSe", the formation of an entirely new crystalline phase, coupled with amorphisation is fundamentally inconsistent with a reversible intercalation mechanism. Such structural transformations, leading to new products, are characteristic traits of a conversion reaction or an irreversible phase transformation rather than ion insertion into an existing lattice. The discrepancy between the proposed mechanism and the presented experimental evidence highlights the complexities and ongoing challenges in accurately elucidating the true charge storage mechanism in these new battery cells.

In a similar system, cobalt diselenide ($CoSe_2$) was proposed to present a different charge storage mechanism, suggesting a "reaction with Al^{3+}" ions, explicitly differentiating it from the incorporation of $AlCl_4^-$ anions.

$$\mathrm{CoSe_2} + \mathrm{mAl^{3+}} + \mathrm{3me^-} \rightleftarrows \mathrm{2Al}_m\mathrm{Co}_n\mathrm{Se_2} + (1-\mathrm{n})\mathrm{Co} \qquad (\mathrm{Chem.Eq.}\,3.7)$$

The authors supported this claim with XRD data that showed a reversible variation in the lattice parameter upon cycling [53]. Specifically, the lattice parameter decreased from 0.5871 nm to 0.5827 nm during the initial discharge, this change was attributed to the partial substitution of large Co^{2+} ions with smaller, high-charge-density Al^{3+} ions. The lattice parameter nearly returned to its pristine value upon subsequent charge (0.5846 nm), suggesting a reversible insertion/substitution process. This study was conducted in Swagelok cell reportedly using glassy carbon collector; however, *ex situ* XRD measurements of the electrode later detected reflections associated with molybdenum, which the authors identified as originating from a Mo plate. This unexpected finding raises concerns about the reliability of the study's reported performance, as Mo current collectors are known to be susceptible to parasitic reactions in acidic chloroaluminate electrolytes.

This mechanistic claim for $CoSe_2$ also introduces several points of discussion. First, the source of the proposed Al^{3+} ions is not fully addressed, as free Al^{3+} is not considered a present species in the chloroaluminate IL-based electrolyte. Furthermore, while the reversible lattice parameter change is more consistent with an intercalation or substitution mechanism, the term "reaction with Al^{3+}" remains ambiguous. This illustrates the complex challenge of unveiling charge storage mechanism, particularly when the proposed active species (Al^{3+}) is not readily available in the electrolyte during the initial discharge. An important observation from this study regarding the degradation mechanism of $CoSe_2$ was the dissolution of cobalt species from the electrode to the electrolyte, which would lead to pulverisation of the cathode material. To mitigate this the authors proposed reduced graphene oxide layers.

A similar strategy was proposed to avoid the dissolution of Co_9S_8 and was extended to $CoSe_2$ [54]; this involved the use of MXenes nanosheets. The results showed a visible improvement in the stability of the specific capacity in the first cycles for both materials, Co_9S_8 and $CoSe_2$. However, the data for these studies are not typically reported in detail due to their utilisation of a Mo current collector, which can influence the electrochemical behaviour and comparability with other systems.

Recent investigations into composite cathode material include a study on $CoSe_2$/MXenes system which proposed a mechanism of charge storage based on the intercalation and absorption of the both $AlCl_4^-$ and Cl^-. However, a critical assessment of this work reveals several points of ambiguity. While the material is reported as a $CoSe_2$@TiO_2/MXenes composite, the TiO_2 component is not considered within the proposed charge storage mechanism [55]. Furthermore, their interpretation of XPS data attributing observed Ti-O bonds solely to TiO_2 formation overlooks the inherent Ti-O bonds present within the surface functional groups of MXenes themselves [56]. This oversight introduces considerable uncertainty regarding the precise contributions of each component and the true charge storage mechanism within such complex multi-component composites.

Other electrode materials used as cathodes for RABs, along with their initial capacity, proposed mechanism and details about the experimental setup are presented in Table 3.1.

Table 3.1 Summary of Cathode Materials for RABs

Material type	Material name	Initial capacity	Current collector/cell type	Mechanism	Ref.
Carbon-Based	Fullerenes C_{70}	750 mAh g^{-1} at 200 mA g^{-1}	Not specified	Complexation with $AlCl_4^-$	[43]
Transition metal oxides	V_2O_5	Rapid capacity loss	Mo	Intercalation of Al^{3+}	[21]
	Co_3O_4				[57]
	CuO s				[58]
	Mn_2O_4				[59]
	MoO_2				[60]
	$CoSnO_3$/C				[61]
	TiO_2				[62]
	TeO_2				[63]
Transition metal chalcogenides	S	600 mAh g^{-1} at 50 mAg^{-1}	Theoretical model	Conversion	[64]
	Mo_6S_8	160 mAh g^{-1} at 12 mA g^{-1}	Coin cell		[46]
	MoS_2	293 mAh g^{-1} at 100 mA g^{-1}	Self-standing, pouch cell	Intercalation of Al^{3+}	[65]
	NiS_2/Graphene	295 mAh g^{-1} at 100mA g^{-1}	Ta, pouch cell		[42]
	CuS	240 mAh g^{-1} at 20 mA g^{-1}	Ta, pouch cell		[66]
	NiS	100 mAh g^{-1} at 200 mA g^{-1}	Ta, pouch cell	Conversion	[17]
	$Cu_{1.8}Se$	410 mAh g^{-1} at 2 A g^{-1}	Not specified		[67]
	VSe_2	650 mAh g^{-1} at 100mA g^{-1}	Not specified	Not specified	[68]
	Sb_2Te_3	102 mAh g^{-1} at 500 mA g^{-1}	Ta, pouch cell	Conversion	[69]
MXenes	V_2CT_X	380 mAh g^{-1} at 10 mA g^{-1}	Mo	Intercalation of Al^{3+}	[47]

3.4 Passive Components

Even though passive components constitute around 20% of the battery's total weight, they are considerably less studied across all batteries, including LIBs [70], with RABs being no exception. These components play diverse roles but collectively ensure cell integrity. When properly engineered and designed, they can significantly enhance overall performance by improving charge conductivity, material stability, and homogeneity in the distribution of active species.

Significant challenges in RABs arise from the highly acidic chloroaluminate electrolyte, which is essential for achieving reversible Al plating and stripping. This acidic environment leads to high corrosivity, affecting not only the stability of the positive electrode active material but also other battery components, potentially causing corrosion in current collectors, or positive electrode dissolution, ultimately leading to cell failure [8].

3.4.1 Current collector

As its name implies, the current collector is an electronically conducting material responsible for rapid transfer of electrons between the active material and the external circuit. An ideal current collector should possess excellent electronic conductivity, low density, low weight, and easy processability. While also demonstrating stability in contact with the electrolyte and other cell components.

In RABs, it is well-documented that current collectors face specific issues. For instance, common materials used in LIBs, such as Mo, copper, Ni or SS, encounter significant corrosion problem in acidic chloroaluminate IL-based electrolytes, making them unsuitable for direct transfer to RABs. For example, Mo has demonstrated dissolution in IL electrolyte, confirmed by the paramagnetism and ICP-OES analysis after soaking [71]. Ni also exhibited significant surface changes upon soaking, with the formation of Ni oxides hinting at spontaneous galvanic corrosion even without applied current [72]. These findings are applicable not only to current collectors but also to other metallic cell parts, such as coin cell casings such as exemplified in an early study using V_2O_5 positive electrode in a coin cell configuration [21] later revealed that iron and chromium from the SS were oxidized to form iron chloride ($FeCl_3$) and chromium chloride ($CrCl_3$), leading to specific capacity being erroneously attributed to V_2O_5 [73]. Corrosion of the current collector not only leads to false capacity reading but also jeopardizes the cell integrity.

To mitigate metallic component corrosion, scientists have proposed strategies such as using corrosion inhibitors in the electrolyte. These compound, introduced in small amounts, are designed to absorb onto the metal surface, often via functional groups like -C=N- in an imidazole ring, preventing metal dissolution and corrosion without affecting the electrochemical activity. While not extensively studied in RABs, various acidic ionic liquid corrosion inhibitors have been presented and offer a promising starting point [74]. Another strategy involves applying corrosion-resistant layers on current collectors or battery casings, with examples including PEDOT [49], titanium nitride (TiN) [75], or chromium nitride (Cr_2N) [76].

3.4.2 Binder

The primary function of a binder is to maintain the mechanical integrity of the electrode by connecting all the components among themselves and to the current collector, thereby preventing active material pulverisation or detachment. A good binder should be stable in contact with the electrolyte and other components of the cell, possess low crystallinity (as amorphous regions facilitate electrolyte penetration [77]), exhibit strong adhesion, resist dissolution into the electrolyte and ideally, have good electrical conductivity.

Polymeric binders interact with active material particles in three states: a bonded polymer layer that diffuses into the pores for mechanical interlocking, a fixed polymer layer that adheres adjacent particles, and an excessive polymer layer surrounding the fixed layer. While the properties of fixed and excessive layers are inherent to the polymer, the bonded layer's properties depend on the interface interactions between the polymer and substrate [78].

Given that many RAB materials are adapted from LIBs applications, where poly(vinylidene fluoride) (PVDF) binders are widely used for cathodes, it is important to note that direct technology transfer is often not straight forward. Researchers have reported a darkening of $AlCl_3$:EMImCl electrolyte upon PVDF addition [79], though poly(tetrafluoroethylene) (PTFE) showed no such reaction., suggesting PTFE's grater suitability for RABs with the electrolytes[80]. Further studies revealed that $Al_2Cl_7^-$ induces dehydrofluorination and dehydrochlorination of PVDF, forming amorphous carbon that paradoxically protects graphite and enhance electrode surface area and conductivity [81].

Conversely, water-based binders like CMC have demonstrated easy dissolution in chloroaluminate ionic liquid electrolytes, compromising electrode integrity [79]. Sodium alginate (Na Alg) has shown satisfactory adhesion strength, chemical stability, low electrochemical polarisation, and fast reaction kinetics when used in graphite cathodes, though this particular study employed Mo as current collector [82]. Binder free electrodes, such as Ni foam-based, have also been proposed but the inherent concern about the Ni corrosion remains a challenge, especially considering that extremely high capacities are reported compared to the electrodes fabricated with binders [80]. Similarly, binder-free electrodes based on carbon nanofibers were studied using Mo as a current collector [83].

3.4.3 Separator

Separators in RABs primarily fulfil two functions: electronically isolating the positive and negative electrodes to ensure electron transfer solely via the external circuit, and allowing the efficient diffusion of chloroaluminate species, which serve as the active charge carriers in the electrolyte. Based on these requirements, common LIB separators like Celgard® are often unsuitable due to their thinness, which may not adequately hold the active species, and their limited permeability to bulky chloroaluminate species, hereby hindering Al plating/stripping and limiting battery capacity. Consequently, glass fibre is the most employed separator in RABs.

Relatively few studies specifically focus on RABs separators, likely due to their less remarkable performance contributions compared to active materials and limited comparative options. Nonetheless, some research has explored alternatives. For instance, electrospun polyacrylonitrile (PAN) demonstrated a lower interface resistance of approximately 3 kΩ, which remained stable over time, compared to glass fibre separators, which oscillated between 5 and 7 kΩ over a 15-day period [84]. When cells with graphite cathode using PAN separators were compared to those with glass fibre, the PAN separator showed a slight improvement in the specific capacity (around 5 mAh g^{-1}) [84]. This study used a Swagelok cell configuration but does not report on the current collector. Similar benefits of smaller overpotentials and resistance were observed for polyimide separators, although the specific capacity of cells with graphite electrodes remained nearly identical [85].

Modification strategies for glass fibre separators have also been proposed, such as incorporating porous carbon (CMK-3) on the surface of the separator to trap and prevent the migration of active materials to the anode. For instance, a CMK-3 modified separator, combined with a MXenes coating, led to an increase in both initial and stable specific capacity, while the capacity loss behaviour remained like that of unmodified separators. However, specific performance values from this study are not detailed here as Mo was used as the current collector [86].

A different behaviour was observed in CMK-3- selenium, where modified separators (with CMK-3) delivered a considerable improvement in both initial specific capacity and cycling stability compared to a regular separator [50]. (Note: this material's exceptional specific capacity was discussed in the cathode section 3.3.4).

3.5 Critical Technical Challenges and Future Outlook for RABs

The advancement of RABs as next-generation energy storage systems centres on a comprehensive understanding of their component interactions, dynamic behaviours, and degradation mechanisms. Among the most pressing challenges is the corrosive nature of chloroaluminate IL-based electrolytes, which significantly limits the practical implementation of RABs.

3.5.1 Challenges in Cell Components

The aggressive chloroaluminate IL-based electrolyte affects nearly all cell components (see Sections 3.1, 3.3, 3.4 and 3.4). Metallic parts, including current collectors and cell casings, are highly susceptible to corrosion. Beyond these, active electrode materials and auxiliary components face distinct degradation pathways.

A particularly unresolved issue is the development of reliable reference electrodes for RABs. Unlike aqueous systems, where standard electrodes such as Ag/AgCl or saturated calomel (Hg/Hg_2Cl_2) are used, ionic liquids present unpredictable behaviour. Pseudo-reference electrodes, such as silver wire, activated carbon, or metal alloys—often degrade in the electrolyte, leading to potential drift. Even Al foil, a seemingly compatible choice, suffers from instability due to uncontrolled removal of its passivation layer. This persistent lack of a stable reference electrode represents a critical gap in RAB research, hindering accurate electrochemical characterisation [13]

The Al anode also presents challenges. Although Al dendrites are less likely to cause short circuits than lithium dendrites, they can still lead to capacity loss by forming inactive Al deposits. The native oxide layer may suppress dendrite growth, and detached dendrites may reduce risk [124], but their unpredictable formation and the influence of oxide thickness remain poorly understood. These factors directly impact long-term cycling stability and coulombic efficiency, making dendrite control a key area of ongoing research.

On the anode, rapid degradation is often observed due to the dissolution and migration of active materials in the electrolyte. This limits overall cyclability. Additionally, the electrolyte's extreme sensitivity to moisture introduces further complications. The theoretical reduction potential of −1.66 V vs. SHE of Al leads to hydrogen evolution reaction (HER) triggered by trace water [125]. HER competes with Al plating, consumes charge carriers, and generates gas, posing safety risks and potentially forming insulating phases. Standard water-tracking methods such as Karl-Fischer titration or gas chromatography are problematic due to the corrosive nature of the electrolyte, which can damage sensitive components like platinum electrodes or stainless steel.

3.5.2 Challenges in Characterisation

The corrosive electrolyte also complicates battery characterisation, even at the laboratory scale. Electrolyte preparation, storage, and prolonged exposure can damage gloveboxes and other equipment.

Electrochemical cell design is similarly constrained. Coin cells, widely used in other battery chemistries, are generally unsuitable for RABs due to material incompatibility and limited adaptability for *in situ/operando* techniques. Alternative setups include custom Swagelok cells with inert leads (e.g., W or glassy carbon), glass cells, TSC surface cells made of PEEK, and pouch cells. Among the few successful real-time studies, one notable example investigated $AlCl_4^-$ intercalation in graphite using a custom PEEK cell [34].

These design limitations restrict the feasibility of advanced characterisation. Techniques requiring transparent windows (i.e., synchrotron-based methods) are difficult to implement. While pouch cells offer some compatibility, high-resolution data often require specialized modifications.

Beyond setup, data interpretation presents its own challenges. *Ex situ* techniques can introduce artifacts, leading to misinterpretation of the battery's true operational state. For example, relying solely on XPS to confirm Al^{3+} as the charge carrier can be misleading, as Al in chloroaluminate ions shares similar binding energies. Similarly, changes in lattice parameters may be overemphasized as evidence of Al^{3+} insertion, while the loss of crystallinity, potentially indicating new amorphous phases, is overlooked. These examples underscore the need for multimodal characterisation strategies and a deep understanding of each technique's limitations.

3.5.3 Waste Disposal and Environmental Concern

Environmental sustainability is a core motivation for next-generation battery research, and RABs present unique challenges in this regard. Upon exposure to air, the chloroaluminate electrolyte reacts with moisture to produce corrosive and pungent HCl vapours. As a result, cell disassembly must be performed under a fume hood or in an inert glovebox with proper ventilation.

Handling and disposal of these acidic and potentially toxic components require specialized protocols, beyond standard battery waste management practices. While some procedures are analogous to other chemistries, the reactive nature of the electrolyte demands stricter controls to ensure safety and environmental compliance.

3.6 Knowledge Gaps: Contribution of this Research

The preceding literature review highlights significant advancements in RABs, including the development of room-temperature electrolytes and the exploration of stable electrode materials. Nonetheless, a thorough analysis of the existing of literature reveals several critical knowledge gaps that hinder the rational design of high-performance and commercially viable RAB systems.

3.6.1 Ambiguous and Contradictory Charge Storage Mechanisms in Cobalt Selenide-Based Cathodes

Despite their promising electrochemical performance, the precise charge storage mechanisms of cobalt selenides in RABs remain ambiguous and often contradict presented experimental evidence. For example, an Al^{3+} intercalation mechanism proposed for CoSe is inconsistent with *ex situ* XRD data that clearly indicates new phase formation and significant amorphisation [52]. Furthermore, other interpretations have overlooked the presence of side products or artifacts from passive components leading to an incomplete or misleading understanding of the true charge storage pathway.

This dissertation directly addresses these critical mechanistic discrepancies by providing a real-time investigation into the electrochemical transformations of CoSe cathodes. Employing advanced *in situ* and *operando* synchrotron-based X-ray techniques, this work offers unprecedented insights, it reveals that the primary charge storage is facilitated by the reversible redox of selenium caused by an initial phase transition and amorphisation.

3.6.2 Unexplored Multifunctionality and Voltage-Dependent Electrochemical Behaviour of MXenes in RABs Systems

While MXenes have emerged as versatile materials, their exploration in RABs has predominantly focused on enhancing the stability of active materials by mitigating the dissolution and migration of species. A comprehensive understanding and systematic exploration of their broader, multifunctional roles in RABs remains largely unexplored. Specifically, their potential as versatile components in current collectors, binders, or functionalized separators, has received limited attention. Moreover, the detailed influence of operating conditions on MXenes specific electrochemical roles and their interaction within the highly corrosive RAB environment are not yet fully understood.

This dissertation directly addresses these limitations by systematically investigating the multifaceted roles of MXenes in RABs, extending beyond their conventional use for active material stabilisation. This work explores the novel application of MXenes as highly versatile components, including their novel integration as current collectors and within modified separators, roles previously underexplored in this chemistry. Crucially, this thesis elucidates the voltage-dependent electrochemical behaviour of MXenes, demonstrating that they act as stable conductive platforms at lower voltages but exhibit active charge storage at higher potentials

3.6.3 Methodological Barriers to Comprehensive *Operando* Characterisation in RABs

Despite the critical importance of *operando* characterisation for unravelling complex reaction mechanisms, it is widespread and truly comprehensive application in RABs remains significantly underutilized. This arises from fundamental methodological barriers, primarily due to the highly corrosive nature of chloroaluminate electrolytes and the resulting severe constraints on compatible cell materials and designs. These challenges often force a reliance on *ex situ* analyses, which risk introducing artifacts and cannot fully capture real-time, dynamic processes essential for a complete and understanding of RABs.

This dissertation directly addresses these methodological barriers by developing and validating *operando* and *in situ* electrochemical cell designs specifically for RABs. This work demonstrates the successful implementation of new cell configurations compatible with the aggressive corrosive environment, enabling the reliable application of X-ray techniques to track real-time structural and chemical transformations within operating RABs.

4 Experimental Methodology: Building and Analysing the System

A robust and well-defined experimental framework is essential for generating accurate, reproducible, and relevant data, particularly in the complex systems of electrochemical energy storage, where the material performance is tightly linked to specific conditions. Much like Sherlock Holmes or Hercule Poirot, who meticulously piece together complex cases through observation, forensic analysis, and the systematic collection of every detail, a precise methodology in scientific research serves as the indispensable backbone for uncovering truths and complex phenomena within a system.

In this chapter a transparent overview of each experimental step is provided, from the selection of raw materials to the execution of advanced characterisation techniques. The structure is as follows:

- Section 4.1: Materials and chemicals.
- Section 4.2: Material synthesis protocols.
- Section 4.3: Fabrication of cell components.
- Section 4.4: Assembly of cells for electrochemical evaluation.
- Section 4.5: Electrochemical testing procedures.
- Section 4.6: Material and structural characterisation.
- Section 4.7: *In situ* and *operando* characterisation.

4.1 Materials and Chemicals

All the reactants, chemicals, and materials utilized for synthesis and characterisation in this study are listed in Table 4.1

Table 4.1 Chemicals and materials used for experiments

Chemicals	**Abbreviation/chemical formula**	**Purity**	**Supplier**
Aluminium chloride	$AlCl_3$	99.99 %	Sigma Aldrich
1-ethyl-3-methylimidazolium chloride	EMImCl	95 %	Sigma Aldrich
Cobalt nitrate hexahydrate	$Co(NO_3)_2 \cdot 6H_2O$	98 %	Sigma Aldrich
2-Methylimidazole	$C_4H_6N_2$	99 %	Sigma Aldrich
Selenium	Se	99 %	Sigma Aldrich
Carbon black		<99 %	MTI corporation
Graphite MEChANO-CaP 1P1		<99 %	H.C. Carbon GmbH
Multiwalled carbon nanotubes	CNT	<90 %	Sigma Aldrich
Cobalt (II) sulphide	CoS	99.5 %	Fisher scientific
Hydrofluoric acid	HF	50 %	Acros Organics
Hydrochloric acid	HCl	12 M	Fisher Scientific
Titanium carbide	TiC	99.5 %	Alfa Aesar
Titanium	Ti	99.5 %	Alfa Aesar
Aluminium	Al	99.5 %	Alfa Aesar
Binders	**Abbreviation/chemical formula**	**Size**	**Supplier**
Poly(acrylonitrile)	PAN	Mw: 150000	Sigma Aldrich
Carrageenan	Carr		Sigma Aldrich
Carboxy methyl cellulose	CMC		Sigma Aldrich
Poly(vinylidene cellulose)	PVDC	<180 μm	Goodfellow
Solvents	**Abbreviation/chemical formula**	**Purity**	**Supplier**
Deionized water	DI water		
1,2-difluorobenzene	$C_6H_4F_2$		Apollo Scientific
Dimethylsulfoxid	DMSO	100 %	VWR (Avantor)
N, N-Dimethylformamide	DMF	99.9 %	VWR (Avantor)
Ethanol	C_2H_6O	99.8%	Sigma Aldrich
Other materials	**Thickness, Purity**		**Supplier**
Aluminium foil	0.075 mm, 99.0 %		Goodfellow
Glass fibre separator /D			Whatman
Celgard			
Tungsten	0.025 mm, 99.96 %		Goodfellow
Carbon paper (C Paper)	120 μm		Quintech
Aluminium case for pouch cell			MTI

4.2 Material Synthesis and Preparation

The preparation of the electrolyte, active materials, and other cell components are described in the following subsections.

4.2.1 Preparation of Ionic Liquid Electrolyte

The ionic liquid electrolyte ($AlCl_3$:EMImCl) was prepared in an argon-filled glovebox (MBraun). Stoichiometric amounts of $AlCl_3$ and EMImCl were combined to achieve a 1.3:1 molar ratio. Due to the exothermic nature of the reaction, small amounts of each component were alternately added to a glass vial under constant stirring, maintaining the desired ratio and preventing excessive heat generation. The electrolyte was allowed to stabilize for at least 24 hours before use and was utilized within 10 days of preparation.

4.2.2 Synthesis of ZIF-67

The Zeolitic imidazolate Metal-Organic Framework (MOF) ZIF-67 was synthesized following the method described by Qian et al. [89]. Solution 1 was prepared by dissolving 0.45 g of $Co(NO_3)_2{\cdot}6H_2O$ (1 equivalent) in 3 mL of deionized (DI) water. Solution 2 was prepared by dissolving 5.5 g of 2-methylimidazole (43 equivalents) in 20 mL of distilled water. Solution 1 was rapidly added to solution 2 under continuous stirring, resulting in the immediate formation of a purple precipitate. The mixture was stirred for 18 hours, after which the precipitate was collected via centrifugation, washed three times with a mixture of equal volumes of deionized water and methanol, and vacuum-dried at 80°C for 24 hours.

4.2.3 Synthesis of CoSe

CoSe was synthesized using ZIF-67 as a precursor, based on the method by Xing et al. [52]. Dried ZIF-67 was ground with Se powder in a molar ratio of 1:2. The mixture was transferred to an alumina crucible and heated in a tubular furnace, ramping the temperature at 5°C min^{-1} to 350°C and holding for 2 hours to form of $CoSe_2$. A second annealing step was performed at 800°C for 2 hours. During this process, the organic ligands decomposed into carbon, and the $CoSe_2$ was converted to CoSe. Excess selenium sublimated and condensed at the furnace exhaust. **Caution**: It is recommended to use an appropriately long tube and to regularly observe the exhaust, as sublimated selenium may obstruct the system and pose a safety hazard.

4.2.4 Synthesis of Ti_3AlC_2 MAX Phase

The Ti_3AlC_2 MAX Phase was synthesized by sintering a mixture of TiC, Ti, and Al powders in a 2:1.25:2.2 molar ratio at 1380°C for 2 hours under argon flow. Both the heating and cooling rates were maintained at 3°C min^{-1}. The resulting product was a block of Ti_3AlC_2 MAX phase.

4.2.5 Synthesis of $Ti_3C_2T_X$ MXenes

$Ti_3C_2T_X$ MXenes were synthesized via a multi-step etching and delamination process following the method by Mathis et al. [90].

4.2.5.1 MAX phase milling and purification:

The as-sintered Ti_3AlC_2 MAX phase block was milled into a fine powder using a TiN-coated milling bit. The powder was washed with 9 M HCl to remove impurities, then repeatedly washed with DI water until a neutral pH of 7 was achieved. The powder was dried in a vacuum oven at 80°C and sieved through a 400-mesh (38 μm) sieve.

4.2.5.2 Etching

To prepare multi-layer $Ti_3C_2T_X$ MXenes, 1g of purified Ti_3AlC_2 MAX powder was mixed with 20 mL of an etchant solution (6:3:1 volume ratio of 12 M HCl, DI water, and HF). The mixture was stirred at 350 rpm at 35°C for 24 hours. The etched product was washed with DI water until the pH reached 6.

4.2.5.3 Li-ion intercalation

The multi-layer $Ti_3C_2T_X$ MXenes was dispersed in 50 mL of 0.5 M LiCl solution and stirred at 400 rpm for 4 hours to facilitate the Li ion intercalation. The product was washed with DI water to remove excess Li ions.

4.2.5.4 Delamination and storage

The Li-intercalated multi-layer $Ti_3C_2T_X$ MXenes was delaminated into single layer sheets via mechanical agitation. The delaminated single-layer $Ti_3C_2T_X$ MXenes was collected by repeated centrifugation and collection of supernatants. These supernatants, containing the delaminated single-layer MXenes, were stored in a refrigerator for future use.

4.3 Fabrication of Battery Components

This section details the fabrication procedures for the various components comprising the RABs, including current collectors, electrodes, and modified multilayered separators.

4.3.1 Electrodes

Electrodes were prepared by doctor blading slurries of the active materials onto current collectors. Two distinct electrode formulations were used:

4.3.1.1 $Ti_3C_2T_X$ as Binder/Conductive Agent

Slurries were prepared with 80 wt.% active material and 20 wt.% $Ti_3C_2T_X$, which served as both binder and conductive additive.

4.3.1.2 Conventional binders

Slurries consisted of 80 wt.% active material 10 wt.% conductive carbon black, and 10 wt.% binder: PAN (for CoSe and CoS), or carrageenan (carr, for CoS and graphite).

Table 4.2 Summary of electrodes used

Active material	Binder	Current collector
CoSe	PAN	C Paper
	Carr	C Paper
	CMC	C Paper
Graphite	Carr	C Paper
	Carr	$Ti_3C_2T_X$

The prepared slurries were coated onto either a porous C Paper or $Ti_3C_2T_X$ current collectors (Section 4.3.2), according on the experimental design. Electrodes were cut into

2×2 cm^2 squares for pouch cells or 12 mm diameter discs for Swagelok cells. All electrodes were vacuum dried at 90°C for 12 hours prior to cell assembly.

For better understanding the electrode materials binders and current collectors are summarized in Table 4.2.

4.3.2 Current Collector

Free-standing $Ti_3C_2T_X$ current collector film was fabricated from delaminated $Ti_3C_2T_X$ dispersion. The dispersion was cast onto the surface of Celgard and dried at room temperature. Once dry, the $Ti_3C_2T_X$ film was carefully peeled off the Celgard substrate and further dried in a vacuum oven at 90°C for 12 hours.

4.3.3 Modified Separators

Modified separators were prepared by fabricating composite membranes via vacuum-assisted filtration of aqueous dispersions containing $Ti_3C_2T_X$, and carbon nanotubes (CNT). The solid components were dispersed in DI water. The specific compositions for each separator type are as follows: for $Ti_3C_2T_X$-CNT separator 7.2 mg $Ti_3C_2T_X$, 7.2 mg CNT in 36 mL water. For $Ti_3C_2T_X$ separator 7.2 mg $Ti_3C_2T_X$ in 36 mL water.

Each mixture was filtered through a 5 cm diameter Whatman glass fibre filter. The resulting membranes were dried at 60°C for 24 hours, cut into 12 mm diameter discs for Swagelok cells or 2.5×2.5 cm^2 squares for pouch cells, and vacuum-dried at 60°C for 12 hours before use.

4.4 Cell Assembly

This section describes the assembly procedures for the various electrochemical cells used in this study.

4.4.1 Swagelok Cells

Two-electrode Swagelok cells (see Figure 4.1 a) were assembled inside an argon-filled glovebox (with H_2O and O_2 levels below 0.1 ppm). To prevent corrosion from the reactive ionic liquid electrolyte Teflon was used for the cell body and rings, and tungsten (W) was used for the current collector rods. The cell stack typically consisted of the working electrode, two separators (either one modified and one regular, or two regular separators), 250 µL, and the high-purity Al foil counter electrode. The cell was then sealed.

Specific cell configurations were employed for certain investigations. For example, some cells were assembled without active material, using only current collectors to investigate their behaviour (Section 7.2), while in other configurations, a positive electrode was omitted, with the modified separator serving as the active positive electrode (Section 7.3).

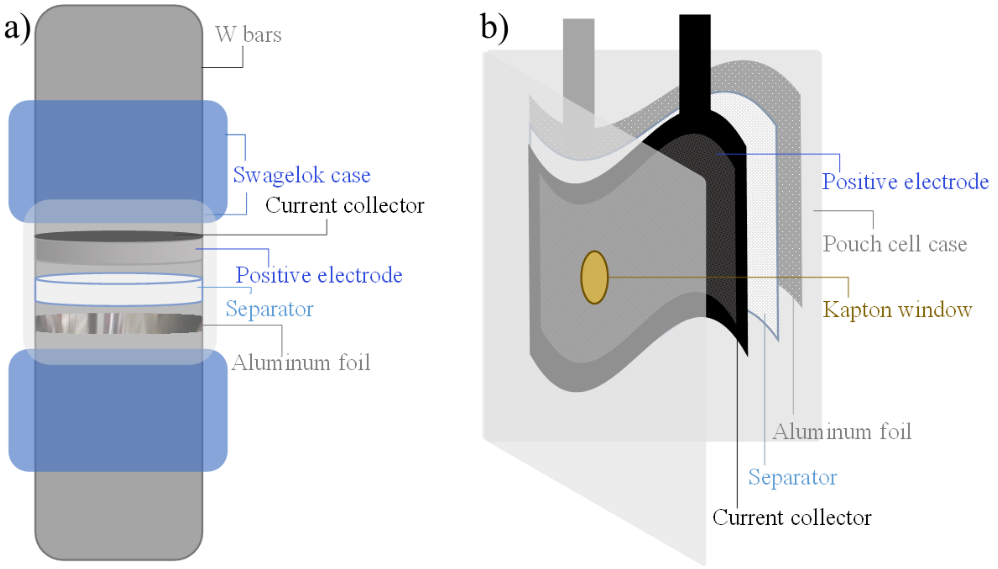

Figure 4.1 Scheme of the cells employed in this research work: a) Swagelok cell, b) pouch cell

4.4.2 Pouch Cells

Pouch cells (see Figure 4.1 b) were assembled using commercially available ALF100210 pouch cell cases, which feature a polypropylene inner layer and a polyamide outer layer. The cases were pierced with 12 mm diameter holes, which were sealed with Kapton tape. A square working electrode with an extended current collector tab was placed inside the pouch cell pocket, followed by two 2.5 × 2.5 cm separators and 800 µL of electrolyte. A high-purity Al foil counter electrode, also with an extended strip for external connection, was then added. The cell was hermetically sealed.

4.5 Electrochemical Characterisation

Electrochemical measurements, were carried out in a climate chamber maintained at 25°C. A MPG3 multi-channel potentiostat/galvanostat (Bio-logic Science Instrument, France), equipped with EC-Lab® software, was used for all experiments.

4.5.1 Cyclic Voltammetry Measurements

Cyclic voltammetry (CV) measurements were performed to investigate the electrochemical behaviour of the active material and cell components.

CoSe (Chapter 5): CV was performed at a scan rate of 20 mV s^{-1} over a cell voltage range from 0.3 V to 2.3 V.

Graphite (chapter 7): CV was performed at a scan rate of 0.5 mV s^{-1} over a cell voltage range from 0.3 V to 2.3 V.

CoS (Chapter 7): CV measurements were performed at scan rates of 0.5 and 1 mV s^{-1} over a cell voltage range of 0.4 to 1.8 V.

$Ti_3C_2T_X$, C paper, and Mo current collectors (Chapter 7): CV measurements were conducted at scan rates of 0.5 mV s^{-1} over cell voltage ranges of both 0.4 V to 2.3 V and 0.4 to 1.8 V.

Statistical analysis was performed, and the anodic charge was calculated for 6 samples of $Ti_3C_2T_X$ current collector. These results were compared to single measurements obtained from C Paper and Mo current collectors.

4.5.2 Chronoamperometry Measurements

Chronoamperometry (CA) measurements were conducted under two primary setups:

Ex situ and post-treatment studies: The positive electrode was polarized at a constant cell voltage of 2 V for 2 hours. Following polarisation, samples underwent various post-treatment procedures: some were removed for *ex situ* SEM analysis, others were subjected to galvanostatic charge/discharge with potential limitation (GCPL) cycling, and in certain cases, the electrolyte and/or Al foil counter electrode were replaced prior to further GCPL cycling.

In situ X-Ray Absorption Spectroscopy (XAS) studies: CA was employed to polarize the positive electrode at a series of predefined cell voltages: 1.2 V, 1.45 V, 1.7 V, 1.95 V, 2.0 V, 2.5 V, 2.0 V, 1.95 V, 1.7 V, 1.2 V, 0.95 V, 0.7 V, 0.45 V, 0.2 V, 0.45 V, 0.7 V, 0.95 V, and 1.2 V. Each potential step was maintained for 11.5 minutes to ensure electrochemical stabilisation and enable concurrent XAS measurements.

4.5.3 Galvanostatic Charge/Discharge Cycling with Potential Limitation Measurements (GCPL)

GCPL measurements were performed under various conditions:

CoSe (Chapters 5 and 6): Measurements were performed within a cell voltage of 0.3 V to 2.3 V at a current density of 1 A g^{-1}, with additional tests were performed at 25 mA g^{-1}.

CoSe (Chapter 6, *operando*): *Operando* XAS and Synchrotron Radiation Diffraction (SRD) measurements were conducted during GCPL cycling at 1 A g^{-1} within a cell voltage window of 0.1 to 2.2 V.

Graphite (Chapter 7): GCPL was performed within a cell voltage of 0.3 V to 2.3 V at a current density of 60 mA g^{-1}.

For CoS (Chapter 7): GCPL was performed within a cell voltage of 0.4 V to 1.8 V at a current density of 25 mA g^{-1}.

Modified separators (Chapter 7) :GCPL measurements were conducted within a cell voltage window 0.4 to 2.3 V at a current density of 60 mA g^{-1} based on the mass of $Ti_3C_2T_X$ in the separators.

The derivative of the galvanostatic curves (dC/dV vs. V) is reported throughout the thesis to highlight subtle changes in the potential profile and identify plateaus.

4.5.4 Electrochemical Impedance Spectroscopy (EIS) Measurements

Electrochemical Impedance Spectroscopy (EIS) measurements were conducted at open circuit voltage (OCV) and after the final discharge cycle, utilizing a single sine perturbation method. The DC potential was maintained at OCP, with an AC excitation voltage of 10 mV. No delay was applied before measurement. The frequency sweep ranged from 0.1 MHz to 30 mHz, with seven data points collected per decade. The potentiostat pulse width was set to 4, and the number of averages was 3.

4.5.5 Linear Sweep Voltammetry Measurements

Linear sweep voltammetry (LSV) was performed in cells with inert cathodes (C Paper) and pristine electrolyte, electrolyte pre-treated by soaking active material or binders. Scan rates of 0.5 V s^{-1} in a voltage interval of 0.1 to 2.5 V were applied.

4.6 Material and Structural Characterisation

This section outlines the suite of techniques employed to characterize both pristine synthesized materials and commercial compounds, as well as *ex situ* analyses performed on battery components following electrochemical cycling or polarisation.

4.6.1 X-ray Diffraction

The crystalline structure and phase purity of the synthesized materials were determined by XRD. Measurements were performed at room temperature with a Stoe Sadi P diffractometer equipped with Mo-Kα-radiation (λ = 1.5406 Å), operating in flat-sample transmission mode Phase identification was performed using the Inorganic Crystal Structure Database (ICSD), and Rietveld refinement of the diffraction patterns was carried out using the FullProf software package.

Ex situ XRD was performed on pristine electrodes and on electrodes of CoSe (Chapters 5 and 6), and $Ti_3C_2T_X$ (Chapter 7) after soaking in the electrolyte or cycling. Prior to analysis, the electrodes were washed with 1,2-difluorobenzene to remove residual electrolyte.

4.6.2 Scanning Electron Microscopy and Energy-Dispersive X-ray Spectroscopy

Surface morphology and elemental composition were analysed using a thermal field emission scanning electron microscope (FE-SEM, Carl Zeiss SMT AG) operated at 5.00 kV, equipped with an Energy-Dispersive X-ray (EDX) spectroscope (Quantax 400 SDD, Bruker). Samples were mounted on steel holders using carbon tape.

Pristine electrodes of various compositions were characterized, including: CoSe with different binders, Graphite with carr and $Ti_3C_2T_X$, graphite coated on C Paper and $Ti_3C_2T_X$ Al foil.

Ex situ SEM/EDX analysis was also performed on Al foil electrodes after 20 and 60 galvanostatic cycles with CoSe using conventional and modified separators. Additionally, a CoSe electrode with PAN binder was polarized at 2 V for 2 hours prior to analysis. All cells were disassembled in an argon-filled glovebox, and electrodes were washed with 1,2-difluorobenzene and vacuum-dried before characterisation.

4.6.3 Physical Property Measurements Systems

The electrical resistance of $Ti_3C_2T_X$ current collector layers was measured using a Physical Property Measurement System (PPMS). A four-probe configuration was employed to assess resistance as a function of temperature over a range of 5 to 300 K with an incremental step size of 1 K. Measurements were performed under an amplitude excitation of 10 mA and frequency of 0.4 Hz.

These measurements aimed to quantify the intrinsic electrical properties of $Ti_3C_2T_X$ films and evaluate their temperature-dependent behaviour, which is critical for their application as current collectors.

4.6.4 X-ray Absorption Spectroscopy

XAS measurements were conducted to probe the local structure and oxidation state of specific elements. Pristine CoSe as analysed at the Se and Co K-edges, while $Ti_3C_2T_X$ was examined at the Ti K-edge. All spectra were processed using the Demeter software suite.

4.6.5 Thermogravimetric Analysis

Thermogravimetric analysis (TGA) was performed using a STA 449 C Jupiter thermobalance (Netzsch-Gerätebau GmbH). Samples were heated from room temperature to 1000°C at a rate of 5°C min^{-1} under an air atmosphere.

The primary objectives were to determine the carbon content in CoSe (originating from the MOF precursor ligands) and to assess the thermal stability of materials in oxidative environments. Mass loss was recorded as a function of temperature, and the derivative thermogravimetric analysis (DTGA) curve was calculated to identify decomposition events and their corresponding temperatures.

Differential Thermal Analysis (DTA) was not included due to the absence of a suitable blank reference for the sample holder. However, the DTGA curve provided sufficient resolution for interpreting thermal decomposition kinetics.

4.6.6 Inductively Coupled Plasma - Optical Emission Spectroscopy (ICP-OES)

The dissolution of cobalt from CoSe into the electrolyte was quantified using ICP-OES. Measurements were performed with an OPTIMA 4300DV (Perkin-Elmer) equipped with an Echelle polychromator and a two-dimensional CCD array solid-state detector.

To prepare the samples, CoSe electrodes were soaked in the electrolyte for 12 hours. Both the pristine electrolyte and post-soaking electrolytes after soaking were analysed to determine the concentration of dissolved Co and Se.

4.6.7 Raman spectroscopy

Raman spectra were collected using a LabRam Evolution HR spectrometer (HORIBA Jobin Yvon) with a 633 nm laser excitation wavelength. Measurements were performed over a spectral range of 100 - 4000 cm^{-1}.

Ex situ Raman analysis was conducted on pristine CoSe and $Ti_3C_2T_X$ electrodes. As well as after soaking, CA for 2 h at 2 V and 200 cycles. Cells were disassembled in a glovebox, and the electrodes were washed with 1,2-difluorobenzene and vacuum dried prior to characterisation, additional measurements were done without washing the electrolyte.

4.7 *In Situ* and *Operando* Characterisation

This section describes the advanced in situ and *operando* characterisation techniques employed to investigate electrochemical processes in real time or under realistic operating conditions. These methods provide critical insights into the structural, electronic, and chemical changes of the materials occurring during battery operation.

4.7.1 *In Situ* X-ray Absorption Spectroscopy

In situ XAS measurements were conducted to examine the local electronic and structural environment of specific elements during electrochemical cycling. Measurements were performed at the Se K-edge for CoSe, under a series of predefined potential steps applied via CA (see Section 4.5.2). All spectra were analysed using the Demeter software suite.

4.7.2 *Operando* X-ray Absorption Spectroscopy at Synchrotron

Operando XAS measurements focusing on the Co K-edge, at Deutsches Elektronen-Synchrotron (DESY), beamline P65. These experiments investigated the oxidation state and coordination environment of cobalt during continuous battery operation.

A custom designed *operando* pouch cell (See Section 4.4.2). The cells were cycled under specific galvanostatic conditions described in Section 4.5.3. Spectra were plotted using Python and processed using the Demeter software suite.

4.7.3 *Operando* Synchrotron Radiation Diffraction

Operando SRD was employed to monitor the structural changes of the active material during electrochemical cycling. High-energy synchrotron radiation ($\lambda = 0.207337$ Å) was used at DESY beamline P02.1. Instrument calibration was performed using LaB_6 (660c NIST standard). Diffraction data were collected using the Varex XRD 4343CT (150×150 µm2 pixel size, 2880 x 2880 pixel area, CsI scintillator directly deposited on amorphous Si photodiodes) and azimuthally integrated using the DAWN software. Data were plotted using Python and analysed with the FullProf software package.

5 Fundamental Electrochemical Performance of Cobalt Selenide for Rechargeable Aluminium Batteries

In any complex investigation, whether solving a mystery or unravelling the behaviour of a novel material, progress depends not only on the tools and evidence available but on the ability to interpret and connect findings. Initial observations may be misleading, masking the true nature of a system. This principle is particularly relevant to next-generation energy storage materials, where apparent performance may stem from parasitic reactions rather than the intended charge storage mechanism.

To assess the viability of CoSe as a cathode material for RABs, it is essential to understand its functional behaviour, the factors influencing its performance, and its degradation pathways. As discussed in Section 3.3.5, some cobalt selenides (CoSe and $CoSe_2$) have emerged as promising candidates for RABs, yet their charge storage mechanisms and stability in ionic liquid electrolytes remain insufficiently understood.

In this chapter the characterisation of CoSe is presented, and is structured as follows:

- Section 5.1: Physicochemical and structural characterisation of pristine CoSe.
- Section 5.2: Electrochemical evaluation and binder selection for CoSe cathodes.
- Section 5.3: Elucidating the reaction mechanisms and degradation pathways of CoSe in RABs.

5.1 Physicochemical and Structural Characterisation of Pristine CoSe

As established in Section 4.2, CoSe was synthesized via high-temperature selenisation of the ZIF-67 template. This process is expected to result in the carbonisation of the organic linkers, forming a carbonaceous shell around the CoSe particles.

5.1.1 Thermal Analysis of Carbon Content

To evaluate the presence and nature of the carbon shell, TGA and Raman spectroscopy were performed. The TGA results are presented in Figure 5.1.

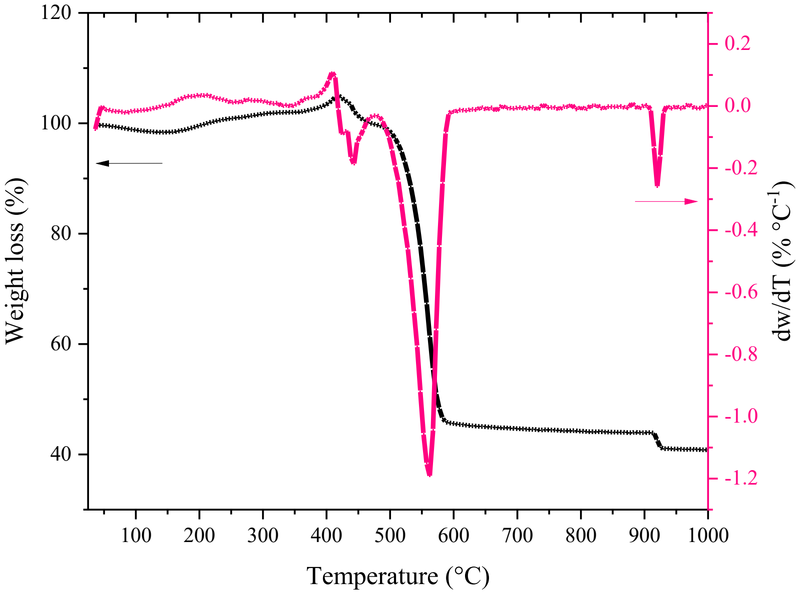

Figure 5.1 Thermal characterisation of the pristine CoSe: TGA (black) and DTGA (pink) curves of CoSe in air.

The thermogram in air reveals several distinct thermal events:

- Below 120°C, a minor weight loss (5 wt.%) is observed, attributed to the evaporation of absorbed water. This low value is consistent with the high-temperature synthesis, which minimizes residual moisture.
- Around 400°C, a slight mass gain is recorded, likely due to oxygen uptake and partial surface oxidation of CoSe.
- Between 480°C and 580°C, a significant mass loss occurs, with the DTGA peak at 560°C. The residual mass stabilises at 45.56 wt.%. This event corresponds to the combustion of the carbonaceous matrix derived from the ZIF-67 precursor forming CO and CO_2.
- A final decomposition event is observed around 900°C, with the DTGA peak at 921°C. This is attributed to the breakdown of CoSe and volatilisation of its oxidation products, including Co_3O_4, SeO_2.

The results confirm the presence of a carbon shell surrounding the active phase and its progressive oxidation between 400 and 900°C. The thermal behaviour reflects two sequential processes. (i) Combustion of the carbon matrix: This step involves the degradation of carbon originating from the MOF template. This interpretation is supported by a similar decomposition profile reported for ZIF-67/graphene oxide composites [91]. However, since said study was conducted under non-oxidizing conditions, the reported decomposition gases are different from those expected in an air atmosphere. (ii) Thermal decomposition and oxidation of the CoSe active phase: The final mass loss corresponds to the oxidation and volatilisation of CoSe, consistent with literature on $CoSe_2$/carbon fibres composites [92], which identifies, Co_3O_4 as the final stable product, while SeO_2 is lost as volatile.

It is important to note that the mass loss between 480°C–580°C results from overlapping processes: carbon combustion (mass loss), CoSe oxidation (mass gain), and SeO_2 volatilisation (mass loss). Due to this complexity, the carbon content cannot be directly quantified from this step alone. Consequently, electrochemical performance metrics such as current density are reported with consideration of the carbon shell's contribution.

5.1.2 Structural Properties and Composition

Raman spectroscopy is used to further investigate the structural features of the carbon matrix and the CoSe phase. The spectrum, shown in Figure 5.2, displays three key features.

The spectrum shows two broad peaks characteristic of carbon materials. The D band, at approximately 1360 cm^{-1}, corresponds to the breathing modes of sp2 carbon rings. It indicates disordered or amorphous carbon. The G band, at 1590 cm^{-1}, is attributed to the in-plane vibrational mode of sp2 hybridized carbon atoms, represents graphitic domains. The intensity ratio of these two bands, I_D/I_G, provides a quantitative measure of the degree of graphitisation and structural disorder. The calculated I_D/I_G ratio suggests a moderately ordered carbon matrix with limited defects.

In addition to the carbon features, a sharp peak at 675 cm^{-1} is assigned to C–Se bonding, consistent with literature reports on chemically bonded CoSe–carbon composites [93].

This chemical interaction is believed to enhance electrical connectivity and mitigate volume changes during cycling.

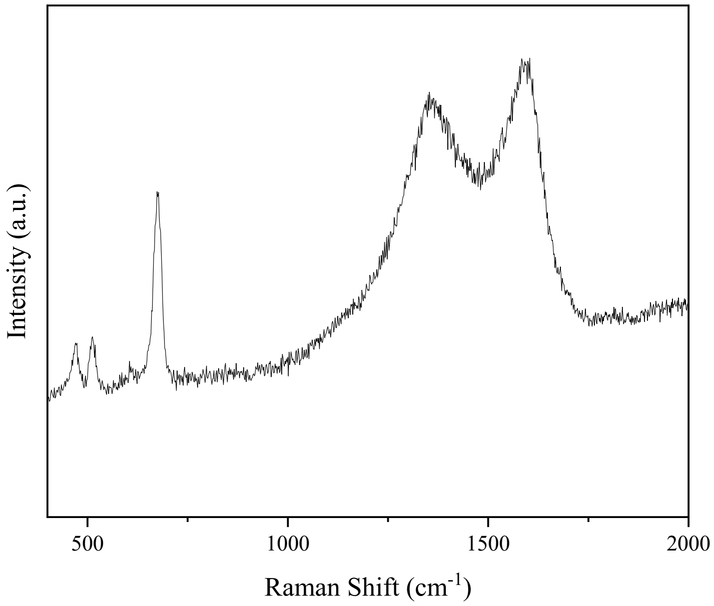

Figure 5.2 Structural characterisation of the pristine CoSe: Raman spectra of CoSe

Additional bands at 468 and 507 cm^{-1} are attributed to Co-Se vibrations, further confirming the formation of the CoSe phase. These bands were also reported in literature in studies of $CoSe_2$/C composite [94]. Minor shifts from literature values are attributed to differences in stoichiometry and morphology.

Together with TGA, the Raman results confirm the successful synthesis of a CoSe@C composite, with a chemically integrated carbon shell.

5.1.3 Crystalline Structure

XRD is used to determine the crystalline structure and phase purity of the material. The diffraction pattern, shown in Figure 5.3, reveals that the major diffraction peaks are indexed to a hexagonal phase of CoSe (space group $P6_3/mmc$). This result is consistent with the findings reported in literature [52], confirming the successful synthesis of the material. The Rietveld refinement yielded lattice parameters of a = b = 3.6121 Å and c = 5.2832 Å, where Co form the metallic sublattice and Se occupies the interstitial sites.

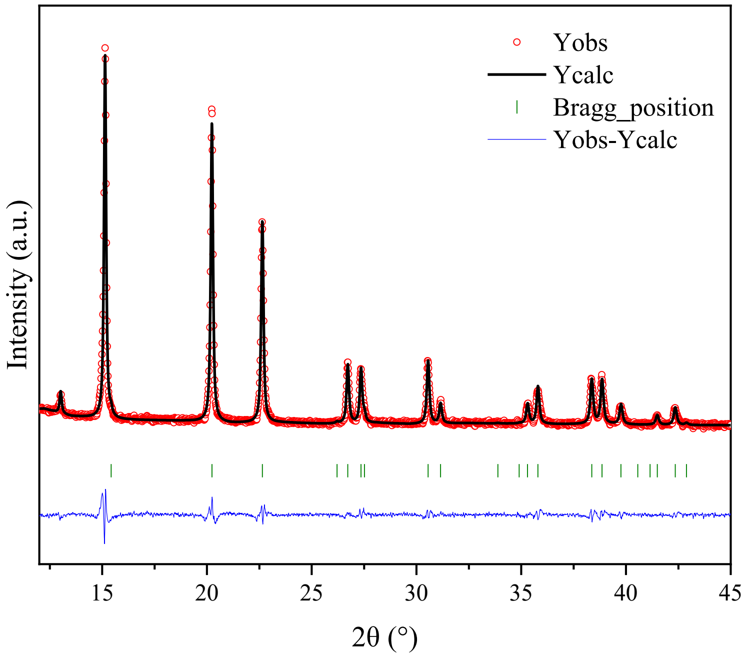

Figure 5.3 Characterisation of the crystalline structure: X-ray diffraction pattern of CoSe

Quantitative phase analysis estimated the composition as 99.81 ± 0.01% CoSe and 0.19 ± 0.01% $CoSe_2$. Given the proximity to the detection limit and negligible impact on refinement quality ($\chi^2 = 3.46$ with vs. 3.45 without), the presence of $CoSe_2$ in the pristine sample is considered minimal. However, its increased presence after electrochemical cycling suggests electrolyte-induced formation, which is further explored in later chapters.

5.1.4 Electronic Structure

The XAS is performed to probe the oxidation states and local environments of Co and Se in the pristine material. The results are shown in Figure 5.4.

The XAS spectrum at the Co K-edge (Figure 5.4 a) shows a progressive shift in edge energy across the reference compounds: metallic Co < CoSe < CoO < Co_3O_4. This trend reflects increasing oxidation states, with metallic Co at 0, CoO at +2, and Co_3O_4 containing both +2 and +3 oxidation states. The intermediate position of the CoSe edge between metallic Co and CoO supports the assignment of Co^{2+} as the dominant oxidation state in CoSe. This observation is consistent with the oxidation state of Co in CoSe reported previously in literature [93].

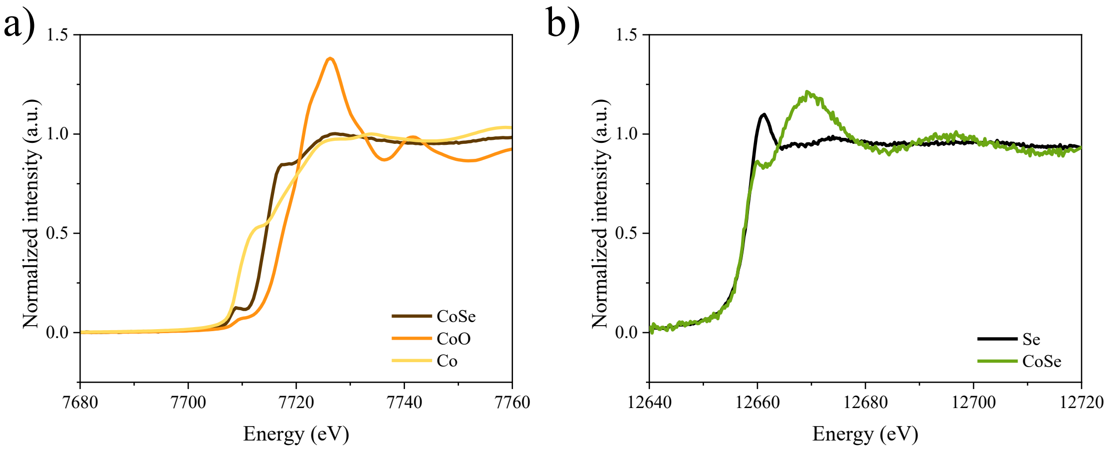

Figure 5.4 Characterisation of the electronic structure: XAS spectra of CoSe a) Co K-edge, b) Se K-edge

The XAS spectrum at the Co K-edge (Figure 5.4 b) shows a different behaviour. The edge position closely matches that of elemental Se (0), this minimal shift is expected, as literature reports that the K-edge position for Se compounds varies within a narrow range [95]. However, subtle differences are observed in the white line feature (the prominent peak at the edge). The white line of Se (0) reference, located at approximately 12669 eV, has a slightly higher intensity compared to that for the CoSe sample (12660 eV). The intensity and slight shift of the white lines suggest a reduced oxidation state in CoSe compared to elemental Se, consistent with literature trends [96].

These findings confirm the mixed-valence nature of the CoSe compound and its covalent bonding environment, where Co adopts a (+2) oxidation state, stabilized by the Se^{2-} anion.

5.1.5 Summary and Remarks on the Physicochemical and Structural Characterisation of Pristine CoSe

The combined results from TGA, Raman spectroscopy, XRD, and XAS provide a comprehensive understanding of the pristine CoSe material:

TGA and Raman confirmed the presence of a carbon shell derived from the MOF precursor. XRD verified the formation of the desired hexagonal CoSe phase with minimal secondary phase. XAS revealed a Co oxidation of +2 and a Se state of -2, consistent with covalent Co–Se bonding.

These findings validate the successful synthesis of a structurally and electronically well-defined CoSe@C composite, setting a robust foundation for subsequent electrochemical investigations.

5.2 Electrochemical Evaluation and Binder Selection for CoSe Cathodes

In the context of RABs, several principles from other electrochemical systems apply, most notably, the importance of continuous electronic conductivity and a stable electrode-electrolyte interface. These characteristics are directly influenced by the distribution of the active material, conductive additives, and the current collector, which in turn depends on the binder used. Therefore, binder selection is a critical factor in electrode performance and stability.

To enable accurate characterisation of the energy storage mechanism of CoSe, it is essential to minimize parasitic effects introduced by suboptimal binders. This section presents a comparative study of three binders with distinct chemical properties: PAN, carr, and CMC.

5.2.1 Microstructural Characterisation of Electrodes

Surface and cross-sectional SEM images of CoSe electrodes fabricated with different binders are shown in Figure 5.5. Electrodes prepared with PAN exhibit superior penetration into the C Paper substrate, resulting in a more uniform distribution of the active material. This uniformity preserves the morphology of the CoSe particles and enhances the overall surface area, which is expected to reduce diffusion limitations and improve electrochemical performance.

In contrast, electrodes fabricated with carr and CMC show less homogeneous coverage and poorer integration with the current collector. The way these morphological differences correlate with the electrochemical results will be approached in Section 5.2.3.

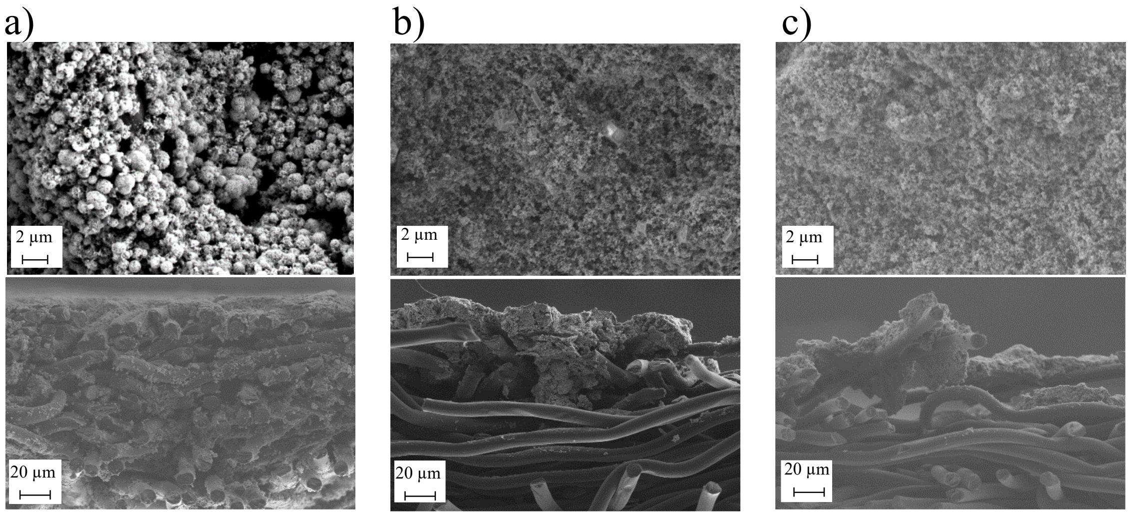

Figure 5.5 Microstructural characterisation: SEM images of CoSe electrodes fabricated with different binders (top: superficial view, bottom: cross section): a) PAN b) carr and c) CMC

5.2.2 Effect of Binder on Electrolyte Stability

As a critical component of the electrode, the binder not only ensures the mechanical integrity of the active material and conductive additives but are also guarantees intimate contact with the electrolyte, potentially influencing its electrochemical stability window. This is a particularly relevant consideration for chloroaluminate ionic-liquid-based electrolytes, which already possess a narrow stability window.

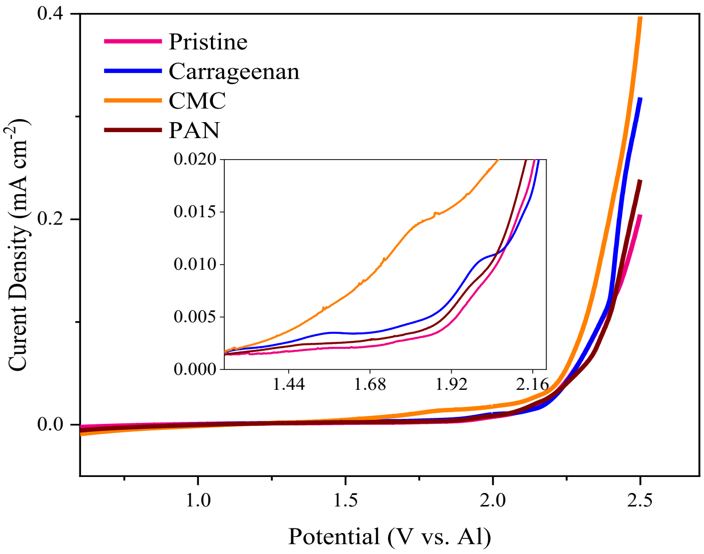

Figure 5.6 Effect of binder on electrolyte stability: LSV of cells fabricated with inert C paper and electrolytes soaked with different binders.

To assess this effect, each binder was soaked in electrolyte, and the resulting solutions are tested via LSV measurements in cells fabricated with inert C Paper cathode and Al foil anode (Figure 5.6).

While all binders exhibited some impact on the electrolyte's stability, CMC causes the most pronounced negative effect in the electrochemical stability window, evidenced by an earlier onset of oxidation current. Carr also showed a measurable negative effect, whereas PAN had the least influence. These results highlight the importance of binder–electrolyte compatibility in maintaining system-level stability.

5.2.3 Electrochemical Characterisation of Electrodes

The electrochemical performance of CoSe cathodes fabricated with carr, PAN and CMC was evaluated using GCPL cycling, as shown in Figure 5.7.

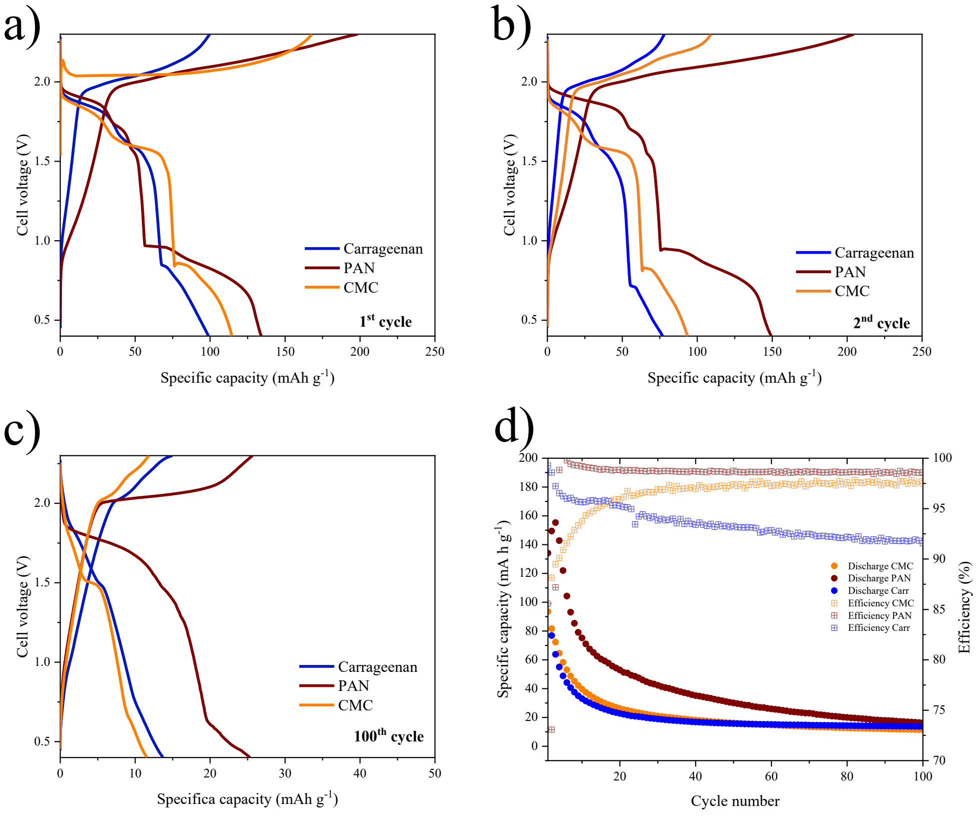

Figure 5.7 Electrochemical characterisation: GCPL of CoSe electrodes fabricated with different binders a) 1st cycle, b)2nd cycle, c)100th cycle, d) capacity vs cycle number

All electrodes exhibited capacity fading over 100 cycles, this process is a distinguishing feature of CoSe electrodes in literature [52], [53], [54]. Moreover, the PAN-based electrode consistently demonstrates higher initial capacity and slower degradation.

Differential capacity plots (dQ/dV), presented in Figure 5.8, provide further insight into the underlying electrochemical processes. In the first cycle, all electrodes display a prominent irreversible cathodic peak near 1 V, attributed to the initial reduction of CoSe. The peak position varies slightly depending on the binder: 0.95 V (PAN), 0.88 V (CMC), and 0.83 V (carr), with PAN showing the highest intensity. This supports the SEM findings, indicating better utilisation of the active material due to improved active material distribution.

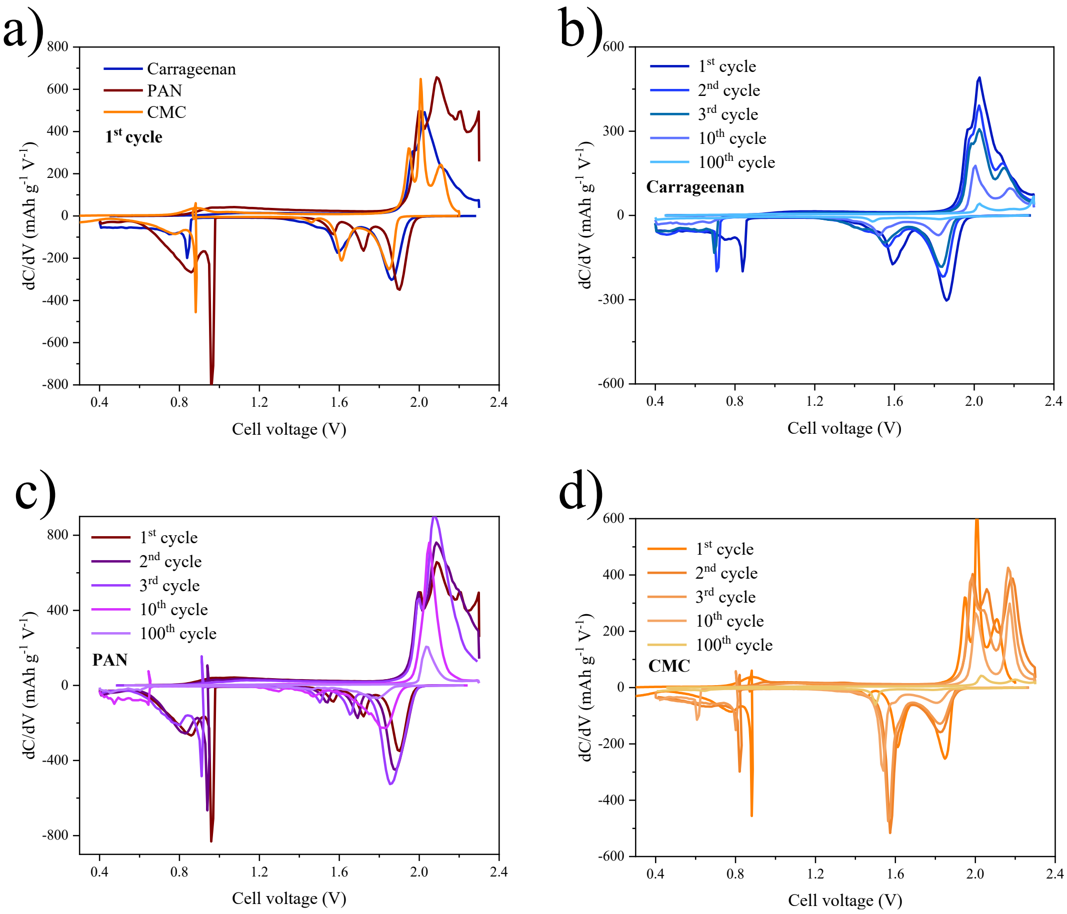

Figure 5.8 Electrochemical characterisation: differential capacity (dQ/dV) curves of CoSe cathodes fabricated with different binders a) 1st cycle of all binders b) carr c) PAN d) CMC

Over 100 cycles, all electrodes show diminished peak intensity and a progressive shift of cathodic peaks to lower voltages, indicating increased overpotential and electrochemical polarisation. This shift reflects kinetic hindrance at the electrode–electrolyte interface and contributes to capacity fade. Despite this, PAN-based electrodes retain the most defined and intense peaks, in agreement with a slight higher capacity retention over the first 70 cycles.

5.2.4 Remarks on Electrochemical Evaluation and Binder Selection for CoSe Cathodes

The comparative analysis of binder performance reveal that PAN provides the most uniform distribution of the active material to the C Paper current collector. This superior morphology directly correlates with improved electrochemical behaviour. PAN also exhibits the least detrimental effect on the electrochemical stability window of the chloroaluminate IL-based electrolyte.

Electrochemical testing confirm that PAN-based electrodes deliver the highest initial capacity and the slowest degradation rate over 100 cycles. Differential capacity analysis further supported these findings, showing a more intense irreversible cathodic peak in the first cycle, indicative of more complete electrochemical activation of the CoSe material.

Based on these results, PAN is selected as the optimal binder for all subsequent electrochemical studies.

5.3 Elucidating the Reaction Mechanisms and Degradation Pathways of CoSe in RABs

The electrochemical behaviour of CoSe is investigated using CV, GCPL, and mechanistic analysis. The initial degradation of CoSe in contact with the electrolyte is assessed *by ex situ* characterisation of electrodes soaked in the electrolyte and the electrochemical characterisation of the resulting electrolyte These techniques are applied to understand the redox processes, identify the active charge carriers, and evaluate degradation pathways during cycling.

5.3.1 Initial Degradation

The main challenges that RABs research face are related to the corrosivity of the electrolyte, which hinders the selection of active and passive components of the cell, the harsh environment in RABs suggests that an initial degradation may initiate even before electrochemical cycling.

To investigate the initial degradation, CoSe electrodes were soaked in pristine electrolyte. Visual inspection revealed a colour change in the electrolyte, from translucent to yellowish, indicating chemical interaction. Subsequent ICP-OES analysis confirms the presence of both cobalt and selenium in the soaked electrolyte, providing direct evidence that CoSe partially dissolves upon contact with the electrolyte, even prior to cycling.

To further characterize the electrochemical activity of these dissolved species, the soaked electrolyte was used to assemble a two electrode cell with an inert C Paper cathode and Al anode and subjected to LSV. The results are compared with the LSV of a pristine electrolyte in the same cell structure (Cpaper //Al) and presented in Figure 5.9

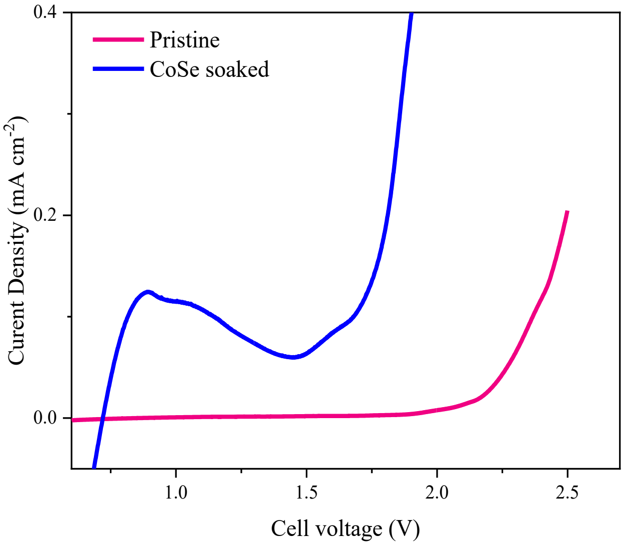

Figure 5.9 Effect of dissolved species in electrochemical stability window: LSV of Cpaper//Al cells with electrolyte soaked with CoSe and pristine electrolyte

The data provide definitive evidence that the dissolved species detected by ICP-OES analysis are redox-active. An oxidation peak is observed at approximately 0.9 V and the onset of a broader oxidation current begins around 1.7 V, confirming that the species undergo oxidation that could interfere with the cell's intended electrochemistry.

To evaluate structural changes caused by the initial degradation on the CoSe structure, the soaked CoSe electrode is analysed via XRD. The resulting diffractogram, shown in Figure 5.10, reveals significant changes compared to the pristine sample.

The disappearance of the reflection at 13.08°, corresponding to the (100) plane, indicates anisotropic dissolution, disrupting the in-plane registry of the crystal. A general decrease in reflection intensity suggests partial dissolution of the material. Finally, a shift toward higher 2θ angles implies lattice shrinkage and defect formation, likely due to the loss of Co and Se atoms, as supported by ICP-OES data.

Additionally, XRD measurements revealed Co_3Se_4 reflections. The role of this species in the electrochemical mechanism is addressed in Section 6.1.2 during the *operando* characterisation.

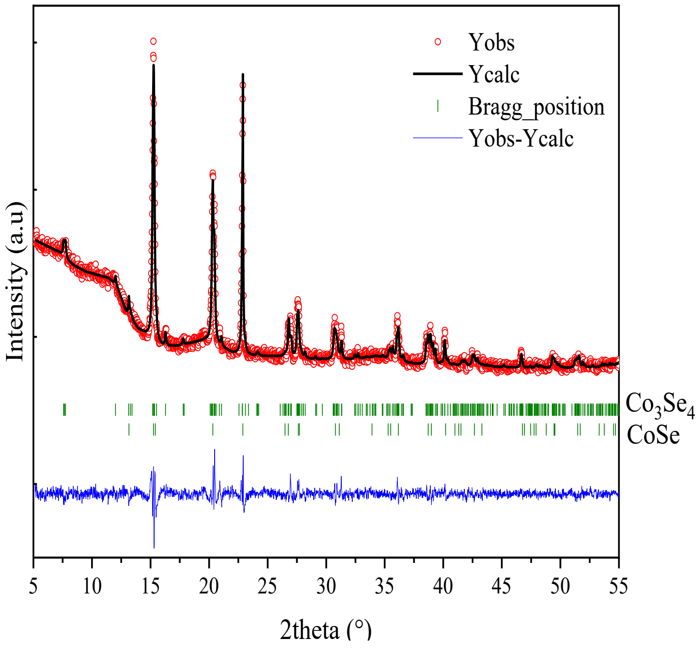

Figure 5.10 Effect of initial dissolution on crystalline structure: X-ray diffractogram of CoSe soaked in electrolyte

Furthermore, the soaked electrode was analysed using Raman spectroscopy. The spectrum, shown in Figure 5.11, reveals significant degradation as the C–Se peak at 675 cm^{-1} and Co–Se bands at 468 and 507 cm^{-1} of the pristine sample (Figure 5.2) are no longer visible, indicating substantial dissolution of the active material. The remaining spectrum shows only the D and G bands of the carbon matrix. The I_D/I_G ratio of 0.84, like the pristine value of 0.8, suggests that the carbon layer remains largely intact after soaking.

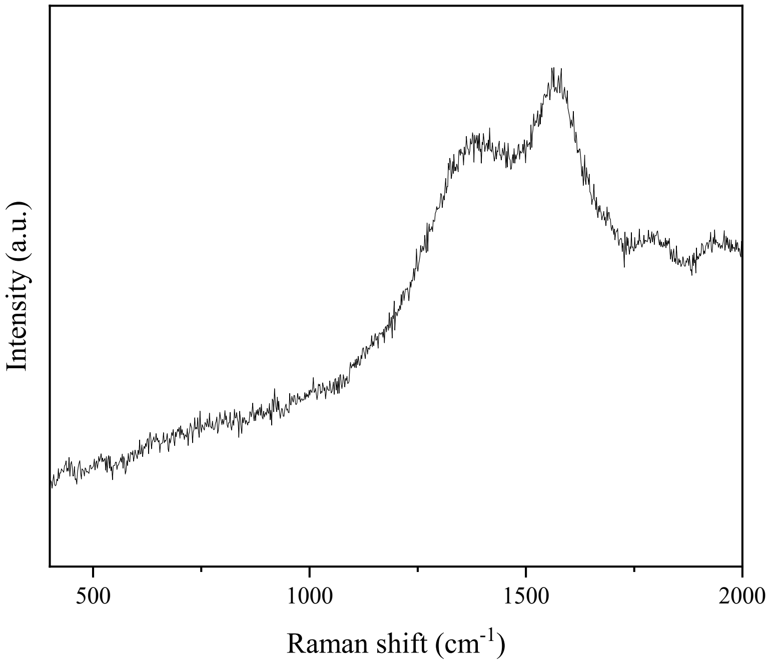

Figure 5.11 Effect of initial dissolution on chemical structure: Raman spectra of CoSe soaked in electrolyte

5.3.2 Redox Behaviour and Charge Carrier Mechanism

The electrochemical characterisation of CoSe cathodes is presented in Figure 5.12. CV curves (Figure 5.12 a) reveal two distinct redox couples during the first cycle: anodic peaks at approximately 1.03 V and 2.00 V, and corresponding cathodic peaks at 0.57 V and 1.80 V. These peaks indicate the presence of at least two electrochemical processes contributing to charge storage.

As cycling progresses, the redox peaks shift: by the 10th cycle, the anodic peak moves to 1.01 V and the cathodic peak to 0.66 V. This shift reflects a reduction in overpotential, suggesting improved kinetics and reversibility. The narrowing of the voltage gap between anodic and cathodic peaks implies that the electrode undergoes a gradual activation process, likely influenced by the progressive dissolution of the native oxide layer on the Al foil anode. Initially, this passive layer hinders Al plating and stripping [97], but it is gradually removed by the chloroaluminate electrolyte. As the interfacial resistance decreases, charge transfer becomes more efficient, contributing to the observed peak evolution.

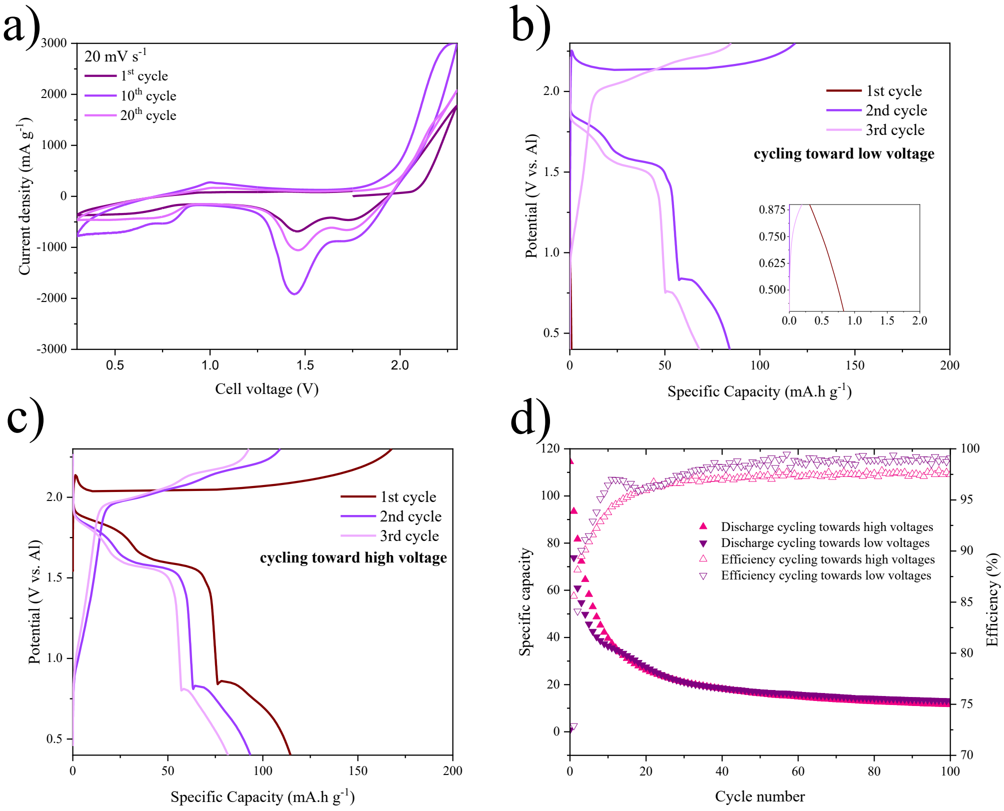

Figure 5.12 Electrochemical characterisation of CoSe electrodes (fabricated with carr): a) CV curves, b) GCPL curves starting from OCV toward lower potentials, c) GCPL curves starting from OCV toward higher potentials, d) efficiency and specific capacity of cell starting from OCV toward higher potentials

To determine the nature of the charge carrier, GCPL is performed (CoSe//Al) cells, cycling is initiated toward oxidation (higher voltages) and reduction (lower voltages), with identical CoSe cathodes (fabricated with carr). Although PAN was identified as the binder with the least detrimental effect on the electrolyte and the best distribution of active material on the current collector, the direct comparison of the galvanostatic cycling initiating from both a discharge and charge could not be conducted using PAN as a binder due to material constraints. Instead, carr-based electrodes were used for this comparison, as its influence is primarily kinetic, and the fundamental electrochemical behaviour of

CoSe remains representative. Therefore, the results presented here for the CMC-based electrodes are considered representative of the electrochemical behaviour of the CoSe cathode, with the difference of a reduction in the overall performance due to the binder limitation on cell kinetics.

In Figure 5.12 b), cycling begins from the open-circuit voltage (OCV, 1.55 V) toward lower voltages. The initial discharge capacity is negligible (0.4 mAh g^{-1}), which could be attributed to double-layer formation, while the subsequent charge reaches approximately 54 mAh g^{-1}. This pronounced asymmetry indicates that the CoSe electrode does not undergo significant reduction (cation insertion) during the initial discharge, and that charge storage becomes active only after an initial oxidation step.

In contrast, Figure 5.12 c), shows that when cycling starts from the OCV (1.73 V) toward higher potentials, both charge and discharge capacities in the first cycle are substantial and comparable (154 mAh g^{-1} and 114 mAh g^{-1}, respectively), This behaviour suggests that, once the electrode has been oxidized, reversible ion insertion and extraction can occur.

Taken together, these results imply that the CoSe electrode requires an activation process via oxidation before reversible electrochemical reactions can proceed. Such behaviour is consistent with an anion $AlCl_4^-$ insertion mechanism, like that observed in graphite electrodes [16], [98], [99], [100], [101]. If Al^{3+} were the active species, one would expect measurable discharge capacity when cycling begins from lower potentials. The absence of such capacity indicates that cation insertion is unlikely under these conditions.

Moreover, as calculated in Section 2.3.2 the theoretical specific capacity of CoSe, assuming a three-electron redox process involving Al^{3+}, is approximately 409 mAh g^{-1}. However, the experimentally observed capacity with PAN-based electrodes (the highest observed capacity) is significantly lower, below 200 mAh g^{-1} (Figure 5.7). This discrepancy aligns more closely with the theoretical capacity for a single-electron transfer mechanism involving $AlCl_4^-$, which is 194 mAh g^{-1}. The proximity of experimental values to this theoretical limit further supports a single electron redox mechanism, therefore $AlCl_4^-$, not Al^{3+}, is responsible for charge storage in this system.

Figure 5.12 d) shows the evolution of charge/discharge capacity and coulombic efficiency over the first 50 cycles. A notably low efficiency is observed in the initial cycles for both cells, which gradually improve with continued cycling. This behaviour is commonly attributed to the formation of a cathode–electrolyte interphase (CEI), a phenomenon well-documented in graphitic cathodes [101], [102], [103]. While CEI formation in selenide-based cathodes is less explored, the presence of a carbonaceous matrix in the synthesized CoSe suggests that similar interfacial processes may occur.

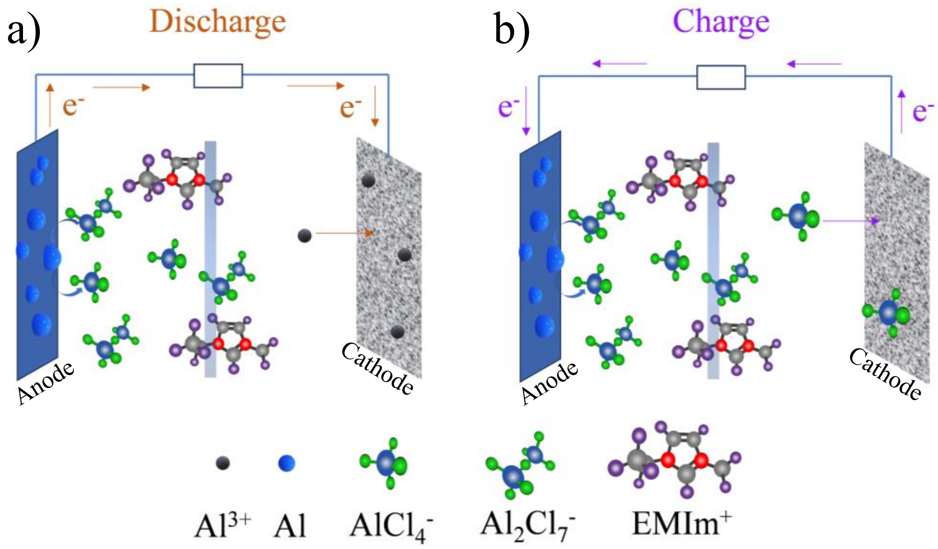

Figure 5.13 Conceptual comparison of ion insertion mechanisms in cathodes for RABs: a) insertion of Al^{3+} occurring during discharge, b) insertion of $AlCl_4^-$ occurring during charge

Figure 5.13 illustrates conceptually how the electrochemical mechanism depends on whether the CoSe electrode accommodates cationic or anionic aluminium species. The schematic is intended as a qualitative comparison to highlight the direction of ion movement rather than depict a complete mechanistic model.

In the case of a cation-insertion mechanism (Figure 5.13 a), earlier studies have proposed that electrochemical reduction of CoSe proceeds via the insertion of aluminium species derived from the Lewis acidic electrolyte. However, free Al^{3+} ions do not exist in such media; instead, aluminium is present as chloroaluminate complexes ($Al_2Cl_7^-$ and $AlCl_4^-$) in equilibrium. Therefore, Al^{3+} insertion would involve local decomplexation steps at the cathode, where $AlCl_4^-$ provides coordinated chloride to form Al–Se bonds, while chloride released at the cathode participates in regenerating Al_2Cl_7 at the anode.

In contrast, under an anion-insertion mechanism (Figure 5.13 b), oxidation of the CoSe electrode is charge-balanced by the insertion of complex anions such as $AlCl_4^-$. At the same time, oxidation at the aluminium anode produces Al^{3+}, which immediately complexes with available chloride (from $AlCl_4^-$/ $Al_2Cl_7^-$ equilibrium) to maintain charge balance.

Thus, while Figure 5.13 is schematic, it emphasizes that (i) there are no free chloride or Al^{3+} ions in solution, (ii) all charge transport occurs through coordinated chloroaluminate species, and (iii) the observed electrochemical asymmetry, where capacity emerges only after an initial oxidation, aligns with an anion-insertion process. This interpretation challenges previous reports on CoSe and $CoSe_2$, such as those by W. Xing et al. [52], Cai et al. [53] and Yao et al. [54], which proposed Al^{3+} insertion or conversion mechanisms.

5.3.3 High Voltages Irreversibility

The electrochemical evaluation of CoSe cathodes in this study was conducted at relatively high current densities (1 $A \cdot g^{-1}$), consistent with conditions used in previous literature [52], [53], [54]. While some studies have reported measurements at similar or even higher current densities, there is a noticeable absence of data at lower current densities. This omission may reflect a strategic choice to suppress parasitic reactions and obtain clearer electrochemical signals. However, it also suggests that the behaviour of cobalt selenides under low-current conditions remains underexplored.

To investigate this gap, Figure 5.14 presents the GCPL profiles of two identical cells cycled at a low current density of 25 mAg^{-1}. Both cells exhibit a prolonged, flat voltage plateau near 2 V, referred to as an "infinite plateau". This behaviour is characteristic of a dominant parasitic side reaction that overshadows the intended electrochemical processes. The lack of meaningful capacity under these conditions may explain why previous studies did not report data at low current densities. However, rather than avoiding this regime, our study aims to understand the origin and nature of these parasitic processes, which could be critical for improving the long-term stability and performance of CoSe-based cathodes.

At low current densities, the extended time per cycle allows parasitic reactions to proceed more extensively, making them dominant over the intended electrochemical processes. This observation explains the low initial coulombic efficiency and supports the hypothesis that the early stages of cycling are dominated by dissolution of active species rather than by the formation of a CEI. Although these reactions are less pronounced at higher current densities, they still influence the initial capacity and reversibility.

This raises an important consideration, what we interpret as "true performance" may depend on the conditions under which the system is evaluated. Previous studies have largely avoided low current regimes, possibly due to the lack of meaningful capacity and the dominance of side reactions. However, this omission leaves a gap in understanding the full electrochemical behaviour of CoSe cathodes. Our results suggest that exploring this regime is essential to uncover the underlying degradation mechanisms and interfacial processes that are otherwise masked at higher rates.

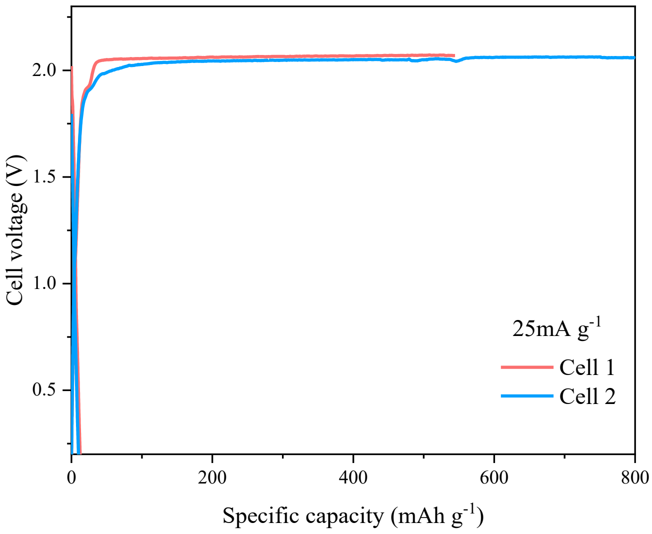

Figure 5.14 High voltage irreversibility: GCPL profiles at 25 mA g^{-1}of identical cells assembled with CoSe cathodes

To further investigate the nature of these high-voltage processes CA is performed on three identical cells, with slightly different active material masses (see Table 5.1). The capacity of the cells shows slight variations, likely influenced by differences in the mass of active material, as well as by its microstructure. These factors could affect the amount of CoSe available to participate in the electrochemical process occurring at 2 V.

The current–time profiles, presented in Figure 5.15, deviate from classical electrochemical behaviour. Instead of a monotonic decay typical of double-layer charging or diffusion-limited processes, the curves exhibit an initial drop followed by wave-like oscillations before stabilizing. This non-Cottrellian response suggests the presence of complex phenomena, likely involving parasitic reactions or partial dissolution of the active material [28].

Table 5.1 Details of cells 1-3

Cell	Specific capacity (mAh g^{-1})	Capacity (mAh)	Initial response (mA)	Mass of active material (mg)
1	294.578	0.401	4.001	1.36
2	211.114	0.328	1.002	1.55
3	311.896	0.374	0.974	1.20

While dissolution of active material is a plausible contributor, classical dissolution typically manifests as a gradual current decrease. The observed oscillations may instead reflect a staged or spatially heterogeneous dissolution process, potentially influenced by the microstructure of the electrode [104]. For instance, localized regions of CoSe may dissolve sequentially or intermittently, driven by variations in surface accessibility, crystallographic orientation, or binder distribution. This could result in transient increases in current as new reactive sites become exposed, followed by decreases as those sites are consumed.

Previous studies have reported cobalt dissolution from Co_9S_8 electrodes in RABs, as evidenced by post-cycling analysis following separator removal, in their work, significant cobalt dissolution into the electrolyte during cycling was confirmed by ICP-OES, indicating severe material degradation [54]. However, this works did not investigate the dissolution mechanism in detail, nor did they employ chronoamperometric techniques to resolve its time-dependent behaviour. Instead, strategies such as MXene-based surface engineering were proposed to mitigate the issue.

These precedents reinforce the hypothesis that the observed current behaviour in CoSe electrodes reflects a dissolution-driven process. To assess the impact of this high-voltage process on the performance, and the contribution of the parasitic reaction to the initial capacity four electrochemical protocols were applied:

- **Cell 0 (Control):** No CA. GCPL at 1 A g^{-1} performed directly after assembly.
- **Cell 1:** CA at 2 V for 2 hours, followed by GCPL at 1 A g^{-1}.
- **Cell 2:** CA at 2 V for 2 hours, followed by replacing the electrolyte and separator with fresh, unused components before performing GCPL at 1 A g^{-1}.
- **Cell 3:** CA at 2 V for 2 hours, followed by replacing the electrolyte, separator, and Al foil with fresh, unused components before performing GCPL at 1 A g^{-1}.

Figure 5.15 compares the cycling behaviour of these cells. Cell 0 begins with the highest initial specific capacity (~140 mAh g^{-1}), compared to the theoretical 194 mAh g^{-1}, and suffers rapid degradation, stabilizing at only ~16 mAh g^{-1} by the 100th cycle. In contrast, Cell 3 starts with a much lower initial capacity (~11 mAh g^{-1}) but exhibits superior stability, reaching ~31 mAh g^{-1} after 100 cycles. This trade-off highlights the dual nature of the high-voltage process: while it contributes to initial capacity, it also initiates degradation pathways, most likely modifying the electrolyte composition, compromising long-term performance. The pre-treatment protocols, particularly the full replacement of cell components in Cell 3, appear to mitigate these effects, enabling a more stable and durable cycling behaviour despite its considerable capacity loss.

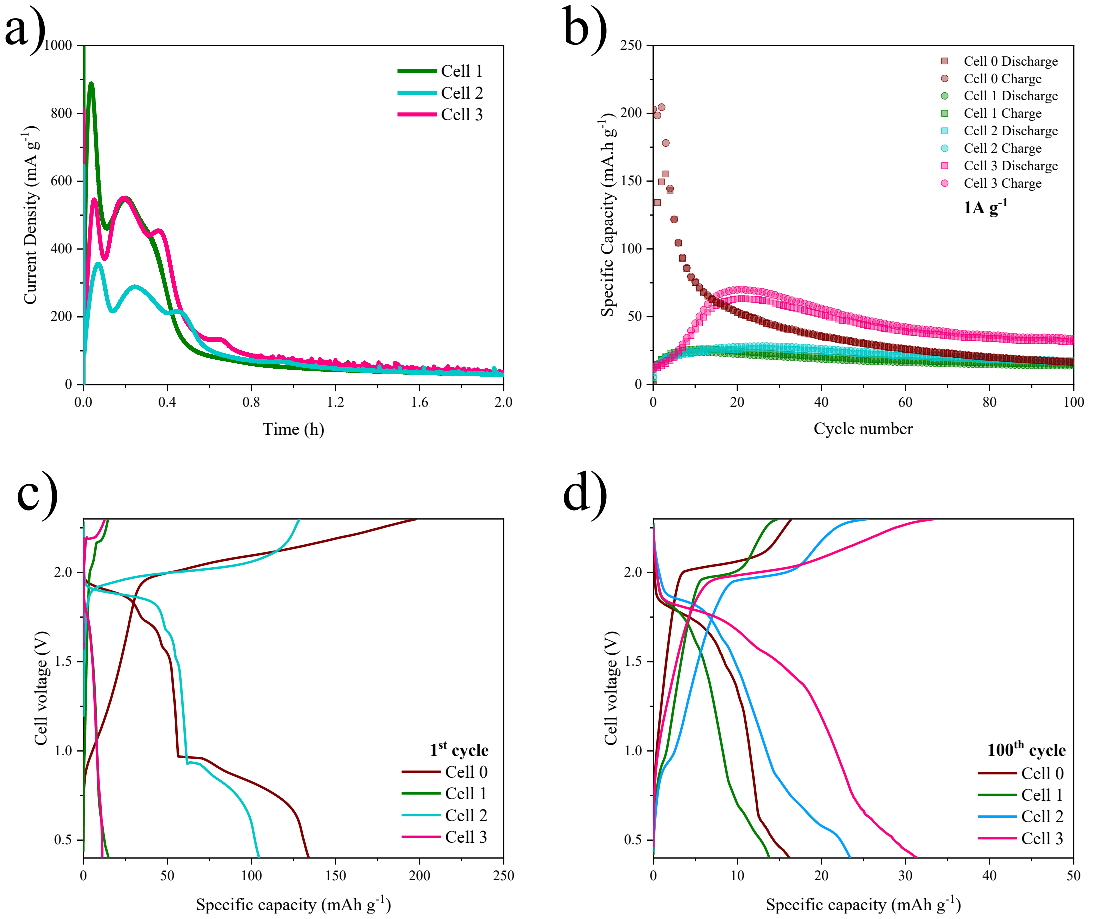

Figure 5.15 High voltages irreversibility. Electrochemical characterisation of cells subjected to CA pretreatment a) CA curves of cells at 2 V, b) capacity vs. cycle number, c) 1st cycle for all cells, d) 100th Cycle for all cells

To further dissect the electrochemical behaviour, differential capacity (dQ/dV) plots were generated for all four cells (Figure 5.16). These plots provide a high-resolution view of the redox processes and their evolution over cycling.

In the first cycle (Figure 5.16 a), Cells 1, 2, and 3 exhibit a simplified anodic profile compared to Cell 0. The multi-step anodic processes observed in Cell 0 are reduced to a single peak, indicating that the CA pre-treatment triggers parasitic reactions in advance, thereby altering the electrochemical environment of the cell.

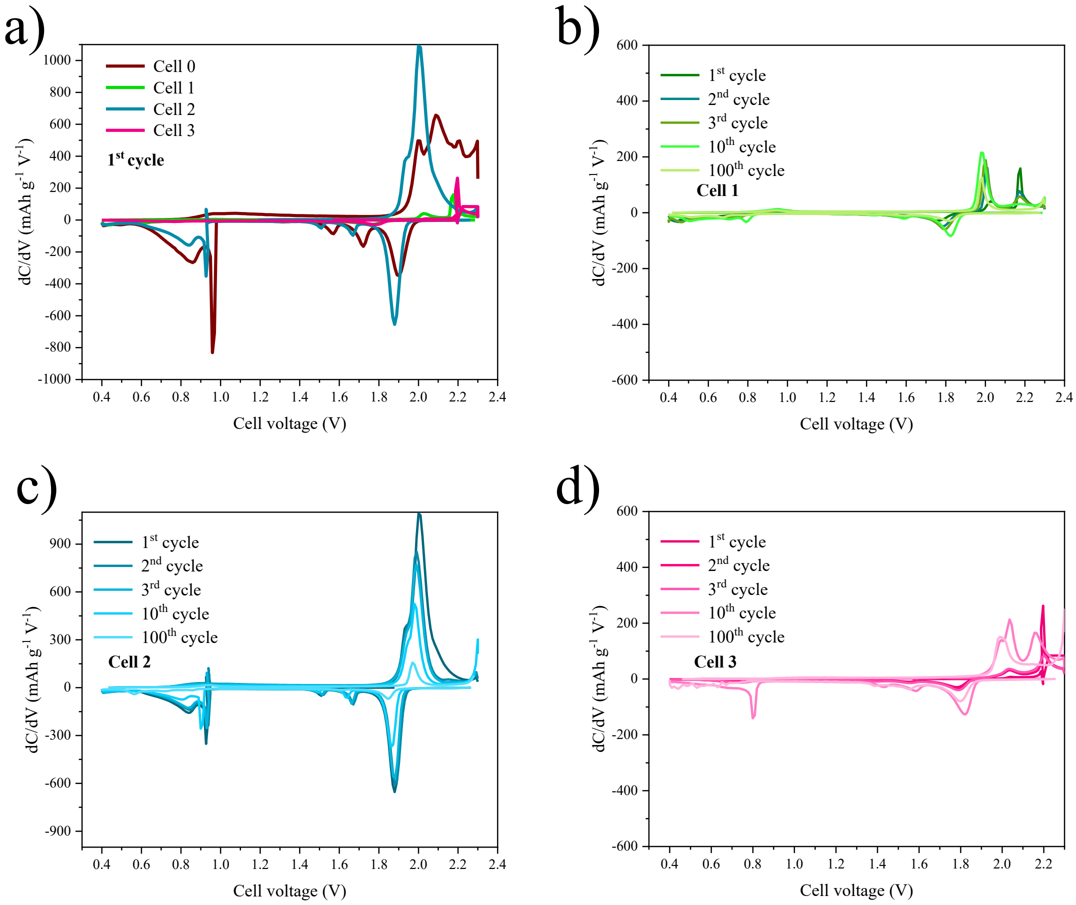

Figure 5.16 High voltages irreversibility. Differential capacity (dQ/dV) analysis of cells subjected to CA pretreatment a) 1st cycle for all cells, b) Cell 1, c) Cell 2, d) Cell 3

A key feature in the first-cycle dQ/dV plots is the irreversible cathodic peak near 1 V. This peak is present in Cells 0 and 2 but absent in Cells 1 and 3. Its presence is interpreted as the reduction of a species formed during the initial charge or CA step, likely a product of interactions between CoSe, the chloroaluminate electrolyte, and the Al anode. The contrasting behaviour of this peak in Cells 1 and 3 provides valuable mechanistic insight. In Cell 1, the absence of the peak is attributed to the depletion of active electrolyte species during CA, which hinders Al plating and stripping [15]. In Cell 3, the peak is initially absent due to the use of fresh components but appears after the 10th cycle. This delayed appearance suggests that the species responsible for the 1 V peak forms gradually, likely, as the native oxide layer on the Al anode is removed [105]. This delayed activation, combined with the gradual increase in capacity, indicates that Cell 3 undergoes a controlled activation process. Unlike Cell 0, where activation and degradation occur simultaneously, Cell 3 separates these processes, allowing the system to stabilize before full electrochemical activity is achieved. The eventual appearance of the 1.0 V peak marks the completion of this activation, correlating with the cell's superior long-term performance.

The evolution of the dQ/dV profiles for each cell can be summarized as follows:

- **Cell 0 (Control):** (Figure 5.8 c) immediate and intense activation, the high voltage processes evolve from multiple peaks in the first cycle into a single, high-intensity peak. The rapid activation is accompanied by the abrupt degradation and poor capacity retention.
- **Cell 1 (CA at 2 V-2 h):** (Figure 5.16 b) significantly lower peak intensity and a gradual reduction in the overpotential over cycling, indicating improved kinetics but limited capacity due to electrolyte degradation.
- **Cell 2 (CA at 2 V -2h, fresh electrolyte):** (Figure 5.16 c) similar to Cell 1 but with higher peak intensity, reflecting a more robust electrochemical process enabled by electrolyte replacement. This supports the belief that the irreversible process at 2.0 V consumes active species in the electrolyte.
- **Cell 3 (CA at 2 V -2h, fresh electrolyte and anode):** (Figure 5.16 d) slow, deliberate activation, rather than a rapid destructive one, highlights the cell's enhanced stability. This demonstrates that the irreversible process at 2.0 V not only consumes active species in the electrolyte but also affects the surface of the Al anode.

The irreversible capacity loss and distinct electrochemical features observed at high voltages suggest the presence of a parasitic side reaction. If left uncontrolled, this reaction leads to rapid degradation, as seen in the control cell. However, when managed through pretreatment and component replacement, it can serve as a beneficial activation step, as demonstrated by the performance of Cell 3.

Given the known instability of transition metal-based cathodes in chloroaluminate ionic liquid electrolytes, it is hypothesized that this dual-nature irreversibility is linked to the dissolution and migration of cobalt to the anode. The ability to control this initial process, either by suppressing it or by isolating it from long-term cycling, is an initial approach for achieving both high performance and extended cycle life in CoSe-based RABs.

5.3.3.1 Effect of high voltage irreversibility on the anode

To assess the impact of the activation process on the Al anode, foil samples are extracted after 2 h of CA at 2 V, washed with 1,2-difluorobenzene, and analysed via SEM-EDX. The results, shown in Figure 5.17, reveal the presence of chlorine, indicating residual electrolyte trapped in surface imperfections. However, no Co or Se was detected, an unexpected result given the improved performance observed with fresh Al foil.

The absence of observable deposits of Co or Se may be due to the washing step, which could have removed loosely bound species. Because of the corrosive nature of the electrolyte, analysing the foil without washing was not feasible, highlighting the limitations of SEM-EDX for detecting transient or soluble species.

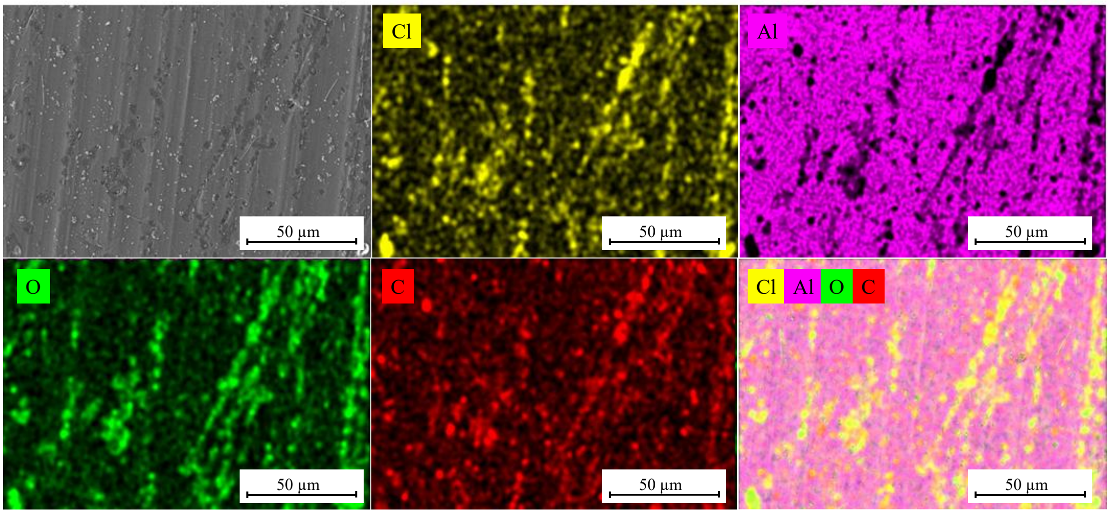

Figure 5.17 Effect of activation on the anode: SEM EDX of the Al foil after CA at 2 V for 2h, washed three times with fluorobenzene after disassembling the cell

Another technique proposed to investigate the influence of electrochemical treatment on Al anodes is EIS. It is performed on symmetric Al//Al cells. The cell labelled 'Pristine Al Foil' is assembled using untreated Al foils. The cell 'CA at 2 V for 2 h' uses both Al anodes extracted from CoSe//Al cells that underwent chronoamperometry at 2 V for 2 hours. To isolate the effect of the electrochemical treatment from that of the passivation layer on pristine Al, the cell 'Al Activation' is fabricated using Al anodes extracted from similarly treated cells, but with inert cathodes instead of CoSe (Cpaper//Al). The resulting Nyquist plots are presented in Figure 5.18.

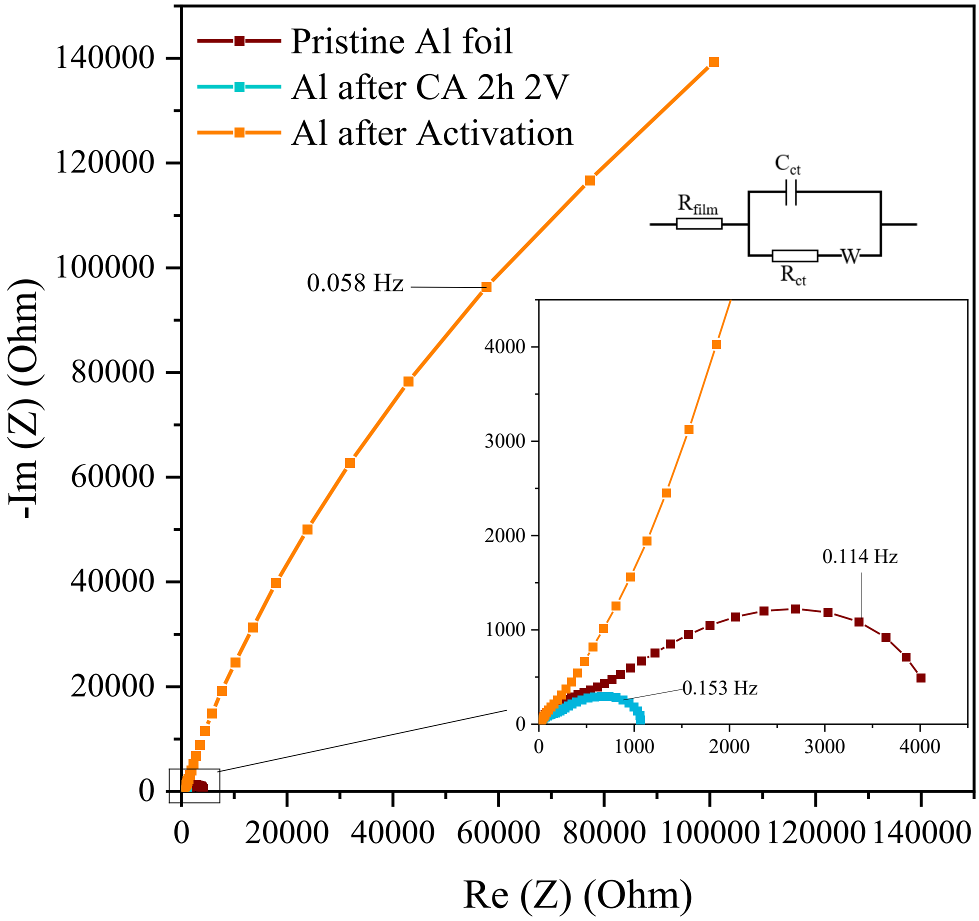

Figure 5.18 Effect of activation on the anode: PEIS graphs of symmetric Al foil cells, pristine and after pretreatment with CoSe and an inert cathode. From 30 mHz to 0.1 MHz

All cells exhibit similar high-frequency intercepts, confirming consistent electrolyte resistance. However, the foil treated without CoSe exhibits a diffusion-dominated response, lacking distinct semicircles. This implies a highly resistive and unstable surface, likely due to re-passivation as reported in literature [105].In contrast, the CoSe-pre-treated foil shows a substantial reduction in surface film resistance (R_{film}) and charge transfer resistance (R_{ct}) compared to the pristine foil. This suggests that the CA pre-treatment at

2 V for 2 h removes the native passivation layer and likely deposits Co or Se species that enhance interfacial conductivity and hinder the repasivation of the Al foil.

These results provide electrochemical evidence that the high voltage irreversibility alters the surface of the electrode, likely speeding up degradation processes, and agree with the improved performance observed in Cell 3 compared to Cell 0.

5.3.3.2 Effect of high voltage irreversibility on the electrolyte

The high voltage irreversible process likely affects the electrolyte by consuming active species and introducing redox-active degradation products. To evaluate this, a cell is assembled using electrolyte previously subjected to CA at 2 V for 2h, replacing the CoSe electrode with inert C Paper, and subjected to LSV.

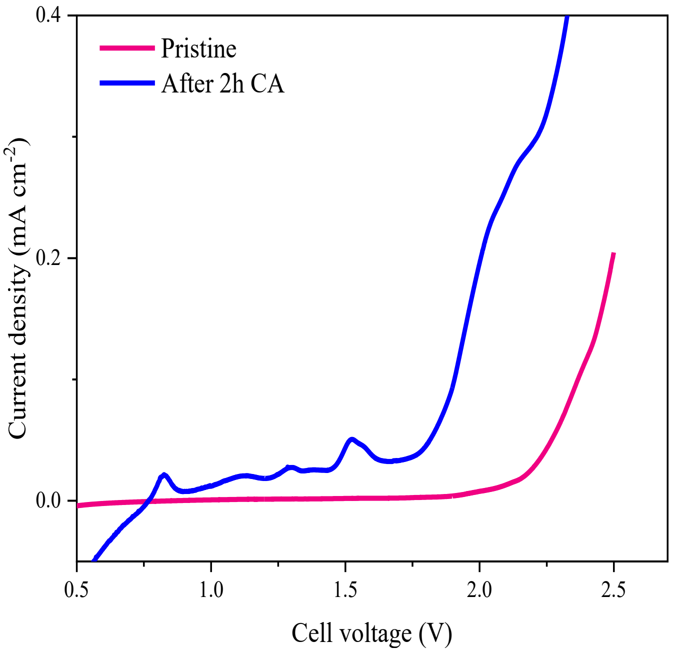

Figure 5.19 Effect of activation on the electrolyte: LSV of electrolyte after CA at 2 V for 2h

Figure 5.19 shows the LSV results compared to pristine electrolyte. The activated electrolyte exhibits oxidation peaks at ~0.8 V and ~1.5 V, confirming the presence of redox-active species released during activation. These species narrow the apparent electrochemical stability window and may interfere with the intended redox processes of the cell.

The use of an inert electrode ensures that the observed signals originate solely from dissolved species, not from interactions with active electrode material.

5.3.3.3 Effect of high voltage irreversibility on the CoSe cathode

To assess structural changes in the CoSe electrode, samples are analysed via XRD immediately after CA at 2 V for 2h. The diffractogram, shown in Figure 5.20, reveals a substantial decrease in reflection intensity, indicating that the long-range crystalline order of CoSe is lost upon high voltage pre-treatment. This behaviour is consistent with irreversible amorphisation or partial dissolution of the active material. The absence of a well-defined amorphous halo suggests that dissolution may play a significant role, as the crystalline phase disappears but the background does not increase markedly. The structural degradation is likely bounded to the significantly low initial capacity observed for Cells 1, 2 and 3.

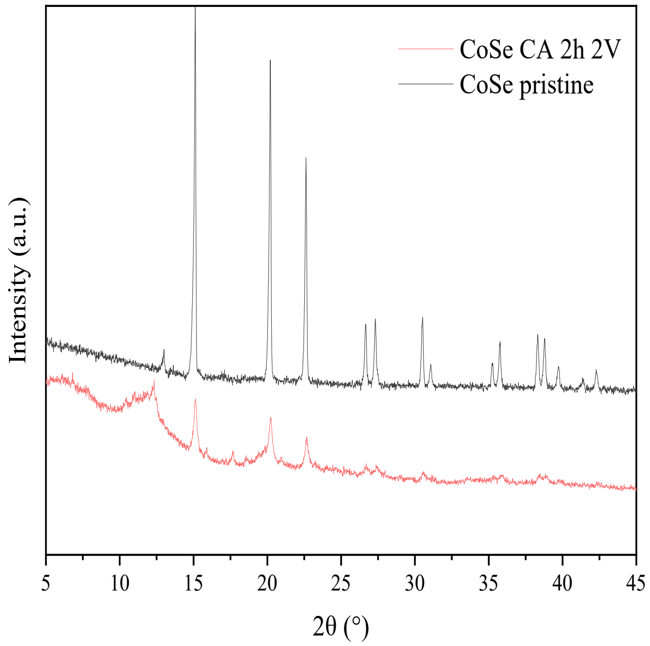

Figure 5.20 Effect of electrochemical activation on crystalline structure: X-ray diffractogram of CoSe after CA for 2h at 2 V

During Raman spectroscopy an interesting feature was observed, the peaks associated to C–Se peak and Co–Se bonds are removed during the preparation of the *ex situ* sample by electrode rinsing with 1,2-difluorobenzene. The comparison of the *ex situ* Raman spectra of electrodes after CA at 2 V for 2 h rinsed and unrinsed are presented in Figure 5.21. The rinsed sample (Figure 5.21a) shows an I_D/I_G ratio of 0.8, like the pristine sample, while the unrinsed sample (Figure 5.21 b) shows an I_D/I_G ratio close to 1, indicating partial loss of graphitic order due to electrolyte exposure.

Importantly, the C–Se peak at 675 cm^{-1} and Co–Se bands at 468 and 507 cm^{-1} observed in the pristine sample (Figure 5.2) are still present in the sample after CA at 2 V for 2h, albeit with reduced intensity. This suggests that amorphized CoSe remains in the electrode, likely contributing to the observed capacity.

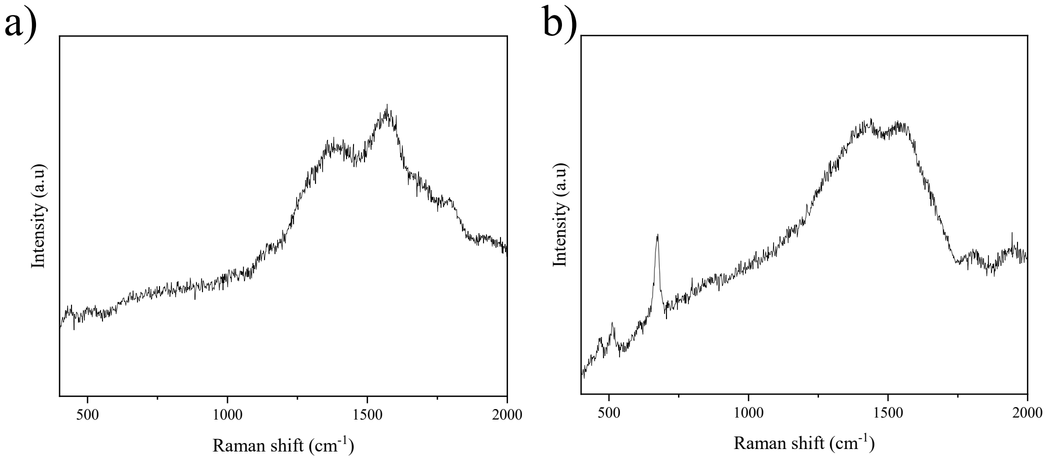

Figure 5.21 Effect of high voltage irreversibility on CoSe cathodes: Raman spectra of CoSe after CA for 2 h at 2 V a) rinsed with 1,2-difluorobenzene, b) not rinsed

It is worth noting that in an earlier reported experiment, where CoSe electrodes were soaked in the electrolyte, no detectable Raman features attributable to Co–Se or C–Se bonds were observed (Figure 5.11), indicating that the solid phase either dissolved or that any remaining species were too diluted to detect. In contrast, after electrochemical pre-treatment at 2 V for 2 h, distinct Raman bands corresponding to Co–Se and C–Se vibrations become evident. This difference likely arises from the different electrolyte environments in the two experiments. In the soaking test, the relatively large volume of electrolyte and the absence of confinement in the cell allowed dissolved Co and Se species to diffuse away from the electrode, effectively washing them out of the probed region. In the Swagelok cell used for electrochemical activation, however, the small electrolyte volume and limited diffusion space promote retention of the dissolved or redeposited species near the electrode surface, where they can reorganize or react to form amorphous Co–Se domains detectable by Raman spectroscopy. Thus, the appearance of Co–Se and C–Se bands after activation likely reflects the local enrichment and partial reconstruction of the active material within the confined cell environment.

5.3.4 Supporting Evidence for the Degradation Hypothesis

Although direct studies on the dissolution of CoSe in chloroaluminate-based ionic liquids are currently unavailable, the hypothesis that CoSe degrades via the formation of soluble species is supported by analogies with related systems and string thermodynamic basis.

Experimental evidence from similar environments confirms the tendency of both Se and Co to form soluble chloride complexes. For instance, Xu et al. reported the formation and shuttling of polyselenide species in chloroaluminate electrolytes [106]. Similarly, Fehrmann et al. demonstrated the dissolution of selenium tetrachloride ($SeCl_4$) in molten NaCl–$AlCl_3$ mixtures, confirming the affinity of Se for chloride coordination [107]. On the Co side Yao et al. investigated cobalt sulphide (Co_9S_8) and proposed a mechanism involving the substitution of Co^{2+} by Al^{3+}, leading to the formation of soluble cobalt-chloride complexes [54].

From a thermodynamic perspective, the dissolution of CoSe into the electrolyte is highly favourable. Both cobalt and selenium exhibit stronger bonding with chloride ions than with each other. The bond dissociation energies for Co–Cl (398 kJ mol^{-1}, [108]) and Se–Cl (322 kJ mol^{-1}, [108]) are higher than that of the Co–Se bond (287 kJ mol^{-1} [109]). This hierarchy (Co–Cl > Se–Cl > Co–Se) provides a clear driving force for the breakdown of the CoSe phase and the formation of soluble species during electrochemical cycling.

These insights support the interpretation that the high-voltage irreversible processes observed in the electrochemical data may involve the dissolution and migration of active species. This hypothesis is further examined through *ex situ* SEM-EDX analysis in the following chapter.

5.3.5 Remarks on the Reaction Mechanisms

CoSe presents an initial degradation upon contact with the electrolyte characterized by the dissolution of Co and Se species that undergo oxidation/reduction, and the formation of a secondary phase $CoSe_2$.

The electrochemical data, particularly the differential capacity plots, offer strong indications of the charge storage mechanism. The presence of multiple distinct peaks in the dQ/dV curves suggests that the reaction does not proceed as a single-step process. Instead, it likely involves either: (i) successive intercalation of chloroaluminate ions into different crystallographic sites within the CoSe lattice, or (ii) a multi-phase conversion reaction, where intermediate compounds form and transform during cycling.

The identification of $AlCl_4^-$ as the primary charge carrier, combined with the complexity of the redox features, supports the hypothesis of a layered or staged reaction pathway. However, distinguishing between intercalation and conversion mechanisms, and determining the exact stoichiometry and structural evolution of CoSe during cycling, requires real-time structural characterisation. Understanding of the charge storage mechanism is addressed in the next chapter using *in situ* and *operando* XAS as well as *operando* XRD. These techniques will allow direct observation of the structural and electronic changes occurring in the CoSe cathode during cycling, providing molecular-level insight into the proposed mechanisms.

The considerable loss in the long-range crystalline order of CoSe observed after the high voltage irreversibility further contributes to the degradation of CoSe. Nonetheless, the dissolved Co and Se species are retained or redeposited species near the electrode surface.

5.3.6 Remarks on the Degradation Pathways

Based on the electrochemical and theoretical discussion presented, the first cycle of CoSe cathodes is proposed to involve an initial irreversible transformation near 2.0 V. This transformation is marked by the appearance of a distinct cathodic peak near 1.0 V, which serves as a signature of the activation process. While this reaction is essential for enabling the main charge storage mechanism, it simultaneously initiates degradation pathways.

The dual nature of this process is clearly illustrated by the contrasting behaviour of Cell 0 and Cell 3. In Cell 0, the reaction occurs immediately, resulting in rapid activation but also accelerated capacity fade. In Cell 3, the process is delayed due to the replacement of cell components after CA pre-treatment. This delay allows the cell to undergo a controlled process, where the necessary species for electrochemical cycling form gradually, leading to improved stability and long-term performance.

By controlling the timing and conditions under which irreversible reactions occur, it is possible to decouple activation from degradation. This strategy is critical for optimizing the performance of CoSe cathodes and may be applicable to other transition metal chalcogenides in chloroaluminate-based RAB systems.

6 Mechanistic Elucidation and Degradation Pathways of Cobalt Selenide Cathodes via *In Situ* and *Operando* Characterisation

In compelling detective stories, the moment of revelation often arrives when the investigator realizes that the initial clues, though seemingly conclusive, were only fragments of a much larger and more intricate narrative. Similarly, the preceding chapters have uncovered critical evidence regarding the electrochemical behaviour and degradation of CoSe cathodes, challenging previously held assumptions. However, to fully understand the underlying mechanisms, it is necessary to move beyond static observations and examine the system in real time.

In this chapter the research presents a dynamic approach, employing *in situ* and *operando* characterisation techniques to directly observe the structural and chemical transformations occurring within the CoSe cathode during cell operation. These advanced methods provide molecular-level insights into the charge storage and degradation processes, offering a comprehensive understanding of the factors that govern performance and stability.

As demonstrated in Chapter 5, CoSe exhibits high initial specific capacity, but suffers from poor cycling stability. The complexity of the electrochemical profiles suggests that multiple, overlapping processes are at play, making it difficult to elucidate the reaction mechanisms using conventional *ex situ* techniques. While valuable for assessing pristine and post-cycled materials, *ex situ* methods offer only static snapshots, failing to capture the dynamic transformations that occur during operation.

To address this limitation, Chapter 6 is structured as follows:

- Section 6.1: Dynamic structural changes in CoSe cathode via *operando* X-ray diffraction.

- Section 6.2: Dynamic electronic and local structural changes in CoSe cathode via *operando* X-ray absorption spectroscopy Co-edge.
- Section 6.3: Dynamic electronic changes in CoSe cathode via *in situ* X-ray absorption spectroscopy (XAS) Se-edge.
- Section 6.4: Degradation mechanisms and products.
- Section 6.5: Remarks on characterisation.

By integrating *operando* XAS, *operando* and *in situ* SRD, and complementary *ex situ* techniques, this chapter constructs a detailed and dynamic picture of the processes governing CoSe cathode behaviour, providing a foundation for rational material design and optimisation.

6.1 Dynamic Structural Changes in CoSe Cathode via *Operando* X-ray Diffraction

Figure 6.1 presents a series of *operando* XRD diffractograms of CoSe collected during the first two cycles. The pattern reveals several key findings that inform the charge storage and degradation mechanisms.

The most prominent observation is the progressive broadening and reduction in the intensity of all reflections associated with the hexagonal CoSe phase (space group *P6₃/mmc),* suggesting a progressive amorphisation of the structure. The loss of long-range order suggests that the crystalline CoSe structure is consumed and replaced by less ordered or amorphous products. In addition to this global structural degradation, the emergence of new reflections corresponding to $CoSe_2$ phase (space group *Pa-3*) is observed, confirming the initial irreversible transformation process proposed in Chapter 5.

Another important observation is the predominance of Al anode reflections over those of CoSe, to resolve the behaviour of CoSe, in the following subsections the analysis will be done by grouping reflection depending on their tendencies. This targeted approach is necessary because the dominant diffraction peaks in the full scan originate from the Al anode, which can obscure subtle changes in the CoSe phase.

Disclaimer: The galvanostatic cycling plot is presented alongside the stacked diffractograms in Figure 6.1 to provide contextual information about the electrochemical conditions during *operando* measurements. However, due to the inclined and non-uniform background in the diffraction data the visual alignment between voltage and diffraction features is not direct. As a result, the time-voltage profile is not included in the figures of the following sections as it does not precisely correspond to the position of the stacked diffractograms.

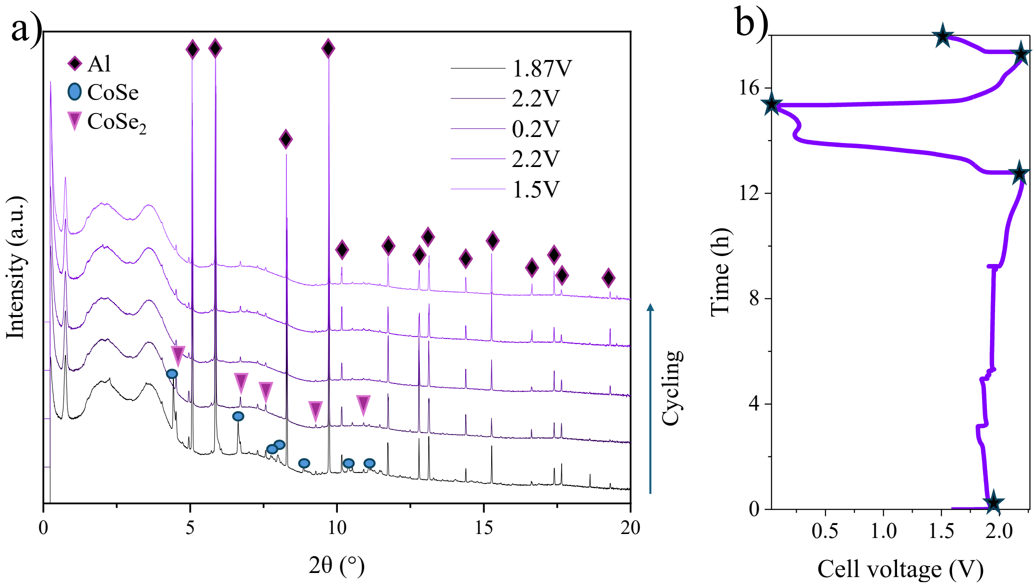

Figure 6.1 Structural changes in CoSe: a) *operando* XRD diffractograms at 1.87, 2.2 and 0.2 V during the first cycle and at 2.2 and 1.5 V, in the following cycle, b) charge/discharge curves of CoSe for *operando* XRD measurements (the points indicated represent when, during cycling, each diffractogram was taken)

6.1.1 Primary conversion reaction

Figure 6.2 focuses on selected 2θ intervals where reflection evolution follows a clear, monotonic trend, indicative of a well-defined phase transition. By isolating specific regions, the visibility of CoSe-related reflections is enhanced enabling a more accurate analysis of its structural evolution.

- Figure 6.2 a): The initial reflection at 4.43° (CoSe (101)) gradually diminishes until its complete disappearance, while a new reflection at 4.52° (CoSe$_2$ (210)) intensifies. This reciprocal behaviour is characteristic of a phase transition.

- Figure 6.2 b): A similar trend is observed for the CoSe (110) reflection at 6.64°, which fades as the $CoSe_2$ (311) peak at 6.71° grows.
- Figure 6.2 c): Subtle CoSe reflections at 7.98° and 7.99°, corresponding CoSe (201) and (112) planes, gradually disappear. This suggests that these planes, which are crucial to the hexagonal CoSe structure, are consumed during the conversion process and that it is not a reversible process.

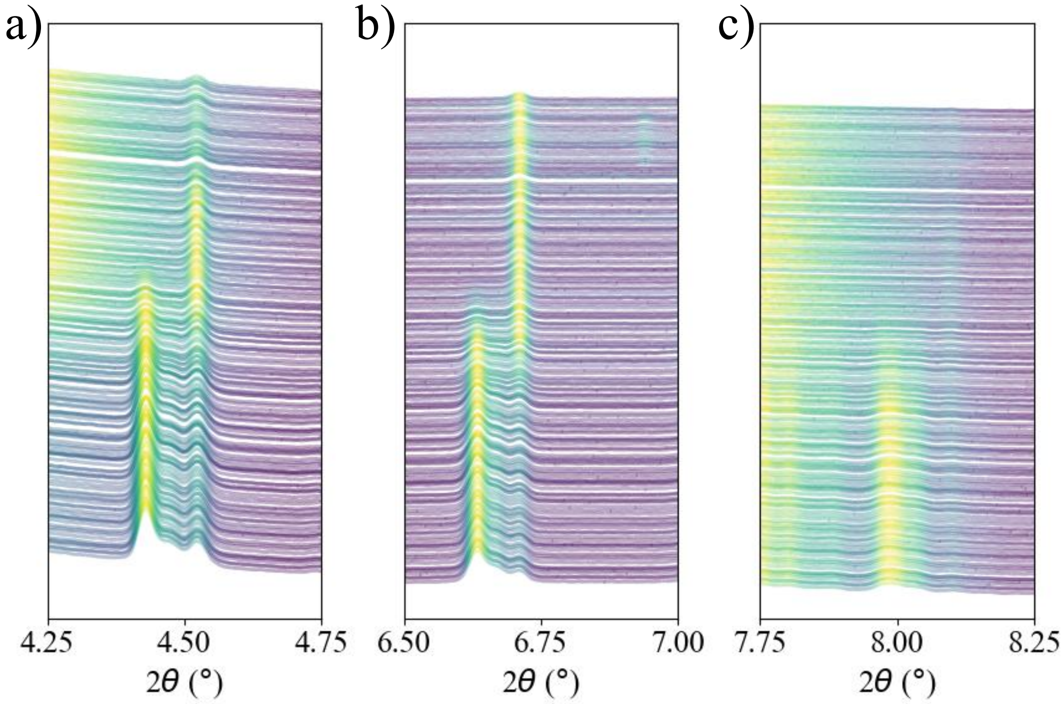

Figure 6.2 Primary conversion reaction. *Operando* XRD patterns focused on sections that present a monotonous reduction in CoSe reflections and increase in $CoSe_2$ reflections: a) 2θ = 4.25°–4.75°, b) 2θ = 6.5°–7°, c) 2θ = 7.75°–8.25°

These observations provide direct structural evidence for the phase transition of CoSe into $CoSe_2$. The disappearance of CoSe reflections and the rise of $CoSe_2$ reflections confirm that the charge storage mechanism involves a chemical transformation rather than ion insertion into a stable host lattice. This supports the hypothesis that the initial activation of the cathode involves a structural transformation of the CoSe, forming new phases and possibly releasing soluble cobalt species into the electrolyte.

An important note at this point is that the Rietveld refinement of the diffractograms indicate the formation of a monoclinic phase, Co_3Se_4 (space group *C12/m1*). While the refinement provides a plausible fit for the inclusion of this phase, the reliability of its quantitative analysis is significantly limited. Due to the predominance of Al reflections, the high number of reflections for Co_3Se_4 and their extensive overlap with the reflections of CoSe, $CoSe_2$, and the Al anode (reflections at 4.48°, 4.51°, and 4.53°, associated with Co_3Se_4 (111), (002), and (400) planes, are masked by the CoSe (101) plane reflection), the volume fraction reported in the refinement likely carries a high degree of uncertainty. For this reason, the analysis of the *operando* diffractograms focuses on the more prominent and well-defined reflections of the CoSe and $CoSe_2$ phases. Nonetheless, the inclusion of Co_3Se_4 in the refinement suggests it is an intrinsic part of the complex, multi-step conversion mechanism that governs the cathode's behaviour. We therefore consider its formation of Co_3Se_4 to be a plausible component of the overall structural transformation, while recognizing the quantitative limitations of this specific dataset.

The initial Rietveld refinement, which attempts to fit the diffractograms using only a two-dynamic phase model of CoSe and $CoSe_2$ and the fixed phase of Al anode, stays short after a few measurements, yielding a very poor fit (indicated by a high χ^2 value). This suggests the presence of an additional phase not accounted for in the model.

To improve the fit, a third phase, monoclinic Co_3Se_4, was introduced, which significantly reduces the χ^2 value and provides a more plausible fit to the overall pattern. While this three-phase model suggests the formation of Co_3Se_4 is likely, the strong peak overlap between Co_3Se_4 and the $CoSe_2$ phase significantly impacts the reliability of the quantitative volume fractions. Specifically, the numerous reflections of the Co_3Se_4 phase mask the signal of $CoSe_2$, causing the refinement to under-report the volume fraction of $CoSe_2$ and present it as a minor component.

Therefore, our primary evidence for the crystalline structure characterisation relies on the qualitative analysis of the *operando* data. As mentioned earlier, Figure 6.2 shows that there is a clear monotonous trade-off in the intensity of CoSe reflections and the appearance of new reflections corresponding to $CoSe_2$. This unambiguous visual trend confirms the phase transition of CoSe into $CoSe_2$ as the main charge storage mechanism, despite the quantitative limitations of the Rietveld refinement.

6.1.2 Complex and transient structural changes

While the primary phase transition from CoSe to $CoSe_2$ is characterized by a clear and monotonic evolution of diffraction peaks, the *operando* XRD data also reveal more complex and transient behaviours that cannot be explained by a single-phase transformation. These phenomena are presented in Figure 6.3, which highlights intervals where reflections fluctuate in intensity or appear and disappear unpredictably, likely attributed to intermediate species.

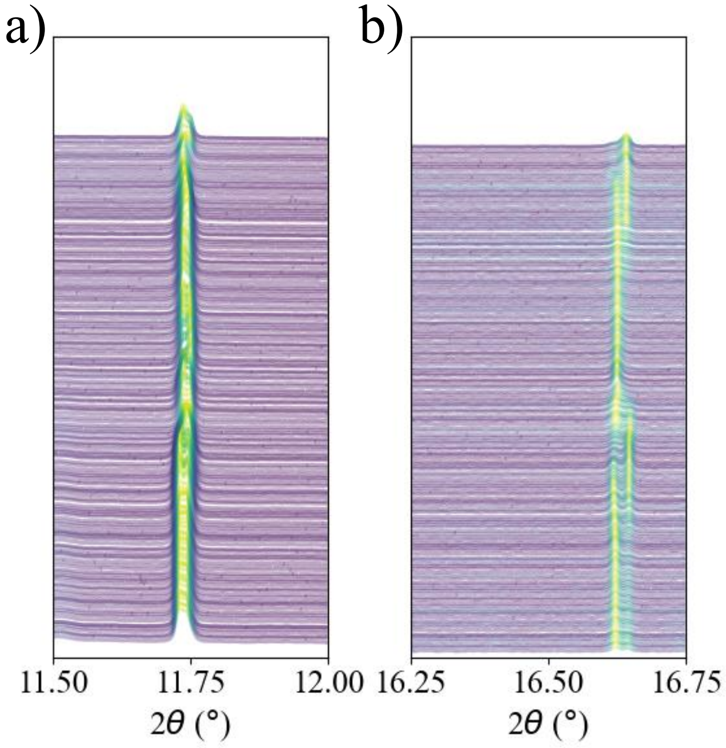

Figure 6.3 Transient structural changes: *Operando* XRD patterns focused on sections that present the formation and disappearance of transient Co_3Se_4 reflections a) 2θ = 11.5°–12°, b) 2θ = 16.25°–16.75°

- Figure 6.3 a): Disorganized changes in reflections corresponding to CoSe (301), (204), and (105), $CoSe_2$ (433), and multiple overlapping reflections from Co_3Se_4. The irregular intensification and attenuation of these reflections suggest the formation of transient intermediate species.
- Figure 6.3 b): Seemingly reversible amorphisation of the $CoSe_2$ (733) reflection at 16.61°, followed by the transient emergence of reflections likely associated with

Co_3Se_4 phase. This behaviour points to transient phase formation, and possible side reactions that contribute to a heterogeneous and dynamic response.

These observations indicate that the charge storage mechanism in CoSe cathodes is not a simple one-step process. Instead, it involves multiple intermediate phases, transient species, and competing structural transformations. The formation and disappearance of Co_3Se_4 reflections provide strong evidence for the existence of transient intermediates, which may play a role in both activation and degradation. This complexity underscores the need for real-time characterisation to capture the full scope of the structural evolution.

Co_3Se_4 was observed in a larger proportion at the *ex situ* characterisation after soaking (Figure 5.10) the more prominent presence in that instance can be associated to the sample preparation. Their presence underscores the importance of *in situ* and *operando* techniques, which avoid such artifacts and provide more reliable insights into real-time transformations.

6.1.3 Structural Changes and Peak Overlap With the Al Anode

Although the primary focus of this study is the CoSe cathode, *operando* XRD data also reveal structural changes in the Al foil anode, as shown in Figure 6.4. The interpretation of these observations is complicated by the fact that Al, being a highly crystalline foil, dominates the diffraction signal and overlaps with key CoSe reflections.

- Figure 6.4 a): A dominant Al (220) reflection is observed at 8.29° obscures adjacent CoSe and $CoSe_2$ reflections. Minor shifts and the formation of secondary reflections around 8.26° are observed.
- Figure 6.4 b): The Al (331) reflection at 12.80°, masks $CoSe_2$ adjacent reflections, and shows slights displacement to higher angles.
- Figure 6.4 c): The Al (420) reflection at 13.13° overlaps with reflections of $CoSe_2$, exhibits reversible intensity changes and the appearance of a new reflection at 13.11°.

These observations indicate dynamic behaviour in the Al-dominated regions during cycling. However, due to the bulk nature of XRD and the early stage of cycling, the origin of these shifts remains uncertain and is not attributed to specific phase transformations at the Al lattice.

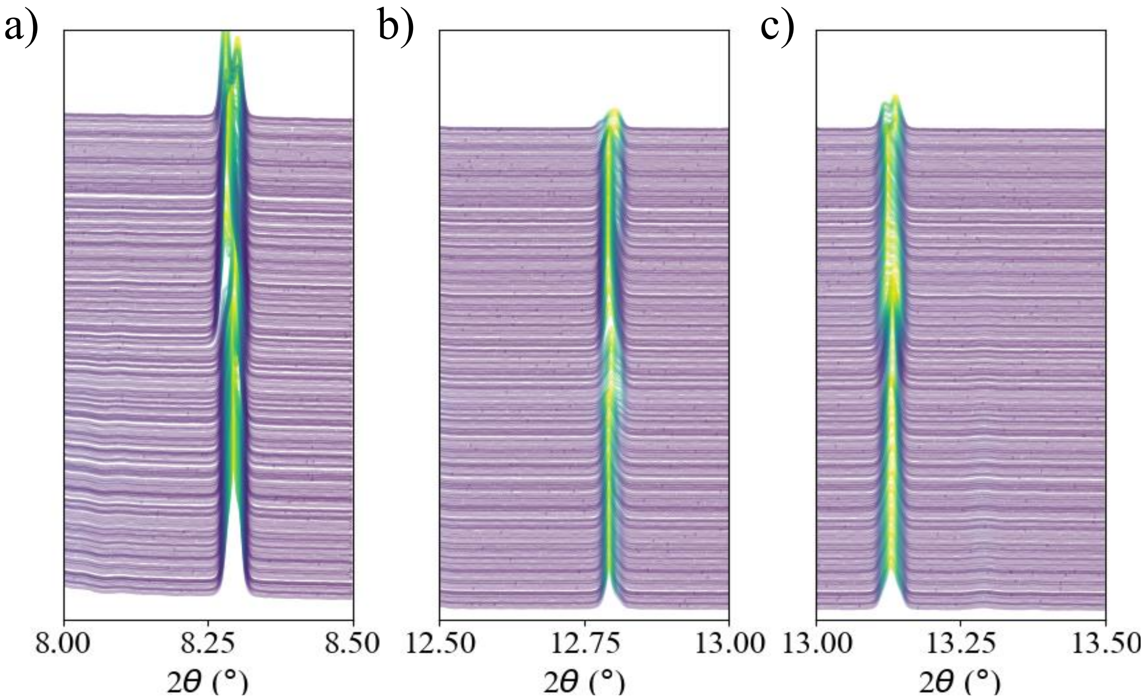

Figure 6.4 Structural changes in the Al Anode: *Operando* XRD patterns focused on sections that present changes in the reflections of Al anode a) 2θ = 8°–8.5°, b) 2θ = 12.5°–13°, c) 2θ = 13°–13.5°

6.1.4 Summary of the Dynamic Structural Changes

The *operando* XRD data provide a comprehensive overview of the structural evolution of CoSe cathodes during the first cycles. Three key phenomena are observed:

Decrease in the long-range order: the intensity of the CoSe reflections decreases considerably until the disappearance of some of them, this behaviour is consistent with the initial anisotropic dissolution observed in the soaked sample and could also be attributed to amorphisation of CoSe. It facilitates the release of Co atoms into the electrolyte, and upon cycling might lead to electrode pulverisation increasing the capacity loss

Crystalline phase transition: The clear, irreversible trade-off in reflection intensity between CoSe and $CoSe_2$ reflections indicates a well-defined crystalline-to-crystalline phase transition. This transformation appears to coincide with the onset of the irreversibility at high voltages that lead to infinite plateau at low current densities electrochemical plateau and rapid capacity loss at 1 Ag^{-1}.

Transient changes: the transient appearance of Co_3Se_4 reflections further supports the existence of transient intermediates and competing reaction pathways.

In summary, the *operando* XRD results reveal a dynamic, partially reversible transformation mechanism involving the conversion of CoSe into $CoSe_2$, through Co_3Se_4. These findings support the proposed degradation pathway involving structural rearrangement and possible dissolution, as discussed in earlier chapters. These insights underscore the complexity of the charge storage mechanism and point to potential strategies for improving stability, such as phase control, electrolyte optimisation, and interface engineering.

6.2 Dynamic Electronic and Local Structural Changes in CoSe Cathode via *Operando* X-ray Absorption Spectroscopy Co-Edge

To complement the structural insights obtained from *operando* XRD, *operando* X-ray absorption spectroscopy (XAS) at the Co K-edge is employed to probe the electronic structure and local coordination environment of cobalt during cycling. This technique enables the detection of subtle changes in oxidation state and bond distances, providing a deeper understanding of the redox behaviour and structural reorganisation of the CoSe cathode.

6.2.1 Analysis of electronic structure

Figure 6.5 presents the Co K-edge XANES spectra of the initial scan of the *operando* cell, alongside reference spectra for metallic cobalt (Co^0) and cobalt oxides (CoO and Co_3O_4). The initial scan of the CoSe electrode within the *operando* cell shows a nearly identical edge position and spectral shape to the pristine sample, suggesting that contact with the electrolyte does not immediately alter the oxidation state of cobalt. This stability implies that the initial interaction between the cathode and electrolyte is structurally benign.

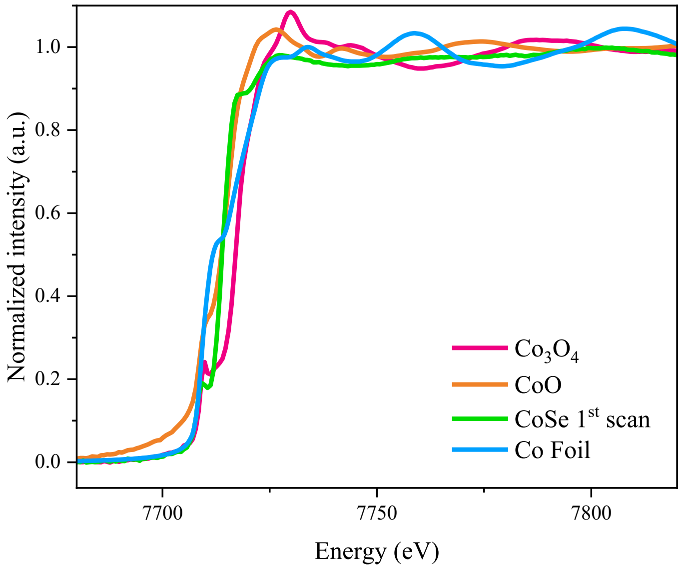

Figure 6.5 Electronic structure of CoSe: Co K-edge XANES spectra of the CoSe 1st scan Co foil, Co_3O_4 and CoO

Figure 6.6 shows the cascade of Co K-edge XANES spectra collected during cycling. Notably, no significant shift in the absorption edge is observed throughout the charge and discharge process. The absence of any substantial edge shift indicates that Co remains predominantly in its pristine oxidation state and does not participate in a redox reaction during cycling. This finding strongly supports the hypothesis that the electrochemical activity of the CoSe cathode is primarily driven by Se redox processes, rather than Co.

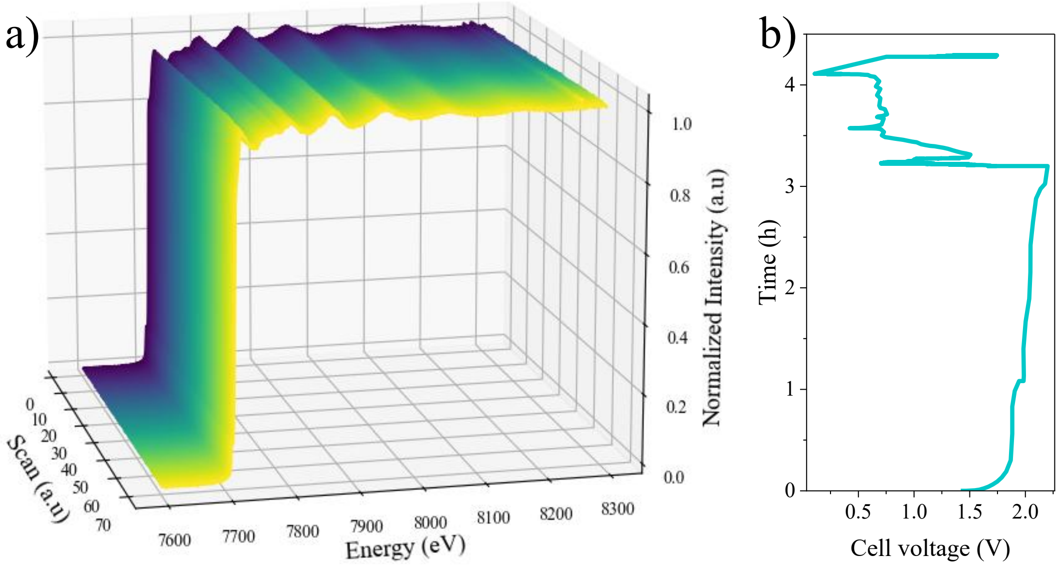

Figure 6.6 Electronic structure of CoSe: a) cascade of *operando* XAS Co-edge spectra, b) GCPL profile of the *operando* cell

The galvanostatic charge/discharge curve shown in Figure 6.6 b) exhibits a "bumpy" profile, which is attributed to intermittent electrode-electrolyte contact caused by gas bubble formation within the pouch cell, a known artifact in this type of setup. While this does not affect the interpretation of the XAS data, it highlights the challenges of *operando* measurements, those challenges were overcame as observed in the *operando* SRD characterisation, performed before XAS.

6.2.2 Analysis of local structure

To investigate the local structural changes around cobalt atoms, a Fourier transform of the extended X-ray absorption fine structure (EXAFS) was performed. Figure 6.7 presents the FT-EXAFS spectra during the initial charge process.

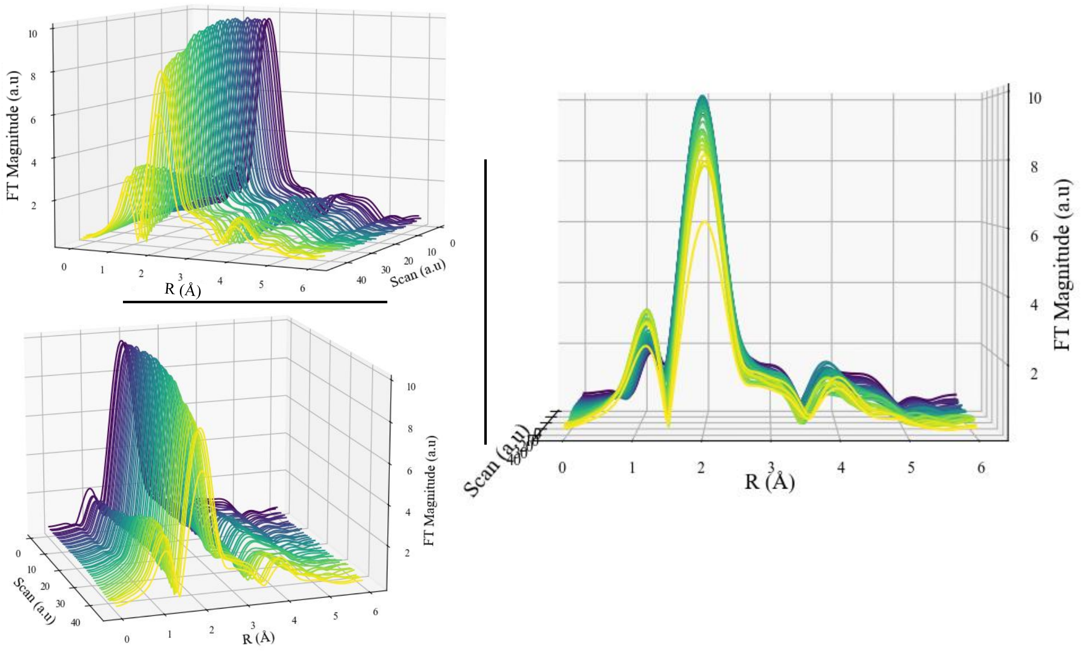

Figure 6.7 Local structure of CoSe: cascade of Co K-edge XAS spectra -FT EXAFS spectra for the initial charge process from different points of view

The first coordination shell, corresponding to the Co–Se bond, appears as a prominent peak at approximately 1.8 Å. During charging, this peak shifts slightly to higher R-values and its intensity decreases progressively. These changes indicate a weakening and elongation of the Co–Se bond, as well as a reduction in the coordination number of selenium atoms around cobalt. This behaviour is consistent with increased structural disorder and supports the hypothesis of cobalt dissolution and CoSe amorphisation during cycling, occurring without a change in the oxidation state of cobalt. Furthermore, considering that the oxidation state of Co remains unchanged, it is proposed that the dissolved species is $Co(AlCl_4)_2$ since during the charge this species is formed by the plating of Al at the anode surface, becoming the most abundant.

The second coordination shell, likely associated with Co–Co interactions, shows an increase in intensity during charging, suggesting the formation of new cobalt-containing phases and changes in the long-range order of the crystal lattice, consistent with the emergence of Co_3Se_4 and $CoSe_2$ phases observed in XRD.

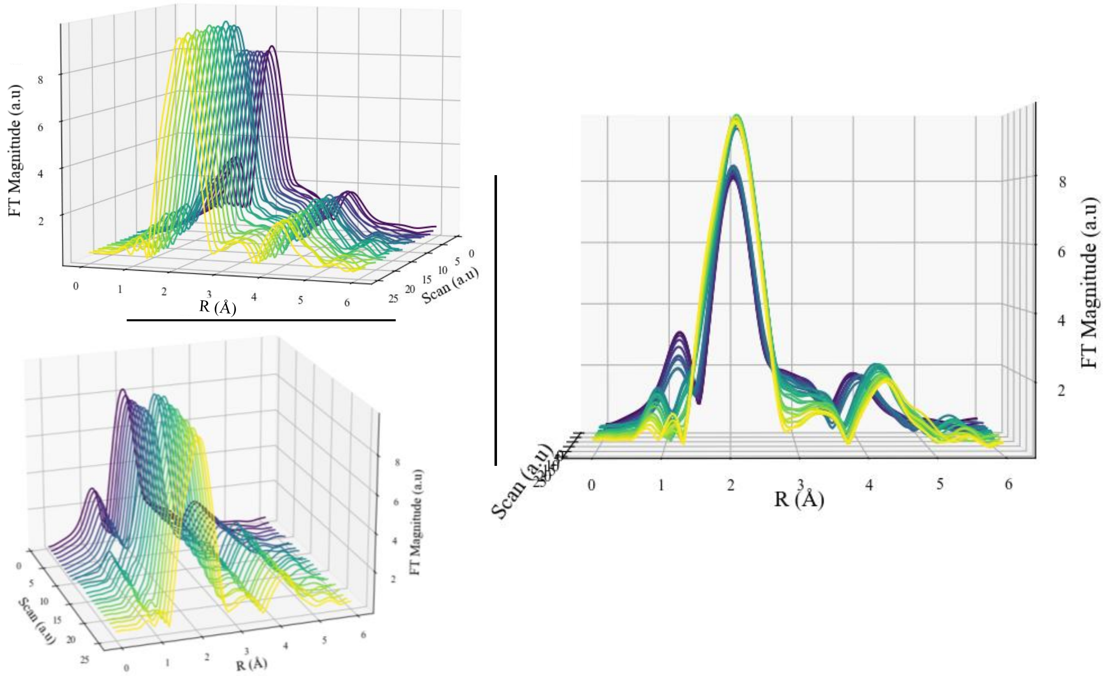

Figure 6.8 Local structure of CoSe. Cascade of Co K-edge XAS spectra FT EXAFS spectra for the initial discharge process from different points of view

During discharge (Figure 6.8), the intensity of the first coordination shell increases, but does not return to its original value. The partial intensity recovery indicates that the structural disorder introduced during charging is not completely reversible. The increase in coordination shell is consistent with the formation of the $CoSe_2$ phase, which features a higher number of Se neighbours around Co. The second and higher coordination shells also increases in intensity and shift to higher R-values, reflecting reorganisation and stabilisation of the crystal lattice in the newly formed phase.

6.2.3 Correlation with XRD

The XAS results are highly consistent with the findings from the *operando* XRD analysis. The phase transition from CoSe to $CoSe_2$ and Co_3Se_4, accompanied by a progressive amorphisation is confirmed by the weakening of the Co-Se bonds and the increase in structural disorder observed in EXAFS.

The XAS results provide electronic-level confirmation of Co dissolution, which occurs without a change in the oxidation state of Co, explaining the absence of redox features in the XANES spectra. This reinforces the conclusion that Se is the redox-active species, while Co undergoes structural reorganisation and partial dissolution.

Together, the *operando* XRD and XAS data present a coherent picture of the charge storage mechanism in CoSe cathodes: an amorphisation of CoSe, and phase transition of its crystalline structure to $CoSe_2$ accompanied by $Co(AlCl_4)_2$ dissolution, which contributes to both activation and degradation. Additionally, the Co demonstrates to be electrochemically inert.

6.3 Dynamic Electronic Changes in CoSe Cathode Via I*n Situ* X-ray Absorption Spectroscopy (XAS) Se-Edge

Following the *operando* Co K-edge XAS results, which demonstrated that Co remains electrochemically inactive during cycling, it became essential to investigate the role of Se in the charge storage mechanism. To this end, in house *in situ* XAS at the Se K-edge is performed to probe the electronic structure evolution of selenium during the first cycle.

6.3.1 Analysis of Electronic Structure

Three sequential measurements, each lasting five minutes, are conducted at constant voltages throughout the first cycle. The resulting spectra are averaged and smoothed to reduce noise and facilitate interpretation. The processed curves are presented in Figure 6.9. Due to the pouch cell configuration, significant background interference from other cell components was present, particularly in the pre-edge and post-edge regions. As a result, the analysis focuses on the rising edge region, where qualitative shifts in absorption energy can still be discerned.

Despite these limitations, subtle but consistent changes are observed in the Se K-edge position during cycling. To better visualize these shifts, the first derivative of the spectra is shown in Figure 6.10.

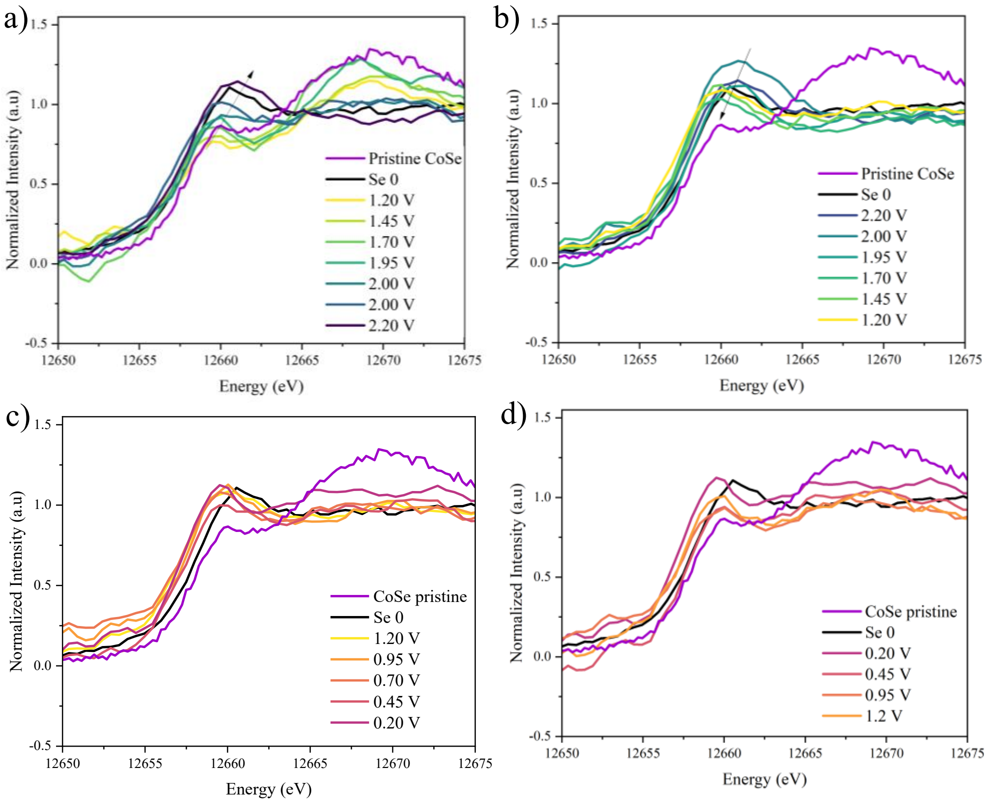

Figure 6.9 Electronic structure of CoSe: *in situ* Se K-edge XAS spectra of CoSe cathode for the first cycle a) from OCV to 2.2 V, b) from 2.2 to 1.2 V, c) from 1.2 to 0.2 V, d) from 0.2 to 1.2 V

During charging (Figure 6.9 a) and Figure 6.10 a), a slight shift of the absorption edge to higher energies is detected approaching the energy position characteristic of elemental selenium (Se^0), but given the differences in local bonding environments, this does not conclusively indicate full oxidation to Se^0. The possibility of intermediate species, such as polyselenides, cannot be ruled out and may contribute to the observed spectral features. This shift reverses during discharge (Figure 6.9 b) and Figure 6.10 b), indicating a return toward the selenide (Se^{2-}) state.

It is important to note that the Se K-edge position for Se^{2-} compounds varies within a narrow range—typically between 12656.0 eV (CuSe) and 12658.0 eV (SeS_2) [95] Therefore, large shifts were not expected. However, the observed trend is consistent with a reversible redox process, where selenium is oxidized during charging and reduced during discharge.

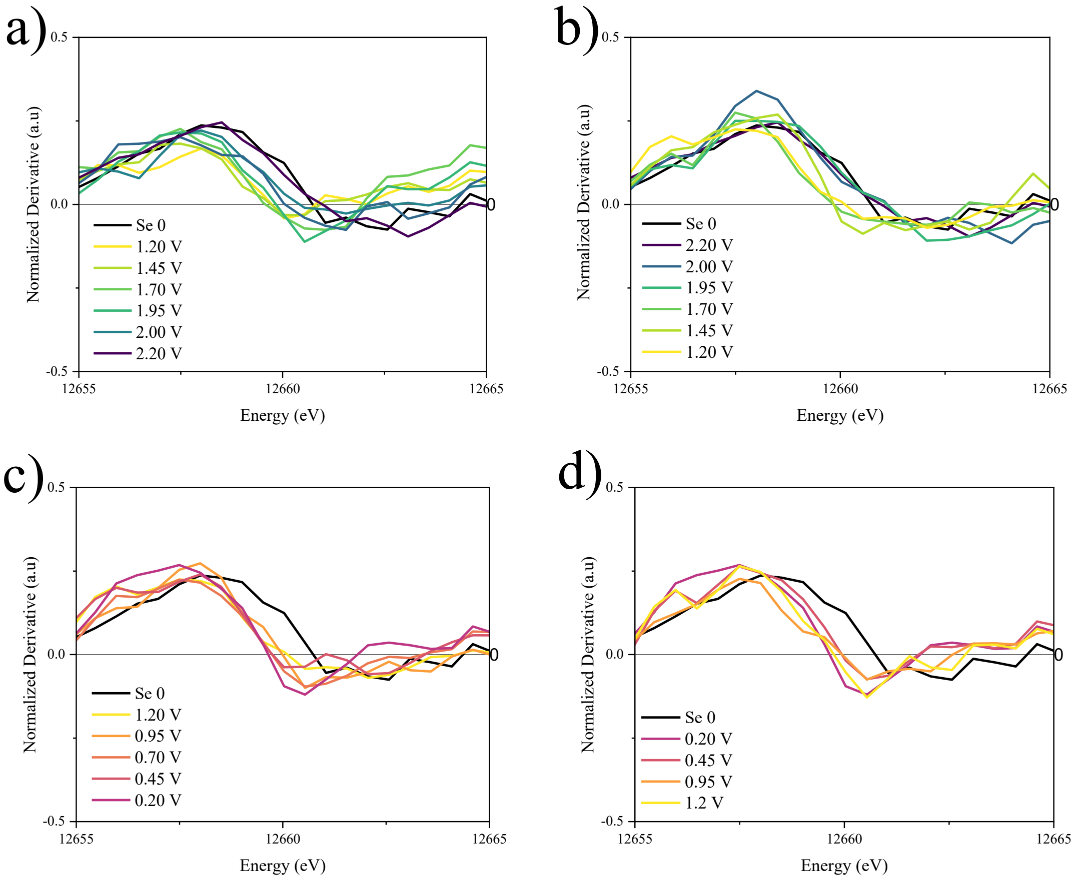

Figure 6.10 Derivative of the Se K-edge XAS spectra of CoSe cathode for the first cycle a) from OCV to 2.2 V, b) from 2.2 V to 1.2 V, c) from 1.2 V to 0.2 V, d) from 0.2 V to 1.2 V

More pronounced changes are observed in the white-line region (edge maxima). Both the energy and intensity of the white line increase upon charging and decrease during discharge. This behaviour aligns with findings by Olegario et al [96], who demonstrated that the Se K-edge white-line intensity and position correlate with selenium's oxidation state. These results provide strong evidence that selenium undergoes a reversible redox reaction from Se^{2-} to Se^{1-} and back, confirming its role as the electrochemically active species in the CoSe cathode.

6.3.2 Se redox activity

The *in situ* Se-K edge XAS analysis provides conclusive evidence that the electrochemical activity of the CoSe cathode is governed by the reversible oxidation and reduction of Se. This finding complements the Co K-edge XAS results, which shows no significant change in the oxidation state of Co during cycling.

The redox activity of Se is consistent with the structural transformation from CoSe to $CoSe_2$ and its amorphisation observed in *operando* XRD and supports the hypothesis that cobalt plays a structural role, while selenium is responsible for the electrochemical functionality. Nonetheless, without definitive confirmation of full oxidation, raises the possibility of intermediate species such as polyselenides. These species have been reported in other selenium-based battery systems and may contribute to selenium dissolution and long-term degradation.

6.3.3 Proposed Charge Storage Mechanism

Based on the combined findings from electrochemical testing, *operando* XRD, and *in situ/operando* XAS, a comprehensive mechanism for charge storage and degradation in CoSe cathodes can now be proposed.

The main charge storage process is proposed to involve a partially reversible phase transition, driven by the redox activity of selenium. *Operando* SRD reveals a phase transition from hexagonal CoSe to cubic $CoSe_2$, while Se K-edge XAS confirms a reversible shift in selenium's oxidation state between Se^{2-} and a more oxidized form. The

Co K-edge XAS shows no significant change in cobalt's oxidation state, indicating that cobalt remains electrochemically inactive and plays a structural role.

The mechanism begins with an irreversible activation step, where the pristine CoSe irreversibly converts into an amorphous Co–Se matrix and crystalline $CoSe_2$ via a transient intermediate Co_3Se_4. This transformation is accompanied by the formation of soluble cobalt chloroaluminate species, suggesting that $AlCl_4^-$ anions participate in the reaction as charge carriers.

$$6CoSe + 6AlCl_4^- \longrightarrow Co_3Se_4 + 3Co(AlCl_4)_2 \text{ (soluble)} + (Se_2)^{-2} + 4e^- \quad \text{(Chem. Eq. 6.1)}$$

The phase transition from Co_3Se_4 to $CoSe_2$ could happen through reintegration of $(Se_2)^{-2}$ (chem. Eq. 6.2) or further dissolution of $Co(AlCl_4)_2$(chem. Eq. 6.3)

$$Co_3Se_4 + 2(Se_2)^{-2} \longrightarrow 3CoSe_2 + 2e^- \quad \text{(Chem. Eq. 6.2)}$$

$$Co_3Se_4 + 2AlCl_4^- \longrightarrow 2CoSe_2 + Co(AlCl_4)_2 + 2e^- \quad \text{(Chem. Eq. 6.3)}$$

The phase transition reaction can be simplified as:

$$6\ CoSe + 6AlCl_4^- \longrightarrow 3CoSe_2 + 3Co(AlCl_4)_2 + 6e^- \quad \text{(Chem. Eq. 6.4)}$$

Or

$$6\ CoSe + 8AlCl_4^- \longrightarrow 2CoSe_2 + 4Co(AlCl_4)_2 + (Se_2)^{-2} + 6e^- \quad \text{(Chem. Eq. 6.5)}$$

While the Se K-edge shifts approach the energy of elemental Se^0, the bonding environment differs, and the formation of Se^0 cannot be conclusively confirmed. The possibility of amorphous polyselenide species forming during charging remains open possible for future investigation.

Subsequently, the reversible capacity is proposed to arise from the reversible oxidation and reduction of Se within the amorphous CoSe

$$2Se^{2-} \rightleftarrows (Se_2)^{-2} + 2e^- \quad \text{(Chem. Eq. 6.6)}$$

6.3.4 Remarks on the Real-Time Probing

The integration of *operando* SRD and XAS and *in situ* XAS has provided a holistic, real-time view of the CoSe cathode's behaviour. The core electrochemical activity is governed by a Se redox couple (Se^{2-}/Se^{-1}, potentially Se^{0}) at an amorphous CoSe and a phase transition from CoSe to $CoSe_2$. Simultaneously, a degradation process is proposed to occur, characterized by $Co(AlCl_4)_2$ dissolution.

This dual-process mechanism explains the electrochemical performance observed in Chapter 5: the initial high capacity, the distinct voltage plateau and the continuous capacity fade over extended cycling. The following section will address the degradation process that leads to the observed capacity fade.

6.4 Degradation Mechanisms and Products

Up to this point, the analysis using electrochemical, *in situ*, and *operando* techniques has revealed the charge carrier, proposed a feasible charge storage mechanism, and identified a likely degradation pathway for CoSe electrodes. Moreover, repeated cycling introduces additional degradation mechanisms that progressively compromise the electrode's integrity and performance. This section presents *post mortem* measurements that support and validate the proposed degradation mechanism, offering additional evidence for the structural and chemical transformations occurring during cycling.

6.4.1 Effect of Cycling on the Degradation of the Cathode

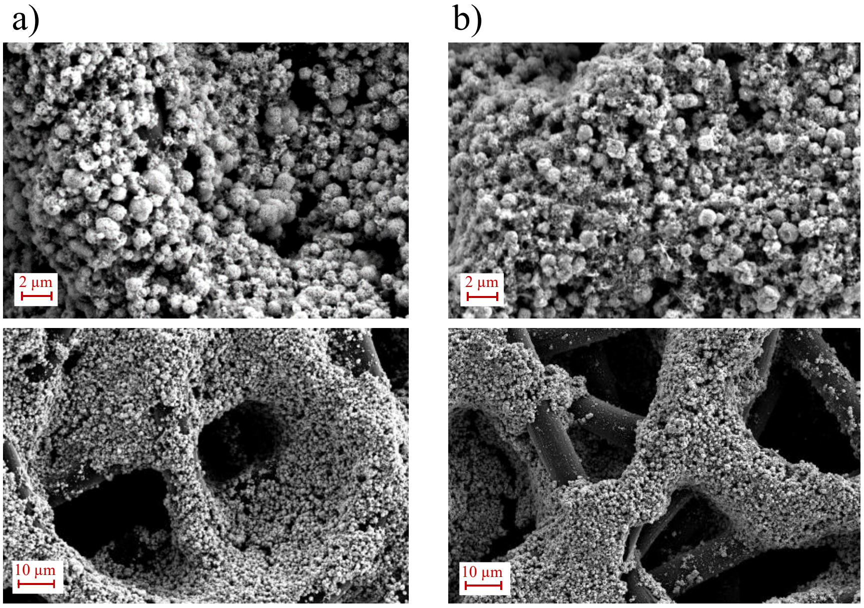

Figure 6.11 Cathode degradation: SEM images of CoSe electrodes a) pristine, b) after 20 cycles

To assess the morphological changes in the CoSe cathode after cycling, SEM imaging is performed on electrodes retrieved after 20 cycles. The results, shown in Figure 6.11, reveal significant structural deterioration.

CoSe particles appear porous and fragmented, with some regions of the C Paper current collector completely exposed and lacking active material. This suggests a loss of electrical contact and active mass, consistent with the dissolution and structural breakdown observed during early cycling stages.

These findings confirm that degradation continues beyond the initial dissolution and high voltages irreversibilities, contributing to capacity fade and reduced long-term stability.

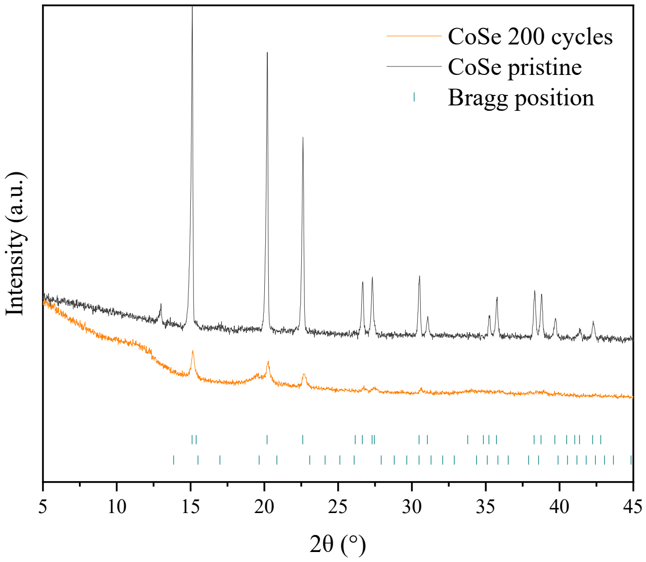

Figure 6.12 Effect of cycling degradation on crystalline structure: X-ray diffractogram of CoSe after 200 cycles

XRD analysis of CoSe electrodes after 200 cycles reveals extensive loss of long-range order, as shown in Figure 6.12. Compared to the already degraded structure observed after 2 hours of CA at 2 V, the reflections are further diminished, indicating a progressive loss of crystallinity during cycling.

This structural collapse is consistent with the initial phase transition, and dissolution mechanisms previously described and reinforces the role of amorphisation in long-term degradation.

Moreover, Raman spectroscopy of cycled CoSe electrodes (Figure 6.13) reveals higher intensity in the C–Se and Co–Se bands compared to electrodes subjected CA pre-treatment at 2 V for 2 h (Figure 5.11). This indicates that repeated cycling promotes the partial reorganisation or redeposition of Co–Se species that are otherwise lost or dispersed during the static activation process. In contrast to the unidirectional CA polarisation, the alternating potential during cycling likely facilitates dynamic dissolution–redeposition equilibria, in which dissolved cobalt and selenium species transiently migrate into the electrolyte and subsequently reincorporate into the cathode surface.

Such behaviour is consistent with the hypothesis that the reversible redox reaction occurs at the amorphous lattice. It also aligns with the detection of cobalt deposits on the Al anode after extended cycling (Section 6.2.1), indicating that Co migration is at least partially reversible and closely linked to the electrochemical degradation and recovery dynamics of the CoSe cathode.

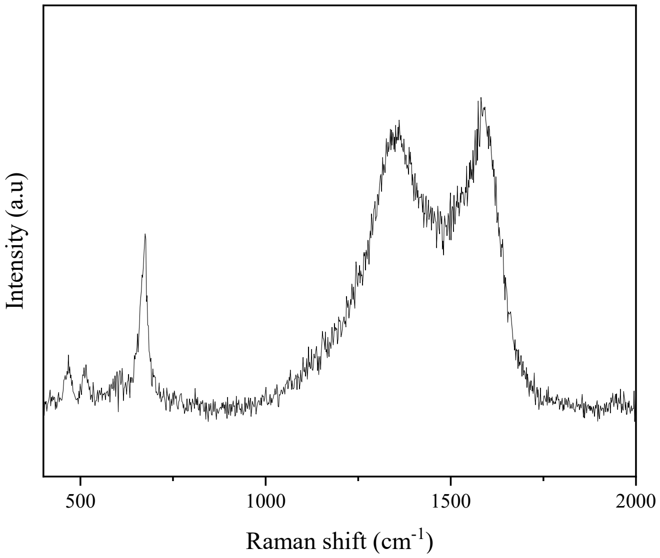

Figure 6.13 Effect of cycling degradation on chemical structure: Raman spectra of CoSe after 200 cycles

6.4.1 Effect of Cycling on the Degradation of the Anode

To investigate the impact of cathode degradation on the Al anode, SEM-EDX analysis was conducted on foils retrieved after 5 and 20 cycles. Figure 6.14 shows clear cobalt deposits on the Al foil after 20 cycles, providing direct evidence of cobalt migration from the cathode to the anode.

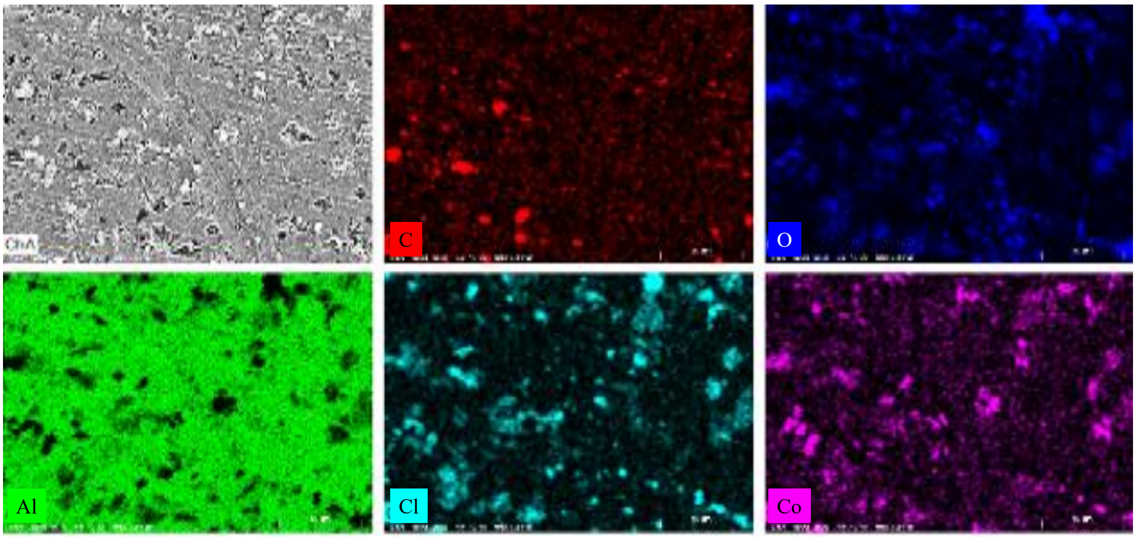

Figure 6.14 Effect of cathode degradation on the anode: SEM-EDX analysis of Al foil after 20 cycles

The comparison of the *ex situ* SEM-EDX analysis of the Al anode after the CA pre-treatment, where no detectable Co or Se deposits were observed on the anode surface, with the *ex situ* SEM-EDX analysis after 20 cycles suggests limited cross-electrode migration at the pre-treatment stage (Figure 5.17). However, as shown in Figure 6.14, clear cobalt deposits appear on the Al foil after 20 cycles, providing direct evidence of progressive Co migration from the cathode during extended cycling. This observation supports the hypothesis that cathode dissolution and redistribution of $Co(AlCl_4)_2$ species occur gradually, with deposits likely growing or aggregating on the anode surface over time.

Such cobalt deposition can contaminate the anode, interfering with Al plating/stripping processes and thereby accelerating capacity fading. Although selenium was not detected in the post-cycling anodes, this may not exclude its migration. Given the prior evidence of Se dissolution from the cathode, it is plausible that Se species also migrate but are removed during the mandatory washing step with 1,2-difluorobenzene required to prevent SEM chamber corrosion. Consequently, both Co and Se dissolution demonstrate to contribute to the long-term degradation processes

6.4.2 Remarks on the Degradation Mechanisms and Products

The high voltage irreversibility is attributed to the dissolution of $Co(AlCl_4)_2$, and occurs concurrently with the primary phase transition and amorphisation. Therefore, it is considered to be responsible of both activation and degradation of the cathode, as proposed in Section High Voltages Irreversibility5.3.3, and further confirmed by the increased structural disorder observed in the XAS. The dissolved cobalt, which remains in the pristine oxidation state, degrades the structure of active material, likely leading to cathode pulverisation and deposits at the anode, hindering Al plating and stripping and contributing to fast capacity loss.

The CoSe cathode undergoes multi-stage degradation, beginning with initial dissolution during cell assembly and continuing through cycling. This degradation manifests as:

- Structural breakdown of CoSe particles
- Loss of active material
- Amorphisation of the crystal lattice
- Migration and deposition of cobalt on the Al anode

The degradation is driven by a shuttling mechanism, where Co dissolves into the electrolyte and forms thermodynamically stable chloroaluminate complexes, such as $Co(AlCl_4)_2$. These complexes are dissolved in the electrolyte and migrate toward the anode, where they deposit and interfere with interfacial processes.

The complex charge storage mechanism and degradation pathway is visually summarized in Figure 6.15, which schematically depicts:

- The formation of soluble $Co(AlCl_4)_2$
- $Co(AlCl_4)_2$migration through the electrolyte
- Final deposition of $Co(AlCl_4)_2$ on the Al anode
- The phase transition of CoSe to $CoSe_2$
- The formation of amorphous CoSe
- The Se redox reaction within the amorphous lattice

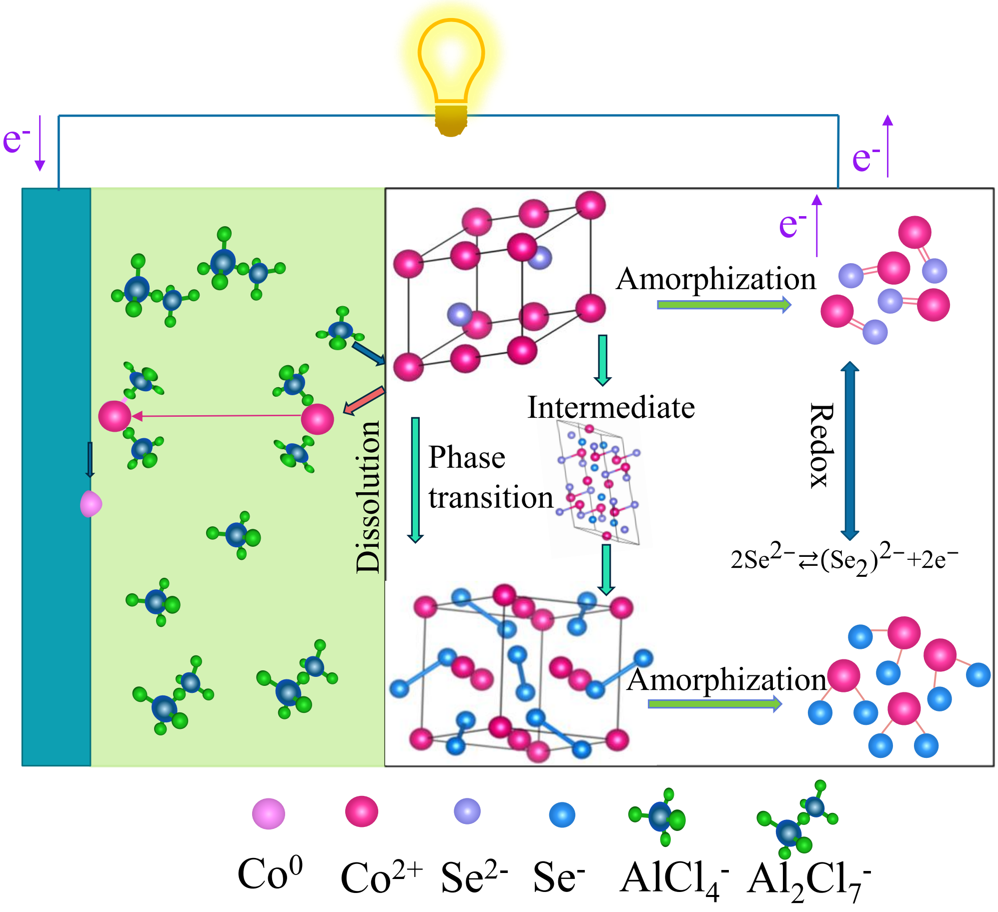

Figure 6.15 Schematic of charge storage mechanism and degradation pathway of CoSe cathodes

6.5 Remarks on characterisation

The integration of electrochemical, *ex situ*, *in situ*, and *operando* characterisation techniques has enabled the comprehensive understanding of the charge storage and degradation mechanisms of CoSe cathodes in RABs for the first time. This multifaceted approach has provided unprecedented insight into the dynamic processes governing electrode behaviour, from initial activation to long-term degradation.

The results presented in this dissertation emphasize two key phenomena: (i) The reversible redox activity of selenium, which drives the primary charge storage mechanism via a conversion reaction from CoSe to $CoSe_2$ and (ii) The irreversible dissolution of cobalt, which contributes to structural degradation, loss of active material, and contamination of the Al anode.

These findings highlight the need for strategies to suppress transition metal migration and minimize parasitic reactions to improve the long-term stability of CoSe-based RABs.

Table 6.1 Summary of characterisation techniques

Technique	Observation	Mechanistic implication
Pristine characterisation (XRD, Raman, XAS SEM)	Structural, morphological, and electronic properties of CoSe	Establishes baseline for comparison; confirms material purity and morphology
CV	Redox behaviour, current voltage profiles	Identifies Se redox activity; reveals multistep nature of cycling
GCPL/differential capacity (dQ/dV)	Voltage profiles capacity retention	Tracks long-term performance; highlights kinetic changes and activation behaviour
LSV and PEIS	Electrochemical stability window and impedance spectra	Assesses electrolyte degradation, interfacial resistance, and activation effects
CA	Current response under constant voltage	Identifies activation behaviour and dissolution dynamics at 2 V
***Ex situ* SEM-EDX**	Morphology and elemental distribution	Visual evidence of cathode degradation and Co migration to anode
***Ex situ* XRD, Raman and XAS**	Crystalline, molecular, and electronic structure changes	Confirms phase transitions, amorphisation, and dissolution of active material
***Operando* SRD**	Real- time phase evolution	Reveals CoSe → $CoSe_2$ conversion and intermediate Co_3Se_4 formation
***Operando* and *in situ* XAS**	Oxidation state and local atomic structure	Confirms Se redox activity; Co remains electrochemically inactive
ICP-OES	Elemental analysis of electrolyte	Detects dissolved Co and Se; confirms chemical degradation and shuttling

Importantly, the insights gained here are not limited to CoSe. They can be extrapolated to a broader class of transition metal chalcogenides and oxides, such as Co_9S_8, MoS_2, and V_2O_5, where similar dissolution phenomena have been linked to poor cyclability and capacity fading. Understanding the dissolution dynamics and redox behaviour in chloride-rich electrolytes offers a valuable framework for designing more stable and reversible multivalent batteries.

The techniques employed and their contributions to the mechanistic understanding are summarized in Table 6.1, providing a concise overview of the characterisation strategy and its implications.

7 MXenes as Functional Passive Components

In the prologue, the foundation was laid: "art imitates life". The resolution of a complex case often reveals the beginning of another. This principle, central to detective fiction and true crime, finds a parallel in scientific inquiry. Just as Agatha Christie's The A.B.C. Murders unravels a seemingly disconnected series of events into a single, intricate plot, this chapter builds upon the findings of previous investigations into CoSe to explore a new, interconnected challenge.

MXenes (two-dimensional transition-metal carbides/nitrides) are widely studied in battery research because of their combination of high electronic conductivity, tuneable surface chemistry, large specific surface area and mechanical robustness. In RABs research most publications have focused on MXenes as active materials [47], or as components of composites that help to mitigate active-material dissolution [54]. Reports of MXenes used explicitly as passive cell components (for example as separator coatings, binder replacements, or dedicated current-collector coatings) are comparatively scarce. This gap is surprising, because several intrinsic MXene properties—chemical tunability, film-forming ability, strong adhesion, and potential to block or adsorb dissolved species—are precisely those that could address common RAB problems (corrosive chloroaluminate electrolytes, transition-metal dissolution and shuttle, and poor interfacial stability) and that are showing promising results in LIBs[70], [110]. In this chapter we therefore explore MXene films and coatings in passive roles (interlayers, separator coatings and conductive interphases) and evaluate how their physical and chemical properties can be exploited to improve electrode and cell stability in corrosive RAB electrolytes.

While CoSe was the primary focus of this thesis, the insights gained now serve as a foundation for examining the versatility of $Ti_3C_2T_X$ MXenes. In this chapter, MXenes are studied not as active materials, but as functional passive components in RABs, including their roles as current collectors, binders, and separator modifiers.

This chapter is structured as follows:

- Section 7.1: Physicochemical and structural characterisation of $Ti_3C_2T_X$.
- Section 7.2: Evaluation of $Ti_3C_2T_X$ as a current collector.
- Section 7.3: Integration of $Ti_3C_2T_X$ into separators to suppress active species shuttling.

Through this exploration, it is demonstrated how strategic incorporation of $Ti_3C_2T_X$ can significantly enhance the practical viability and engineering of next-generation RABs.

7.1 Physicochemical and Structural Characterisation of Pristine $Ti_3C_2T_X$

The development of high-performance batteries requires more than optimizing active materials. The passive components, those that support, connect, and stabilize the system, play a critical role in determining overall efficiency, safety, and longevity. This is especially true in RABs, where the highly corrosive chloroaluminate IL-based electrolytes severely limit the choice of compatible materials, often leading to corrosion, increased impedance, and premature failure. MXenes properties make them ideal candidates for addressing persistent challenges in battery design, particularly in environments with corrosive electrolytes.

Although the literature on MXenes in Al electrochemistry has concentrated on their electrochemical activity, the material attributes that make MXenes attractive active materials also underpin numerous passive-component applications. First, their high electronic conductivity enables them to act as thin, conformal current-collecting layers or conductive interlayers that reduce local current density and homogenize electron transport across composite electrodes [110]. Second, the tunable surface chemistry (–O, –OH, –F terminations that can be introduced or partially exchanged by processing) provides an opportunity to tailor interfacial energy and chemical affinity[111]: Third, MXenes form dense, mechanically robust films by vacuum filtration or spray/coating; such films can act as barrier coatings on separators or cathodes, physically hindering the diffusion of dissolved transition-metal species while permitting anion transport through defects or engineered porosity. Fourth, MXenes are capable of adsorbing chalcogen/polyselenide species through surface interactions or electrostatic attraction, which can suppress shuttle phenomena and reduce active-material loss when used as a coating or interlayer[54], [112].

7.1.1 Electronic Conductivity

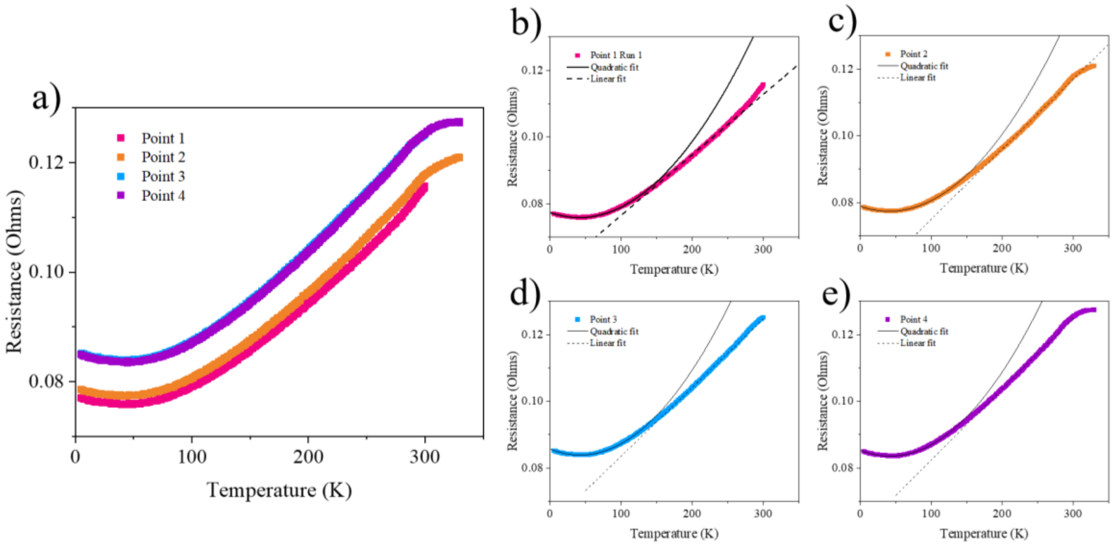

Figure 7.1 Electrical characterisation of $Ti_3C_2T_X$ using the Four-Probe Method. a) collected resistance data across the sample area, b)-e) fitted curves from four individual measurements

The electronic conductivity of $Ti_3C_2T_X$ is measured using a PPMS with a four-probe configuration. The results are presented in Figure 7.1, which shows two resistance vs. temperature curves obtained from different regions of the same film.

The vertical displacement between the curves is attributed to local thickness variations, a common feature of tape-cast films. However, the consistency in curve shape confirms that the intrinsic electronic transport properties are uniform across the sample, with differences in magnitude arising from geometry rather than material quality. The temperature-dependent conductivity data were fitted using two distinct models: a quadratic model for the low-temperature region and a linear model for the intermediate-temperature region. The corresponding fitting parameters are summarized in Table 7.1.

Table 7.1 Summary of fitted parameters for the four-probe curves.

	Point 1	Point 2	Point 3	Point 4
		Quadratic $\mathbf{R = A_{quad} + B_{quad}T + C_{quad}T^2}$		$\mathbf{(eq. 7.1)}$
$\mathbf{A}_{quad}$	0.07738	0.07891	0.08570	0.08532
$\mathbf{A}_{quad}$ std.err	2.3×10^{-5}	2.1×10^{-5}	4.0×10^{-5}	2.2×10^{-5}
$\mathbf{B}_{quad}$	-7.42×10^{-5}	-7.41×10^{-5}	-8.6×10^{-5}	-8.42×10^{-5}
$\mathbf{B}_{quad}$ std err	8.6×10^{-7}	7.5×10^{-7}	1.6×10^{-6}	9.2×10^{-7}
$\mathbf{C}_{quad}$	9.05×10^{-7}	9.12×10^{-7}	1.02×10^{-6}	1.010×10^{-6}
$\mathbf{C}_{quad}$ std err	6.9×10^{-9}	5.8×10^{-9}	1.4×10^{-8}	8.0×10^{-9}
R^2	0.998	0.998	0.994	0.997
		Linear $\mathbf{R=A_{lin}+B_{lin}T}$		$\mathbf{(eq. 7.2)}$
$\mathbf{A}_{lin}$	0.05839	0.0540	0.0629	0.0612
$\mathbf{A}_{lin}$ std err	1.0×10^{-17}	1.9×10^{-4}	1.1×10^{-4}	1.5×10^{-4}
$\mathbf{B}_{lin}$	1.81513×10^{-4}	2.101×10^{-4}	2.061×10^{-4}	2.123×10^{-4}
$\mathbf{B}_{lin}$ std err	4.6×10^{-20}	8.0×10^{-7}	5.0×10^{-7}	6.6×10^{-7}
R^2	1	0.998	0.999	0.999

7.1.1.1 Data treatment and uniformity

To minimize rounding errors, the raw resistance data were fitted directly before converting to sheet resistance (R_S) using the standard conversion factor for a linear four-probe array [107].

$$C = \frac{\pi}{\ln(2)} \approx 4.532 \qquad \text{(Eq. 7.3)}$$

$$R_S = C \cdot R \qquad \text{(Eq. 7.4)}$$

Sheet resistance is independent of thickness and is a fundamental metric for evaluating thin films. The coefficients from the linear and quadratic fits are summarized in Table 7.2.

The data show that the shape-defining coefficients (B and C) have significantly lower standard deviation than the magnitude-defining coefficient (A). This confirms the homogeneity of the material's intrinsic electronic properties, despite flake stacking and thickness variations.

Table 7.2 Summary of sheet resistance parameters for the four-probe curves.

	Point 1	Point 2	Point 3	Point 4	Average	Standard deviation
			Quadratic $\mathbf{R=A_{s,quad}+B_{s,quad}T+C_{s,quad}T^2}$			**(Eq. 7.5)**
$\mathbf{A}_{s,quad}$	0.35069	0.35762	0.38839	0.38667	0.37084	0.01688
$\mathbf{B}_{s,quad}$	-3.4×10^{-4}	-3.4×10^{-4}	-3.9×10^{-4}	-3.8×10^{-4}	-3.6×10^{-4}	2.55×10^{-5}
$\mathbf{C}_{s,quad}$	4.1×10^{-6}	4.1×10^{-6}	4.6×10^{-6}	4.6×10^{-6}	4.4×10^{-6}	2.5×10^{-7}
			Linear $\mathbf{R=A_{s,lin}+B_{s,lin}T}$			**(Eq. 7.6)**
$\mathbf{A}_{s,lin}$	0.264623	0.2449	0.2853	0.2775	0.2681	0.0153
$\mathbf{B}_{s,lin}$	8.23×10^{-4}	9.52×10^{-4}	9.34×10^{-4}	9.62×10^{-4}	9.18×10^{-4}	5.59×10^{-5}

7.1.1.2 Low temperature electronic transport

In the low-temperature regime (2 K to ~150 K), the resistance exhibits a quadratic temperature dependence (Eq. (7.5), characteristic of a Fermi liquid, where electron–electron interactions dominate scattering.

$A_{s,quad}$: represents the residual resistivity, also known as ρ_0, represents the resistance at absolute zero, caused by static impurities and lattice defects.

It is often difficult to find published data on the residual resistivity of metals. Instead, the ratio of resistivity at room temperature (ρ_{RT}) to that at low temperature, typically 4.2 K $\rho_{4.2}$, is more commonly reported.

$$\frac{\rho_{4.2}}{\rho_{RT}}=\frac{R_{4.2}}{R_{RT}} \qquad \text{(Eq. 7.7)}$$

This ratio is valid within 1%, making it a robust metric for comparison. [108] The obtained values for $Ti_3C_2T_X$ are reported in Table 7.3. A low value for the ratio indicates a high-purity, low defect material, as seen in metals like 99.999% indium or Al [109], which have a ratio less than 1×01^{-4}. A higher ratio suggests a more impure or defective material. Therefore, the high value for $Ti_3C_2T_X$ indicates a high density of defects, consistent with the presence of surface termination groups (T_X) in MXenes, which introduce static scattering centres.

Table 7.3 Resistance and ratio for $Ti_3C_2T_X$

	Point 1	Point 2	Point 3	Point 4
$\boldsymbol{R_{4.2}}$	3.49×10^{-1}	3.56×10^{-1}	3.87×10^{-1}	3.85×10^{-1}
$\boldsymbol{R_{RT}}$	5.21×10^{-1}	5.33×10^{-1}	5.66×10^{-1}	5.67×10^{-1}
$\boldsymbol{\frac{R_{4.2}}{R_{RT}}}$	6.71×10^{-1}	6.69×10^{-1}	6.83×10^{-1}	6.79×10^{-1}

$B_{s,quad}$: linear coefficient, is typically associated with electron–phonon scattering. In most metals, this coefficient is positive, reflecting increased resistance with temperature [110]. However, a negative linear coefficient, as observed for the $Ti_3C_2T_X$ sample, suggests a disordered system where the mean free path of electrons approaches the interatomic spacing, a condition known as the Mott–Ioffe–Regel limit. This behaviour is common in amorphous metals, defective carbon materials [111], and some alloys [112], and indicates a breakdown of conventional transport models.

$C_{s,quad}$: fermi liquid coefficient, represents the strength of electron–electron scattering. A larger value implies stronger interactions and may indicate proximity to a quantum critical point. Its presence confirms that $Ti_3C_2T_X$ behaves as a conventional metal in this regime [113].

7.1.1.3 Linear resistance

Above ~150 K, the resistance becomes linear with temperature, a hallmark of non-Fermi liquid behaviour. This crossover suggests a shift in the dominant scattering mechanism. The linear fit (Eq. 7.6) can be related to the temperature coefficient of resistivity (α) using:

$$R_s(T) = R_{ref}\left[1 + \alpha\left(T - T_{ref}\right)\right] \qquad \text{(Eq. 7.8)}$$

$$\alpha = \frac{\mathrm{B_{s,lin}}}{\mathrm{A_{s,lin}}} \qquad \text{(Eq. 7.9)}$$

The averaged linear fit coefficients and α are presented in Table 7.4

Table 7.4 Averaged linear fit coefficients and α

	Point 1	Point 2	Point 3	Point 4	Average
$\mathbf{A}_{s,lin}$	0.264623	0.2449	0.2853	0.2775	0.2681
$\mathbf{B}_{s,lin}$	8.23×10^{-4}	9.52×10^{-4}	9.34×10^{-4}	9.62×10^{-4}	9.18×10^{-4}
α	3.11×10^{-3}	3.89×10^{-3}	3.27×10^{-3}	3.47×10^{-3}	3.42×10^{-3}

The value observed α $Ti_3C_2T_X$ is remarkably similar to that of conventional noble metals such as silver (≈ 3.8×10^{-3} K^{-1}), copper (≈ 3.9×10^{-3} K^{-1}), and gold (≈ 3.4×10^{-3} K^{-1}) [114].

This finding suggests that despite the high defect density and complex scattering mechanism at low temperatures, the dominant electron-phonon scattering mechanism at higher temperature is comparable to that of conventional conductors, highlighting the excellent electronic properties of the $Ti_3C_2T_X$ film.

7.1.2 Structural Properties and Composition

Raman spectroscopy is used to investigate the structural features $Ti_3C_2T_X$.The spectrum in Figure 7.2 reveals D band (~1400 cm^{-1}) and G band (~1563 cm^{-1}), characteristic of graphitic and disordered carbon. The calculated I_D/I_G ratio of 0.78 indicates moderate disorder, consistent with MXenes morphology.

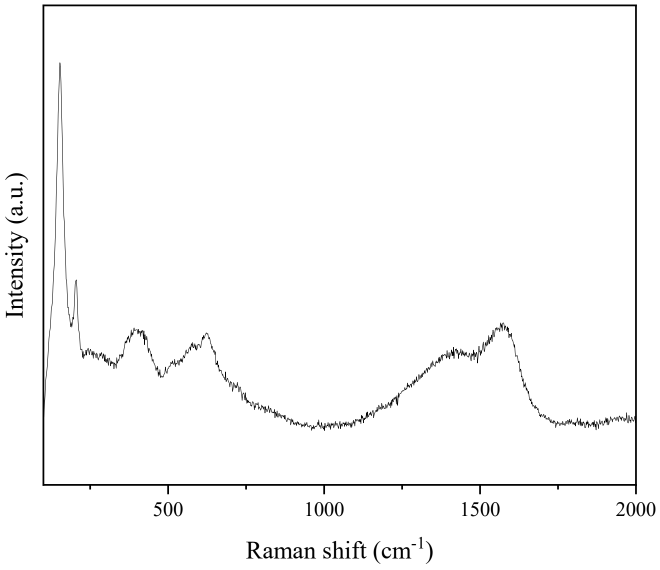

Figure 7.2 Structural characterisation of the pristine $Ti_3C_2T_X$: Raman spectra of $Ti_3C_2T_X$

In addition to the carbon features, a sharp and strong peak observed at 154 cm^{-1} is associated with the oxidation of the $Ti_3C_2T_X$ and formation of Ti_3C_2, as presented in the literature. The bands at 402 and 620 cm^{-1} are attributed to Ti and Al oscillation from the remaining MAX phases [115].

Finally, the band observed at 203 cm^{-1} is attributed to the out-of-plane vibrations of Ti-C bonds. This band was also reported in literature [116] the slight shift in the peak position may be attributed to differences in synthesis conditions or morphology

The results confirm the successful synthesis of $Ti_3C_2T_X$ MXenes with characteristic vibrational modes and structural features consistent with reported data.

7.1.3 Electronic Structure

To investigate the electronic structure and oxidation state of titanium in the pristine $Ti_3C_2T_X$, XAS was performed at the Ti K-edge. The resulting spectrum, shown in Figure 7.3 provides valuable insights into the chemical environment of titanium (Ti) within the $Ti_3C_2T_X$ structure.

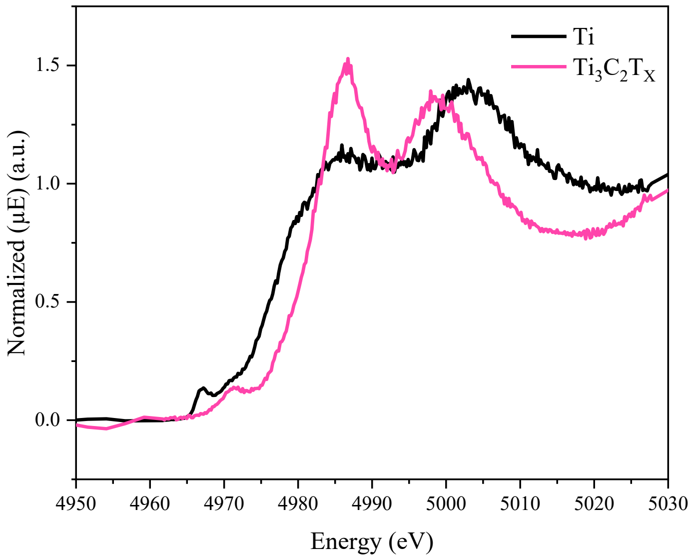

Figure 7.3 Structural characterisation of the pristine $Ti_3C_2T_X$: XAS Ti K edge

The absorption edge of $Ti_3C_2T_X$ is positioned at a higher energy than that of metallic titanium Ti(0), indicating that Ti exists in a positive oxidation state. This shift is consistent with the presence of surface termination groups (T_X) such as hydroxyl (–OH), oxygen (–O), or fluorine (–F), which are known to modify the electronic environment of titanium atoms. These findings align with previous reports on $Ti_3C_2T_X$ [117].

Additionally, features in the pre-edge region confirm the presence of Ti–C bonds. According to literature, these pre-edge features arise from excitations into C 2p–Ti 3d hybridized molecular orbitals [118], further validating the structural integrity and bonding characteristics of $Ti_3C_2T_X$.

7.1.4 Remarks on the Physicochemical and Structural Characterisation of Pristine $Ti_3C_2T_X$

A comprehensive understanding of $Ti_3C_2T_X$ MXenes is established by multiple characterisation techniques. The PPMS analysis revealed high electronic conductivity and a temperature-dependent resistivity profile that transitions from Fermi liquid behaviour at low temperatures to non-Fermi liquid behaviour at higher temperatures. A was found to be comparable to that of noble metals, highlighting the excellent electronic transport properties of the $Ti_3C_2T_X$ film. Raman spectroscopy confirms the presence of characteristic D and G bands, along with low-frequency vibrations associated with Ti–C bonding and residual MAX phase components. These features validate the structural composition and degree of disorder in the material. XAS at the Ti K-edge provides direct evidence of titanium's oxidation state and bonding environment, confirming the presence of surface terminations and Ti–C hybridisation.

Together, these results confirm the successful synthesis of a structurally and electronically well-defined $Ti_3C_2T_X$, suitable for further electrochemical investigation. The material's high conductivity, robust structure, and tuneable surface chemistry make it an ideal candidate for multifunctional passive roles in RABs.

These findings lay the groundwork for the next sections, where $Ti_3C_2T_X$ is evaluated in two distinct applications: as a current collector, and an additive in modified separators.

7.2 $Ti_3C_2T_X$ MXenes as Current Collectors

Section 3.4.1 outlined the key criteria for an effective current collector, including high electronic conductivity, low density, ease of processing, and chemical stability in contact with the electrolyte. In this context, MXenes offer a distinct advantage due to their exceptional processability. Once synthesized, $Ti_3C_2T_X$ can be easily applied via tape casting onto Celgard, followed by room-temperature drying and simple delamination an approach far less energy-intensive than conventional metal processing or electrospun carbon fibre fabrication.

7.2.1 Electrochemical Stability

The current collector plays a vital role in battery electrodes by providing mechanical support, electronic conductivity, and structural integrity. In the case of RABs, the primary challenge lies in the corrosive nature of the chloroaluminate IL-based electrolyte.

To assess the electrochemical stability of $Ti_3C_2T_X$ in this harsh environment, cells were assembled without active material, using various current collectors. LSV is employed to evaluate their stability.

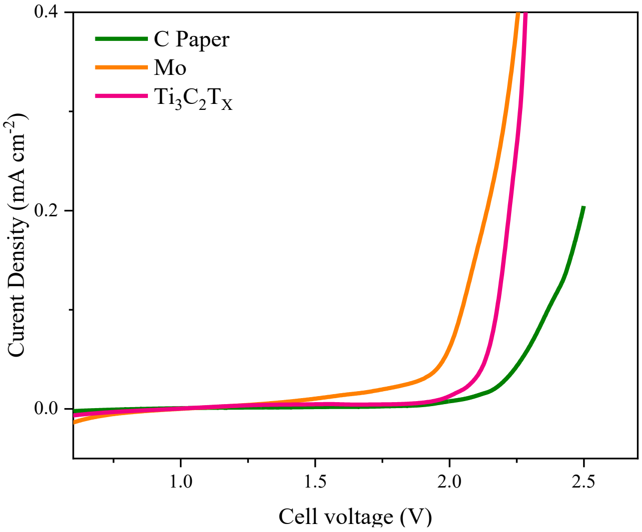

Figure 7.4 Electrochemical stability of current collectors: LSV of C paper, Mo and $Ti_3C_2T_X$

As shown in Figure 7.4, C Paper exhibits the highest electrochemical stability, with no significant current increase within the tested voltage range. $Ti_3C_2T_X$ presents an onset of anodic current occurring around 2.0 V, substantially higher than Mo, which begins to corrode at approximately 1.5 V. These results highlight $Ti_3C_2T_X$ as a stable and promising candidate for current collector applications in RABs.

To further investigate electrochemical behaviour beyond the first oxidation, CV was conducted. Figure 7.5 compares the CV profiles of C Paper, Mo, and $Ti_3C_2T_X$.

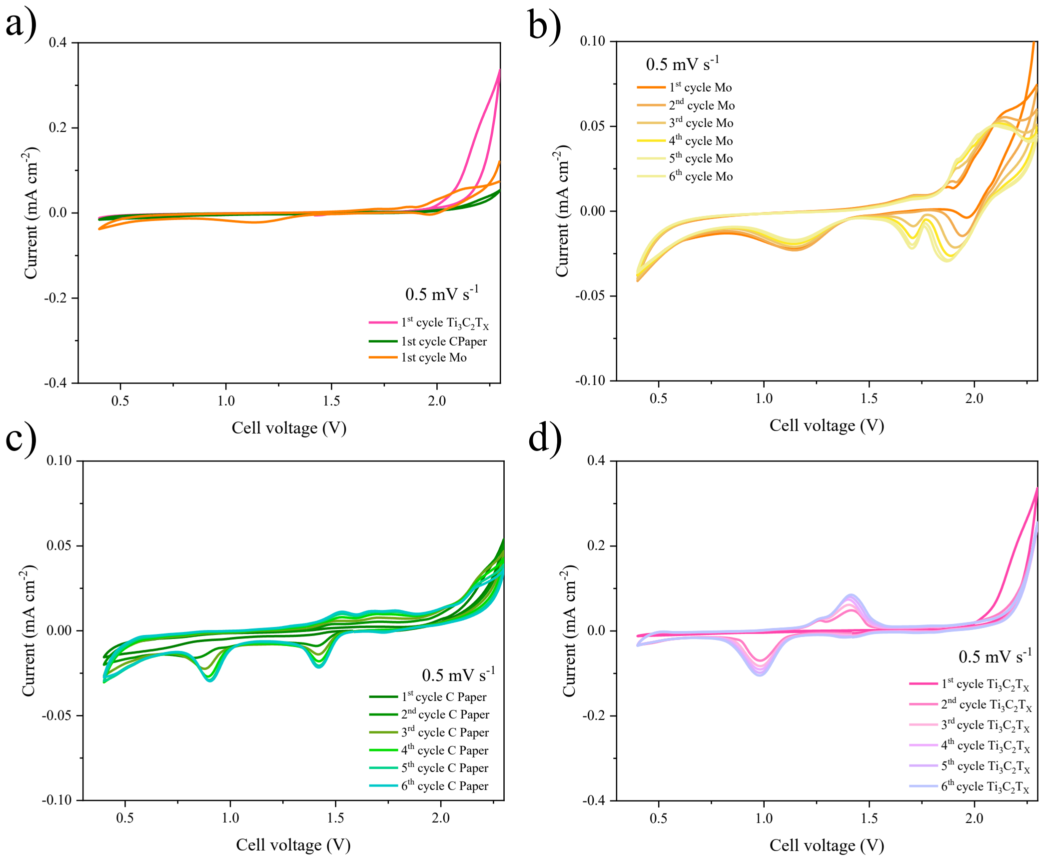

Figure 7.5 Cyclic voltammograms of different current collectors: a) 1st cycle of $Ti_3C_2T_X$ and C Paper and Mo, b)1st to 6th cycle of Mo, c)1st to 6th cycle of C Paper, d) 1st to 6th cycle of $Ti_3C_2T_X$

C Paper shows a low current response, indicating minimal electrochemical activity and charge storage This behaviour suggests that within the investigated voltage range, C Paper acts primarily as an inert conductive support with negligible faradaic contribution.

In contrast, Mo exhibits a steadily increasing current over successive cycles, suggesting ongoing electrochemical reactions. The progressive rise in current implies that Mo undergoes continuous surface activation or redox processes, contributing to its charge storage through non-stable or gradually evolving electrochemical behaviour.

$Ti_3C_2T_X$ however, presents a more complex electrochemical profile. Initially, the material appears electrochemically inactive up to approximately 2.0 V, suggesting an inert response within this lower voltage range. Upon reaching 2.2 V, a distinct peak emerges, marking the onset of an irreversible process, consistent with observations reported in the literature [119]. This irreversible reaction likely represents a voltage-triggered activation step, which facilitates the formation of a stable and reversible redox mechanism in subsequent cycles.

Following this initial activation, $Ti_3C_2T_X$ demonstrates well-defined and reversible redox peaks that persist across successive scans, indicating the establishment of a reversible electrochemical process. Such behaviour has been previously reported mainly for MXene-based composites, where it is attributed to the reversible intercalation of $AlCl_4^-$ within the layered $Ti_3C_2T_X$. Although $Ti_3C_2T_X$ exhibits significant electrochemical activity after activation, this does not compromise its structural integrity. Instead, the reversible redox reactions appear to enhance overall performance through stable charge storage contributions as reported in $Ti_3C_2T_X$ based composites.

To confirm the voltage-dependent activation, CV measurements were repeated with a cutoff voltage of 2.0 V for both $Ti_3C_2T_X$ and Mo. As shown in Figure 7.6, the current response is significantly lower compared to scans up to 2.3 V, confirming reduced electrochemical activity at lower voltages.

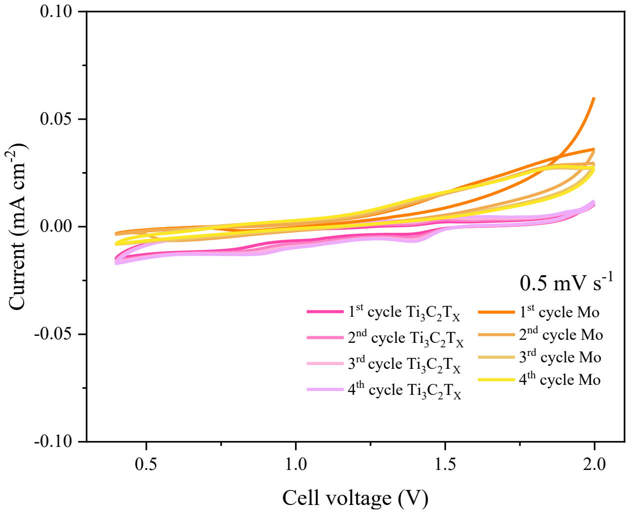

Figure 7.6 Cyclic voltammograms of $Ti_3C_2T_X$ and Mo to 2 V

To deepen the understanding of $Ti_3C_2T_X$ as a current collector in RABs, a comparative study was conducted based on the methodology of Bizot et al., who evaluated Al current collectors in LIBs. The cumulative anodic charge over the first six cycles is calculated to assess electrochemical stability. Due to the limited availability of comparable data for

RABs, $Ti_3C_2T_X$ results are benchmarked against high-purity Al foil in LIBs (as reported by Bizot [120]), as well as Mo and C Paper. The comparative data are summarized in Table 7.4 and Figure 7.7

Table 7.5 Anodic charge during the first 6 cycles of $Ti_3C_2T_X$, Mo and C paper

	$Ti_3C_2T_X$ (6 samples)		**Mo (one sample)**	**C Paper (one sample)**
cycle	**Anodic charge mean (mC cm^{-2})**	**Std. dev**	**Anodic charge (mC cm^{-2})**	**Anodic charge (mC.cm^{-2})**
1	143.0	4	86.5	29.6
2	111.0	7	68.9	34.1
3	112.0	7	62.8	35.8
4	117.0	6	58.8	36.1
5	123.0	6	56.9	35.7
6	129.1	6	56.3	35.4

The results indicate that while C Paper and molybdenum exhibit low and relatively stable anodic charge, $Ti_3C_2T_X$ shows a slightly higher and gradually increasing anodic charge. However, this behaviour remains within acceptable limits, especially when compared to Al used as a current collector in LIBs, where significantly higher anodic charge has been reported.

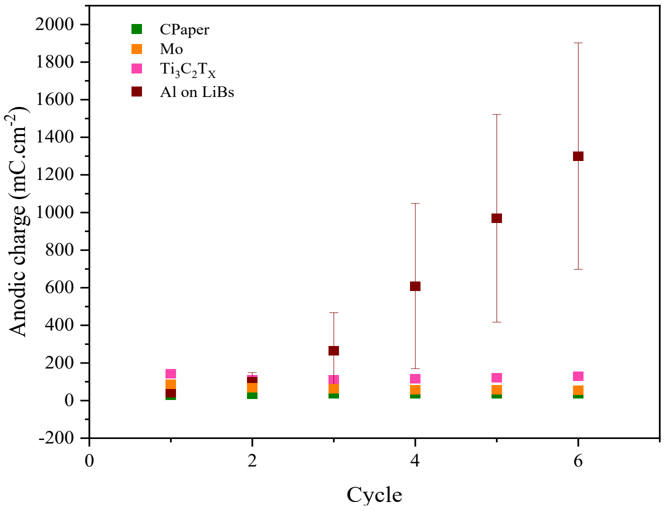

Figure 7.7 Comparison of anodic charge of different current collectors: $Ti_3C_2T_X$, high-purity Al foil in LIBs [120], Mo and C Paper.

This behaviour indicates that $Ti_3C_2T_X$ is a promising candidate for use as a current collector material, particularly in systems operating below 2.0 V, such as cobalt sulphide (Co_9S_8), which typically exhibits an operating voltage not exceeding 1.8 V [121]. The mention of $Ti_3C_2T_X$ here derives from literature reports linking cobalt dissolution and structural degradation to poor cycling stability, similarly to what we report for CoSe. To address this structural degradation, several studies have proposed protective interlayers, for example, reduced graphene oxide films or MXene nanosheets, to suppress cobalt dissolution and improve electrode integrity. In these reports, the use of MXene-based layers (such as $Ti_3C_2T_X$) notably enhanced the stability of specific for both Co_9S_8 and $CoSe_2$ electrodes [54].

Within the context of this work, $Ti_3C_2T_X$ remains electrochemically inert below 2.0 V, behaving similarly to conventional conductive substrates. However, above this threshold, it becomes electrochemically active, suggesting potential as a dual-function component capable of contributing additional capacity. Due to time constraints and the scope of this thesis, a comprehensive evaluation of $Ti_3C_2T_X$ in combination with low-voltage active materials such as Co_9S_8 was not feasible. Consequently, the characterisation of passive components (current collectors, and separators) with low-voltage electrodes will remain as future work.

Nevertheless, the preliminary findings, together with the reported performance improvements of MXene-based systems in the literature, point to a promising research direction. A dedicated study involving more stable low-voltage materials could help elucidate the charge storage mechanisms and potentially lead to the development of highly efficient and durable low-voltage RABs.

7.2.2 Dual-function current collector: Active material graphite

To further explore the dual functionality of $Ti_3C_2T_X$, graphite was selected as the active material as it is considered the standard cathode material for RABs. The morphology and electrochemical performance of graphite cathodes coated on both C Paper and $Ti_3C_2T_X$ current collectors were investigated.

7.2.2.1 Morphological characterisation

It is crucial to address two significant challenges that arise from the thin, lightweight nature of $Ti_3C_2T_X$ current collector: Coating thickness and binder compatibility. Figure 7.8 presents two preliminary coatings of graphite on $Ti_3C_2T_X$: a) with a non-water-based binder (PAN) and b) with a water-based binder (carr).

The PAN-based coating exhibited poor adhesion, likely due to unfavourable interactions with the hydrophilic surface terminations (T_X) on the $Ti_3C_2T_X$. Additionally, thick coatings lead to electrode delamination and cracking upon drying, an issue attributed to the low mechanical robustness of the thin $Ti_3C_2T_X$ layer.

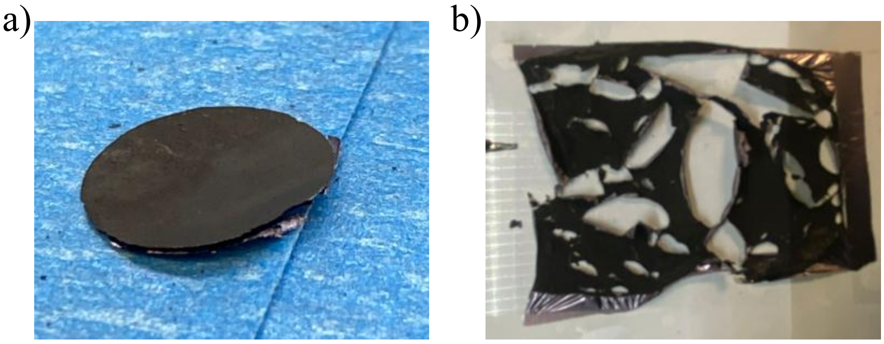

Figure 7.8 Preliminary coatings of graphite on $Ti_3C_2T_X$ with different binders: a) PAN, b) carr

To further assess these limitations, SEM images of graphite electrodes coated on $Ti_3C_2T_X$ and C Paper are shown in Figure 7.9. A clear difference in electrode thickness is observed. A clear difference in electrode thickness is observed. While thicker electrodes are not inherently indicative of higher energy density, since parameters such as mass loading, packing density, and porosity also play critical roles, this morphology can still offer advantages depending on the target application. In the case of nanostructured materials, the inherently high porosity may limit volumetric energy density but can facilitate ion transport and electrolyte accessibility, making such architectures advantageous for lightweight or high-capacity designs. This highlights the importance of balancing electrode thickness, density, and structural porosity in optimizing performance for specific energy storage goals.

Furthermore, $Ti_3C_2T_X$'s excellent wettability in water, evidenced by a contact angle of approximately 34° [122], makes it highly compatible with water-based binder systems. In contrast, metals like molybdenum exhibit much higher contact angles (~76°) [123], resulting in poorer interaction with aqueous formulations. The hydrophilic nature of $Ti_3C_2T_X$ promotes better adhesion and dispersion of water-based binders, which are increasingly favoured for their environmental benefits, lower cost, and reduced toxicity. By enabling strong interfacial bonding with these sustainable binders, $Ti_3C_2T_X$ not only improves electrode integrity but also supports the development of greener and more efficient energy storage technologies.

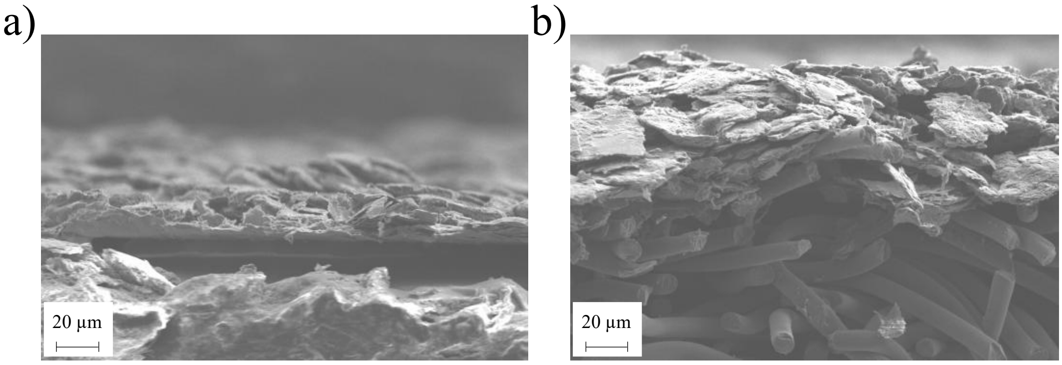

Figure 7.9 SEM image of graphite electrodes coated onto $Ti_3C_2T_X$ and C Paper current collector

7.2.2.2 Electrochemical characterisation

Figure 7.10 compares the specific capacity cycling of graphite electrodes using $Ti_3C_2T_X$ (Figure 7.10 a) and C Paper (Figure 7.10 b) as current collectors, the measurements were conducted up to 2.3 V. The $Ti_3C_2T_X$-based electrode exhibits a high initial specific capacity, primarily attributed to the high voltages anodic process of $Ti_3C_2T_X$. and additional features attributed not visible in the C Paper-based electrode, the features are attributed to the reversible processes observed in the CV.

(Figure 7.10 c) shows that After a few cycles, the capacity stabilizes, indicating a slight but stable enhancement of the specific capacity relative to the C Paper-based electrode, this suggests a synergistic interaction between $Ti_3C_2T_X$ and graphite. Nonetheless, the efficiency shows a decrease upon cycling suggesting an increasing irreversibility. If the reversible process is accepted as caused by intercalation of $AlCl_4^-$ the irreversibility could be attributed to trapped $AlCl_4^-$ on the layered material.

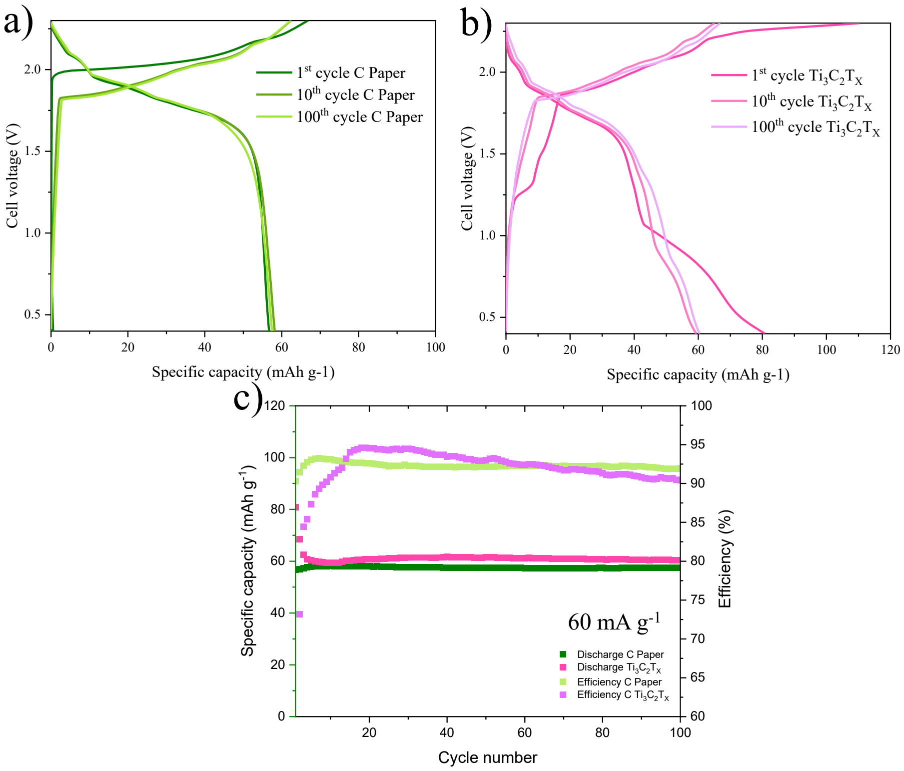

Figure 7.10 GCPL of graphite electrodes onto $Ti_3C_2T_X$ and C Paper current collector: a) 1st, 10th and 100th cycle of C Paper based electrode, b) 1st, 10th and 100th cycle of $Ti_3C_2T_X$ -based electrode, c) comparison of discharge capacity and efficiency upon cycling

7.2.3 Passive current collector and future work

Our investigation into the dual-functionality of $Ti_3C_2T_X$ as current collector has provided valuable insights. While its unique properties, such as high electronic conductivity and favourable electrochemical stability, make it a strong candidate, they also introduce fabrication challenges. Specifically, the thin nature of $Ti_3C_2T_X$ requires careful control of coating thickness, as mechanical stress from solvent evaporation can compromise the structural integrity of the electrode.

Adhesion of the slurry is notably improved when using water-based binders, likely due to the hydrophilic surface terminations (T_X groups) of $Ti_3C_2T_X$, which promote strong interfacial bonding and enhance electrode cohesion.

Electrochemical stability tests confirmed that $Ti_3C_2T_X$ performs well at voltages below 2.0 V, outperforming conventional materials like Mo. Nevertheless, above 2.0V an irreversible anodic current is observed, leading to reversible processes in the following cycles.

7.3 Separators: $Ti_3C_2T_x$ MXenes As a Tool to Reduce Shuttling of Active Material

One of the primary degradation mechanisms affecting transition metal oxides and chalcogenide cathodes in RABs is the dissolution and subsequent migration of active species to the anode. This process leads to capacity fading, electrode degradation, and reduced cycling stability, as demonstrated in Chapters 5 and 6 for CoSe. Addressing this issue is critical for improving the long-term performance of RABs.

While this section focuses on the separator's role in mitigating shuttling, it builds upon the dual functionality of $Ti_3C_2T_X$ discussed in Sections 7.2. MXenes, with their layered structure and tuneable surface chemistry, offer tailored interactions with ions and molecules. When incorporated into the separator, they can act as both physical and electrostatic barriers, suppressing the migration of dissolved metal species while maintaining efficient ion transport. Additionally, their high conductivity, maintained only on the electrode side, may promote uniform current distribution, further enhancing battery performance.

In this study, the use of $Ti_3C_2T_X$ modified separators is proposed to reduce the migration of active material, motivated by the degradation observed in CoSe cathodes. The goal is to improve cycling stability by minimizing capacity loss due to active species dissolution.

7.3.1 Optimisation of the Separator Composition

Two separator configurations were evaluated:

(i) $Ti_3C_2T_X$ separator, containing 8.6 mg of $Ti_3C_2T_X$ per separator; and

(ii) $Ti_3C_2T_X$-CNT separator, incorporating an equal mass ratio of CNTs and $Ti_3C_2T_X$ (total $Ti_3C_2T_X$ content: 4.5 mg per separator). The addition of CNTs was intended to prevent $Ti_3C_2T_X$ restacking, thereby maintaining ionic pathways for chloroaluminate species while enhancing selectivity against the migration of dissolved cathode species.

CV results for both separators are shown in. While both configurations demonstrated promising performance, the $Ti_3C_2T_X$-CNT separator exhibited lower electrochemical activity. This suggests that CNT incorporation may reduce the anodic current during the first cycle that enables reversible redox reactions previously attributed to intercalation of $AlCl_4^-$ in $Ti_3C_2T_X$ layers.

CV results for both separators are shown in Figure 7.11 a) While both configurations demonstrate promising electrochemical behaviour, the$Ti_3C_2T_X$–CNT separator exhibits lower activity compared to the $Ti_3C_2T_X$ only separator. This reduction may arise from the CNT network, which, while beneficial for maintaining porosity and ion transport, and suppress the anodic currents responsible for the reversible redox process observed in $Ti_3C_2T_X$-based electrodes.

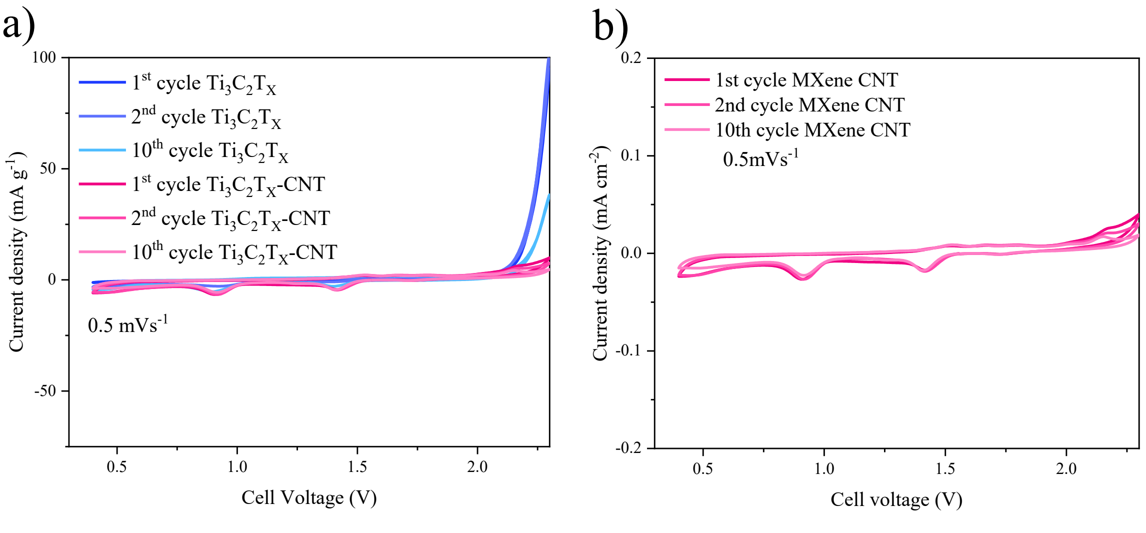

Figure 7.11 $Ti_3C_2T_X$ in modified separators: a) CV of $Ti_3C_2T_X$ and $Ti_3C_2T_X$ -CNT modified separators, b) CV of $Ti_3C_2T_X$ -CNT modified separators (aereal current density)

When the gravimetric response of the separator is converted to an areal basis (Figure 7.11 b), its electrochemical activity remains lower than that of the $Ti_3C_2T_X$ current collector Figure 7.5. Although this comparison is indirect, it reinforces the importance of optimizing MXene-based current collectors to balance high conductivity with controlled redox activity, potentially enabling dual-function electrodes that contribute to both electronic transport and additional charge storage.

7.3.2 Electrochemical performance with graphite electrodes

As standard material, graphite-carr electrodes were paired with $Ti_3C_2T_X$-CNT and conventional separator to assess the effect of $Ti_3C_2T_X$-CNT on the electrochemical performance. As shown in Figure 7.12 a), the $Ti_3C_2T_X$-CNT separator delivers as higher specific capacity during initial cycles without altering the current profiles. However, long-term cycling (Figure 7.12 b) reveals that the conventional separator maintains superior stability. This behaviour can be attributed to the conductive $Ti_3C_2T_X$-CNT layer forming a sandwich-like architecture around the cathode.

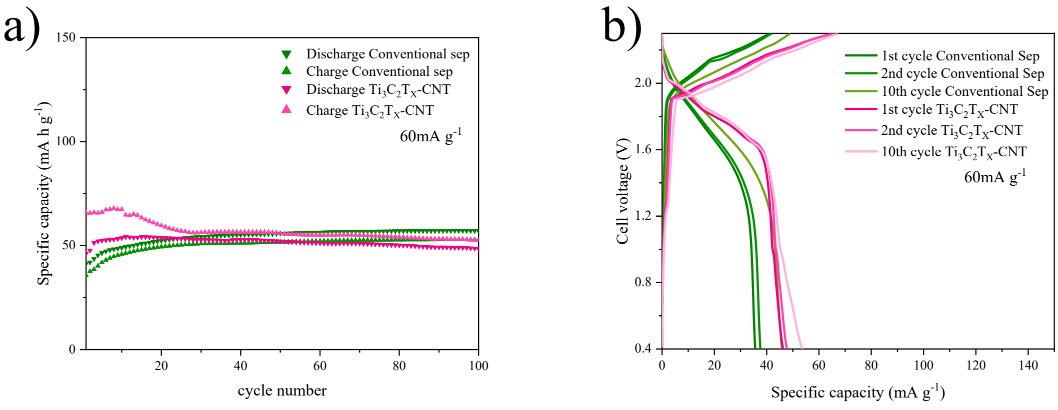

Figure 7.12 GCPL of graphite electrodes with different separators a) 1st and 10th cycles, b) long term cycling performance

Coating both sides of the electrode with a conductive interface that enhances electron transport. Similar “sandwich-structured” designs, with other conductive material have been reported to improve electronic conductivity and interfacial contact in various energy-storage systems[130], supporting the observed improvement here. Importantly, while such a configuration enhances early-cycle conductivity, the intrinsic stability of the cell remains uncompromised. It should also be emphasized that the intended purpose of MXenes in this system is not primarily to increase conductivity but to mitigate shuttle effects through their surface chemistry and adsorption capabilities. In the present graphite-based system, where no shuttle behaviour occurs, the improved performance instead highlights MXene's secondary benefit, its excellent electronic conductivity (Section 7.1.1) offering additional motivation for further research into MXene-based conductive interfaces.

7.3.3 Electrochemical performance with CoSe cathodes

In Chapters 5 and 6, the degradation mechanism was identified as the dissolution and migration of $Co(AlCl_4)_2$, which results in cobalt deposition on the anode and loss of active cathode material. To directly address this issue, $Ti_3C_2T_X$ has previously been incorporated into composite materials such as Co_9S_8 and CoSe, where it demonstrated the ability to mitigate the shuttling of dissolved cobalt species and even enable their reverse redeposition near the active particles[54].

In this section, we propose a more versatile and scalable approach. Rather than synthesizing new composite materials, we employ modified separators designed to perform the same function on a larger (cell-wide) scale, that is, to confine the cobalt species to the cathode side of the cell. $Ti_3C_2T_X$-CNT and conventional separators were paired with CoSe cathodes and compared with conventional ones.

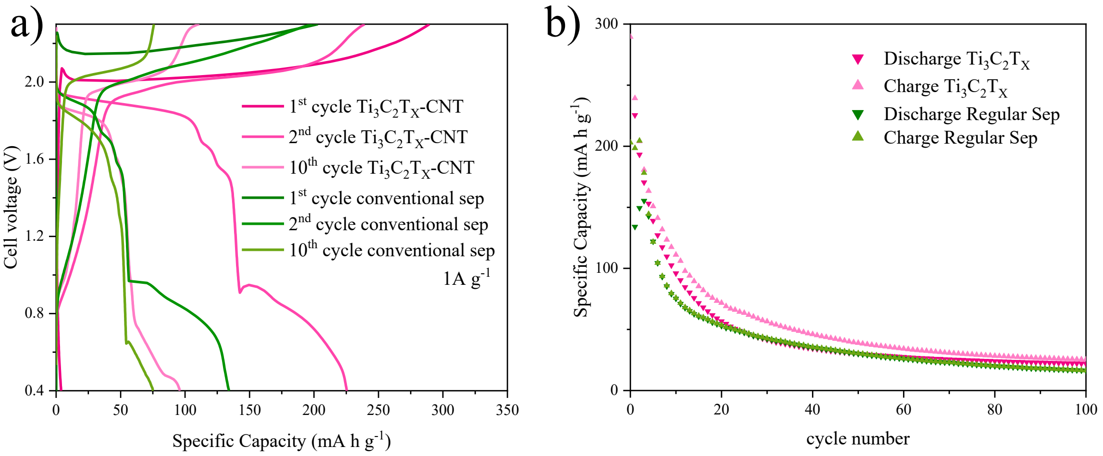

Figure 7.13 GCPL of CoSe electrodes with $Ti_3C_2T_X$ and conventional separators.

GCPL results (Figure 7.13) show a modest yet consistent improvement in both specific capacity and cycling stability when using the $Ti_3C_2T_X$-CNT separator. As demonstrated in the CV analysis, the $Ti_3C_2T_X$-CNT separator remains electrochemically inactive within the investigated voltage range and does not contribute significantly to the cathode capacity, apart from the slight increase observed during the initial cycles, which is attributed to its high electronic conductivity. The sustained improvement observed over 100 cycles is therefore ascribed primarily to the suppression of $Co(AlCl_4)_2$ shuttling, rather than to any contribution from the separator itself. This behaviour confirms that the $Ti_3C_2T_X$-CNT layer acts effectively as an electronically conductive yet electrochemically stable barrier, enhancing the long-term stability of the system

To further investigate conductivity effects, IR drop analysis from the first GCPL cycle (Figure 7.14) reveal that cells with both separators exhibited similar IR drop, indicating higher internal resistance. Although a greater difference was expected, this supports the hypothesis that $Ti_3C_2T_X$-based separators improve charge transport and structural integrity, particularly for materials prone to degradation.

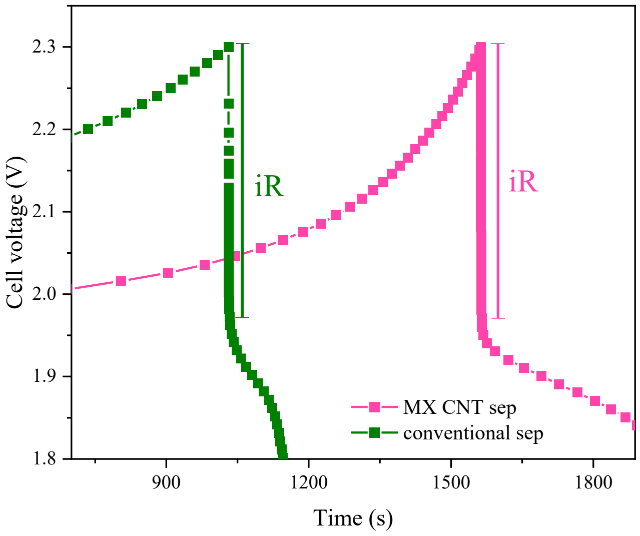

Figure 7.14 IR drop comparison of CoSe electrodes with $Ti_3C_2T_X$-CNT and conventional separator.

Finally, to evaluate the effectiveness of the $Ti_3C_2T_X$–CNT separator in mitigating cobalt shuttling, post-mortem SEM-EDX analysis was performed on the Al anode after 10 cycles. As shown in Figure 7.15, cobalt was detected on the anode surface, confirming that migration of active material from the cathode to the anode is not fully suppressed. This observation indicates that, although the $Ti_3C_2T_X$ modified separator reduces cobalt shuttling to some extent, it does not completely eliminate it.

A possible explanation is that the MXene component, being confined to the separator rather than integrated within the cathode, may capture migrating cobalt species but cannot facilitate their return to the active cathode for reintegration. Consequently, the proposed separator design only partially mitigates the dissolution-driven degradation pathway identified in earlier chapters. These results highlight the need for further optimisation, potentially through integrated electrode, separator heterostructures to more effectively confine and recover cobalt species within the cathode region.

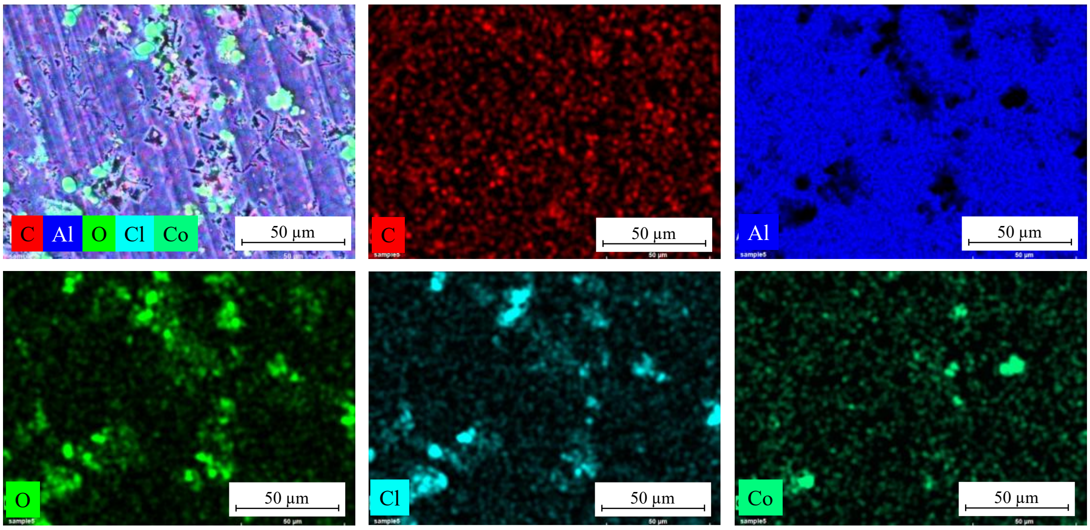

Figure 7.15 SEM-EDX of Al anode after 20 cycles of cycling with CoSe cathode and $Ti_3C_2T_X$-CNT separator

Therefore, the hypothesis that $Ti_3C_2T_X$ -based separators can effectively prevent Co shuttling remains unvalidated. Nonetheless, the observed partial mitigation and improved conductivity highlight the potential of this approach. Future work should explore more advanced separator architectures and composite cathode designs that can better retain active species while maintaining ion transport efficiency.

7.3.4 Remarks and Future Work

The preliminary investigations into $Ti_3C_2T_X$ -modified separators aimed to address the parasitic degradation pathway identified in earlier chapters, specifically, the dissolution and shuttling of cobalt species from the cathode to the Al anode. While the incorporation of $Ti_3C_2T_X$-based layers into the separator showed slight improvements in specific capacity and cycling stability, the results do not conclusively validate the hypothesis that $Ti_3C_2T_X$ can effectively suppress the shuttling mechanism.

Indeed, while the $Ti_3C_2T_X$ layer may reduce the extent of Co migration, it does not eliminate it. Moreover, attempts to increase the barrier effect such as by densifying the $Ti_3C_2T_X$ layer could inadvertently hinder chloroaluminate ion diffusion, compromising overall battery performance. This trade-off highlights the complexity of designing multifunctional separator systems and underscores the need for further optimisation.

Despite these limitations, the findings offer valuable insights and suggest several promising directions for future work:

- Development of composite cathodes that integrate MXenes with active materials to retain dissolved species within the cathode structure and reduce capacity loss.
- Advanced separator designs that block transition metal migration.
- Post-mortem analyses of electrodes and separators to better understand interfacial interactions and material retention mechanisms.

This work also serves to close the loop between the degradation mechanisms discussed in Chapters 5 and 6 and the mitigation strategies explored in Chapter 7. Although the intended goal of suppressing shuttling was not achieved, the approach remains a compelling avenue for future research. With further refinement, $Ti_3C_2T_X$-based components may contribute to the development of more stable and efficient cathodes for RABs.

8 Conclusions

This dissertation directly addresses critical mechanistic discrepancies in the understanding of transition metal chalcogenides as cathodes for RABs. Through a comprehensive, real-time investigation using advanced *in situ* and *operando* synchrotron-based X-ray techniques, this work offers unprecedented insight into the electrochemical transformations of CoSe.

The primary charge storage process is governed by an initial irreversible transformation from hexagonal CoSe to cubic $CoSe_2$ and amorphisation of CoSe, within the amorphous lattice, Se is oxidized from Se^{2-} to Se^{1-} during charge, and reduced back to Se^{2-}during discharge while Co remains electrochemically inactive.

$$6CoSe + 6AlCl_4^- \longrightarrow 3CoSe_2 + 3Co(AlCl_4)_2 + 6e^-$$

$$Se^{2-} \rightleftarrows (Se_2)^{-2} + 2e^-$$

The initial phase transition and amorphisation is essential for enabling reversible capacity but also initiates structural disorder and degradation and is accompanied by the dissolution of $Co(AlCl_4)_2$, which migrates through the electrolyte and deposits on the Al anode. This shuttling mechanism leads to the loss of active material and anode contamination, contributing to capacity fade.

To address this challenge, the second part of this work explored the multifunctional role of $Ti_3C_2T_X$ MXenes as a passive and active component in RABs. $Ti_3C_2T_X$'s high conductivity, chemical stability, and water processability make it a promising candidate for use as a current collector, and separator additive. These investigations were directly motivated by the degradation mechanisms uncovered in the CoSe study, forming a tightly connected research arc.

As a dual-function current collector, $Ti_3C_2T_X$ not only facilitates charge transport but also presents irreversible anodic process, particularly at voltages above 2.0 V that triggers reversible processes that contribute to the specific capacity. Its performance is most promising in low-voltage systems. As a separator additive, the electrochemical activity of $Ti_3C_2T_X$ -CNT does not interfere with the active material and show slight reduction in cobalt shuttling and improved initial specific capacity. However, cobalt is still detected on the anode post-cycling, indicating that the shuttling suppression hypothesis cannot be validated.

Together, these findings form a cohesive narrative: the mechanistic insights into CoSe degradation informed the design and evaluation of $Ti_3C_2T_X$ -based components, which in turn provided valuable feedback on the limitations and opportunities for material engineering in RABs. This integrated approach highlights the importance of understanding both electrochemical mechanisms and component interactions to advance battery performance.

Future Directions

Building on this foundation, future research should focus on:

- Composite cathode architectures that integrate $Ti_3C_2T_X$ to retain active species and reduce dissolution of active material.
- Advanced separator designs that block transition metal migration.
- Multimodal characterisation strategies to capture dynamic transformations and interfacial phenomena in real time.
- Environmentally sustainable processing and disposal protocols, particularly for corrosive chloroaluminate electrolytes.

This work contributes both fundamental mechanistic insight and practical engineering strategies toward the development of more stable, efficient, and sustainable RABs. It lays the groundwork for future innovations in multivalent batteries and multifunctional material design.

9 Appendix

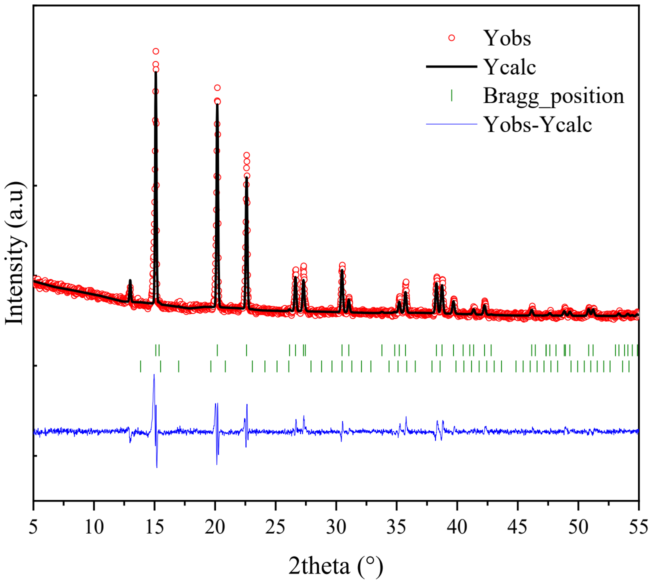

Figure A1 Refinement of CoSe considering $CoSe_2$ phase

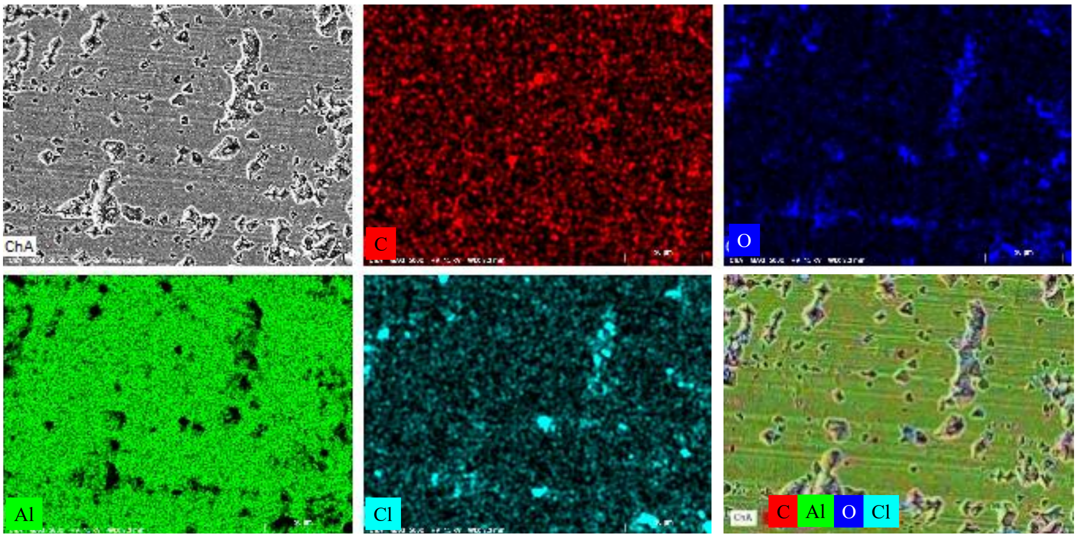

Figure A2 Effect of cathode degradation on the anode: SEM-EDX analysis of Al foil after 5 cycles.

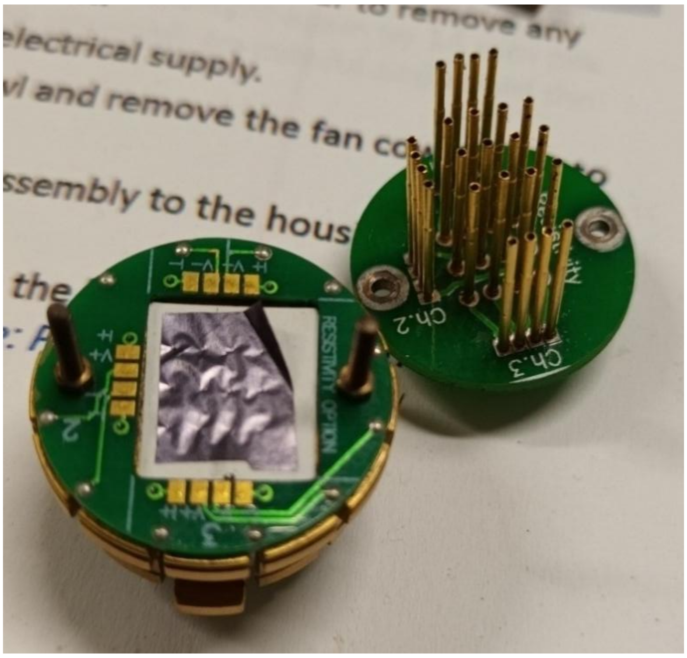

Figure A3 Four probes montage (Wimbush press assembly)

Table A1 Anodic charge during the first 6 cycles of Al (for LIBs) [120]

cycle	**Anodic charge mean (mC cm^{-2})**	**Std. dev**
1	42	15
2	100	49
3	266	201
4	609	436
5	969	552
6	1300	602

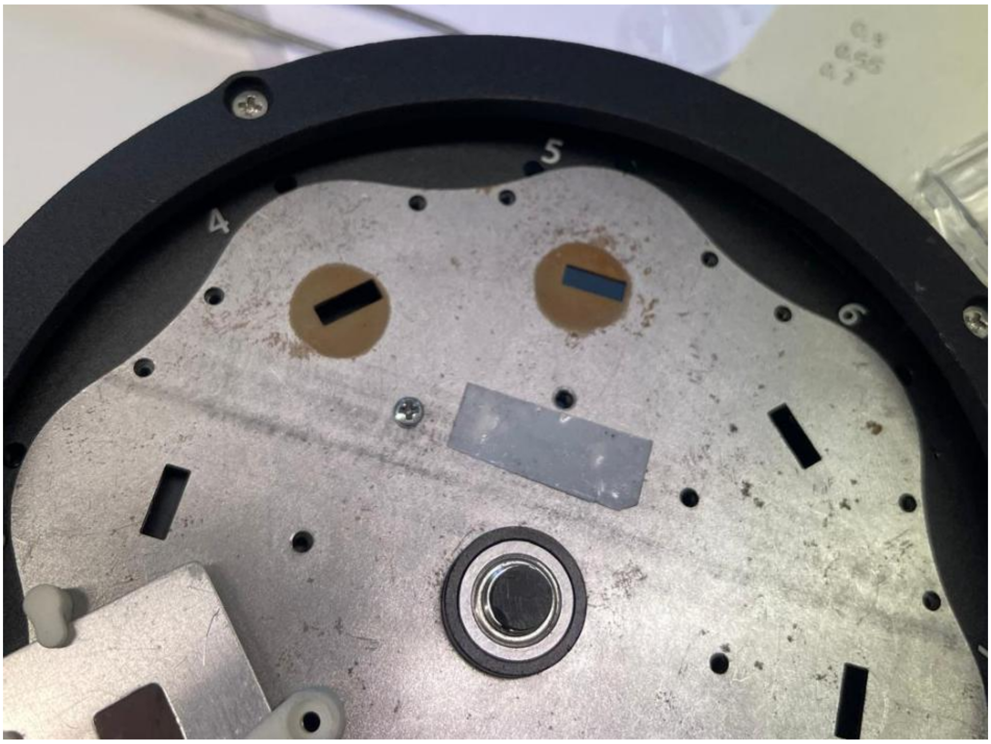

Figure A4 Corrosion of XAS sample holder by contact with *ex situ* electrodes

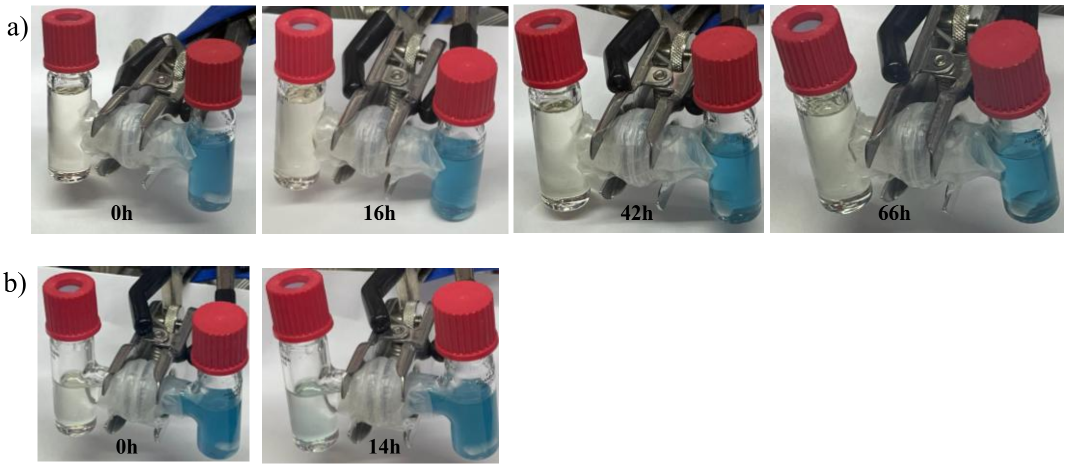

Figure A5 Co diffusion through separator a) modified with $Ti_3C_2T_X$ b) conventional separator

10 Contributions of Authorship

The content of Chapter 3 is based on the author's prior published work. A significant portion of this chapter was adapted, further discussed or synthesized from the following peer-reviewed review article:

E. Fuentes-Mendoza, M. Talari, E. Zemliánushin, R. Córdoba, N. Sabi, S. Dsoke, "Navigating the Challenges of Rechargeable Aluminum Battery Research: Material Instabilities, Technical Hurdles, and Future Directions" ChemElectroChem, 2025, 10.1002/celc.202400705.

The authors contributed to this work as follows: Mahla Talari focused on the electrolyte; Eliana Fuentes-Mendoza (the author of this thesis) and Rafael Cordoba worked on the positive electrode; and Eugen Zemliánushin handled the negative electrode, current collector, and binders. Sonia Dsoke supervised the overall work. The technical challenges were addressed collaboratively by all authors, based on individual experience. All authors contributed to conceiving the review, writing, and editing. As the lead author, Eliana Fuentes-Mendoza was responsible for the primary writing, literature review, and synthesis of the content presented in the original article.

The content of Chapters 5 and 6 are under preparation for publication with the title "Operando and *in situ* Insights into Cobalt Selenide Cathodes for Rechargeable Aluminum Batteries: Conversion Mechanism, Degradation Pathways and Electrolyte Interactions"

This dissertation was conducted by the author under the guidance and conceptual support of Prof. Sonia Dsoke (Albert-Ludwigs University, Freiburg), Dr. Fabian Jeschull (Karlsruhe Institute of Technology, KIT), and Prof. Helmut Ehrenberg (KIT). The author carried out the synthesis of CoSe, fabrication of electrodes and separators, electrolyte preparation, and cell assembly, with support from Amirhossein Dorosti. The $Ti_3C_2T_x$ material was provided by the Drexel Nanomaterials Institute. The self-standing current collector was prepared by the author under the supervision of Sokhna Dieng (Drexel

University) during a collaborative research stay in Prof. Yury Gogotsi's group. The initial goal of this collaboration was to evaluate the use of $Ti_3C_2Cl_2$ as an electrode material for RABs. However, due to the limited viability of this approach, the focus shifted toward the development and partial execution of the chapter on passive components.

SEM imaging was conducted by Dennis Triller. PPMS measurements were performed by Dr. Björn Schwarz (KIT). XAS measurements were carried out by and analysed with the assistance of Dr. Ramon Zimmermans (KIT). TGA measurements were performed by Liuda Mereacre (KIT), and ICP-OES analysis was conducted by Dr. Thomas Bergfeldt (KIT). Synchrotron XAS and SRD patterns were recorded by Dr. Angelina Sarapulova (Albert-Ludwigs University), at DESY, beamlines P65 and P01.2 with the collaboration of Dr. Volodymyr Baran and Dr. Edmund Welter. The interpretation of the synchrotron data was carried out by the author in collaboration with Dr. Angelina Sarapulova, Dr. Ramon Zimmermans, Dr. Fabian Jeschull and Dr. Nicholas Jobbitt.

During the preparation of this work, the author utilized AI-based writing assistants, including Copilot, Gemini, and ChatGPT, to support the writing process. All content generated with the assistance of these tools was carefully reviewed, edited, and verified by the author, who assumes full responsibility for the final content presented in this dissertation.

11 Scientific contributions

11.1 Publication

E. Fuentes-Mendoza, M. Talari, E. Zemliánushin, R. Córdoba, N. Sabi, S. Dsoke, "Navigating the Challenges of Rechargeable Aluminum Battery Research: Material Instabilities, Technical Hurdles, and Future Directions" ChemElectroChem, 2025, 10.1002/celc.202400705.

11.2 Conference contributions

Eliana Fuentes-Mendoza, Angelina Sarapulova, Ramon Zimmerman, Amirhossein Dorosti, Fabian Jeschull, Sonia Dsoke, Unveiling the charge storage and degradation mechanism of CoSe Based Material as Positive Electrodes for Aluminum Batteries, International Conference, Valencia (Spain), Materials for sustainable development conference 2025, oral presentation.

Eliana Fuentes-Mendoza, Angelina Sarapulova, Ramon Zimmerman, Amirhossein Dorosti, Fabian Jeschull[1], Sonia Dsoke, Unveiling the charge storage and degradation mechanism of CoSe Based Material as Positive Electrodes for Aluminum Batteries, International Conference, Mainz (Germany), 76th Annual Meeting of the International Society of Electrochemistry 2025, oral presentation.

Eliana Fuentes-Mendoza, Angelina Sarapulova, Ramon Zimmerman, Amirhossein Dorosti, Fabian Jeschull[1], Sonia Dsoke, Unveiling the charge storage and degradation mechanism of CoSe Based Material as Positive Electrodes for Aluminum Batteries, POLiS Conclave meeting, Karlsruhe (Germany) 2025, oral presentation.

Eliana Fuentes Mendoza, Ruocun (John) Wang, Teng Zhang, Fabian Jeschull, Yury Gogotsi, Sonia Dsoke, Chlorine-Terminated Titanium Carbide (MXenes) as Positive Electrodes for Aluminum Batteries, International Conference, Hong Kong (China), International Meeting on Lithium batteries (IMLB) 2024, poster presentation.

Eliana Fuentes Mendoza, Ruocun (John) Wang, Teng Zhang, Fabian Jeschull, Yury Gogotsi, Sonia Dsoke, Chlorine-Terminated Titanium Carbide (MXenes) as Positive Electrodes for Aluminum Batteries, BACCARA Power Day, Munster (Germany) 2024, oral and poster presentation

Eliana Fuentes Mendoza, Noha Sabi, Rafael Cordoba, Sonia Dsoke CoSe\C- Based Materials as Positive Electrodes for Aluminum Batteries , International Conference, Lyon (France), 74th Annual Meeting of the International Society of Electrochemistry 2023, poster presentation.

References

[1] Igor Zolnerkevic, “The behavior of blackouts,” *Revista Pesquisa Fapesp*, 2017. Accessed: Jun. 25, 2025. [Online]. Available: https://revistapesquisa.fapesp.br/en/the-behavior-of-blackouts/

[2] European Union, *Treaty on the Functioning of the European Union*. OPOCE, 2017.

[3] International Energy Agency, “Renewables 2023,” 2024. [Online]. Available: www.iea.org

[4] A. K. Barik, D. C. Das, A. Latif, S. M. Suhail Hussain, and T. S. Ustun, “Optimal voltage–frequency regulation in distributed sustainable energy-based hybrid microgrids with integrated resource planning,” *Energies (Basel)*, vol. 14, no. 2735, 2021, doi: 10.3390/en14102735.

[5] F. Schomburg *et al.*, “Lithium-ion battery cell formation: status and future directions towards a knowledge-based process design,” Feb. 13, 2024, *Royal Society of Chemistry*. doi: 10.1039/d3ee03559j.

[6] A. Ponrouch and M. Rosa Palacín, “Post-Li batteries: Promises and challenges,” Aug. 26, 2019, *Royal Society Publishing*. doi: 10.1098/rsta.2018.0297.

[7] A. Ponrouch, J. Bitenc, R. Dominko, N. Lindahl, P. Johansson, and M. R. Palacin, “Multivalent rechargeable batteries,” Jul. 01, 2019, *Elsevier B.V.* doi: 10.1016/j.ensm.2019.04.012.

[8] M. R. Palacin *et al.*, “Roadmap on multivalent batteries,” Jul. 01, 2024, *Institute of Physics*. doi: 10.1088/2515-7655/ad34fc.

[9] Cluster of Excellence POLiS, “Cluster of Excellence POLiS - Post-Lithium Storage,” https://www.postlithiumstorage.org/en/polis#:~:text=These%20so%2Dcalled%20post%2Dlithium,stationary%20and%20mobile%20electrochemical%20storage.

[10] D. Muñoz-Torrero, J. Palma, R. Marcilla, and E. Ventosa, “A critical perspective on rechargeable Al-ion battery technology,” *Dalton Trans.*, vol. 48, no. 27, pp. 9906–9911, 2019, doi: 10.1039/c9dt02132a.

[11] J. Park *et al.*, “Stable and High-Power Calcium-Ion Batteries Enabled by Calcium Intercalation into Graphite,” *Advanced Materials*, vol. 32, no. 4, p. 1904411, Jan. 2019, doi: https://doi.org/10.1002/adma.201904411.

[12] X. Li *et al.*, “Oxygen vacancy H2V3O8 nanowires as high-capacity cathode materials for aqueous zinc-ion batteries,” *Ionics (Kiel)*, vol. 30, no. 9, pp. 5279–5289, Sep. 2024, doi: 10.1007/s11581-024-05667-2.

[13] E. Fuentes-Mendoza, M. Talari, E. Zemlyanushin, R. Cordoba, N. Sabi, and S. Dsoke, "Navigating the Challenges of Rechargeable Aluminum Battery Research: Material Instabilities, Technical Hurdles, and Future Directions," *ChemElectroChem*, vol. 12, no. 10, p. e202400705, 2025, doi: 10.1002/celc.202400705.

[14] M. Talari *et al.*, "Exploring the possibility of aluminum plating/stripping from a non-corrosive Al(OTf)3-based electrolyte," *Batter. Supercaps.*, vol. 8, no. 8, 2024, doi: 10.1002/batt.202400317.

[15] W. A. Appiah *et al.*, "Unveiling the plating-stripping mechanism in aluminum batteries with imidazolium-based electrolytes: A hierarchical model based on experiments and ab initio simulations," *Chem. Eng. J.*, vol. 472, Sep. 2023, doi: 10.1016/j.cej.2023.144995.

[16] K. V. Kravchyk, C. Seno, and M. V. Kovalenko, "Limitations of Chloroaluminate Ionic Liquid Anolytes for Aluminum-Graphite Dual-Ion Batteries," Feb. 14, 2020, *American Chemical Society*. doi: 10.1021/acsenergylett.9b02832.

[17] Z. Yu, Z. Kang, Z. Hu, J. Lu, Z. Zhou, and S. Jiao, "Hexagonal NiS nanobelts as advanced cathode materials for rechargeable Al-ion batteries," *Chem. Commun.*, vol. 52, pp. 10427–10430, 2016, doi: 10.1039/c6cc05974k.

[18] J. Yu *et al.*, "Pencil-Drawing Graphite Nanosheets: A Simple and Effective Cathode for High-Capacity Aluminum Batteries," *Small Methods*, vol. 6, no. 4, Apr. 2022, doi: 10.1002/smtd.202200026.

[19] M.-C. Lin *et al.*, "An ultrafast rechargeable aluminium-ion battery," *Nature*, vol. 520, no. 7547, pp. 324–328, 2015, doi: 10.1038/nature14340.

[20] K. L. Ng, B. Amrithraj, and G. Azimi, "Nonaqueous rechargeable aluminum batteries," Jan. 19, 2022, *Cell Press*. doi: 10.1016/j.joule.2021.12.003.

[21] N. Jayaprakash, S. K. Das, and L. A. Archer, "The rechargeable aluminum-ion battery," *Chem. Commun.*, vol. 47, no. 47, p. 12610, 2011, doi: 10.1039/c1cc15779e.

[22] S. Liu, J. J. Hu, N. F. Yan, G. L. Pan, G. R. Li, and X. P. Gao, "Aluminum storage behavior of anatase TiO2 nanotube arrays in aqueous solution for aluminum ion batteries," *Energy Environ. Sci.*, vol. 5, no. 12, p. 9743, 2012, doi: 10.1039/c2ee22987k.

[23] B. Scrosati, "History of lithium batteries," *J. Solid State Electrochem.*, vol. 15, no. 7–8, pp. 1623–1630, Jul. 2011, doi: 10.1007/s10008-011-1386-8.

[24] NobelPrize.org, "The Nobel Prize in Chemistry 2019."

[25] R. Korthauer, *Lithium-Ion Batteries: Basics and Applications*. 2017. [Online]. Available: www.vde.com/institute

[26] Y. Miao, P. Hynan, A. Von Jouanne, and A. Yokochi, "Current li-ion battery technologies in electric vehicles and opportunities for advancements," Mar. 20, 2019, *MDPI AG*. doi: 10.3390/en12061074.

[27] G. Castellan, *Fundamentos de Físico Química*. 1974.

[28] A. J. Bard and L. R. Faulkner, *Electrochemical methods : fundamentals and applications*, 2nd ed. 2001.

[29] EC-lab, “What are SOC and SOH of a battery, how to measure them?” Accessed: Jul. 03, 2025. [Online]. Available: https://www.biologic.net/topics/battery-states-state-of-charge-soc-state-of-health-soh/

[30] N. Schlüter, P. Novák, and D. Schröder, “Nonlinear Electrochemical Analysis: Worth the Effort to Reveal New Insights into Energy Materials,” *Adv Energy Mater*, vol. 12, no. 21, Jun. 2022, doi: 10.1002/aenm.202200708.

[31] S. M. Bak, Z. Shadike, R. Lin, X. Yu, and X. Q. Yang, “In situ/operando synchrotron-based X-ray techniques for lithium-ion battery research,” Jul. 01, 2018, *Nature Publishing Group*. doi: 10.1038/s41427-018-0056-z.

[32] M. S. Whittingham, “Chemistry of intercalation compounds: Metal guests in chalcogenide hosts,” *Progress in Solid State Chemistry*, vol. 12, no. 1, pp. 41–99, 1978, doi: https://doi.org/10.1016/0079-6786(78)90003-1.

[33] G. Greco, G. A. Elia, D. Hermida-Merino, R. Hahn, and S. Raoux, “A Direct Real-Time Observation of Anion Intercalation in Graphite Process and Its Fully Reversibility by SAXS/WAXS Techniques,” *Small Methods*, vol. 7, no. 6, Jun. 2023, doi: 10.1002/smtd.202201633.

[34] Y. Zhang, S. Liu, Y. Ji, J. Ma, and H. Yu, “Emerging Nonaqueous Aluminum-Ion Batteries: Challenges, Status, and Perspectives,” *Adv. Mater.*, vol. 30, no. 38, 2018, doi: 10.1002/adma.201706310.

[35] P. R. Gifford and J. B. Palmisano, “An Aluminum/Chlorine Rechargeable Cell Employing a Room Temperature Molten Salt Electrolyte,” *J. Electrochem. Soc.*, vol. 135, pp. 650–654, 1988.

[36] H. Wang *et al.*, “Anion-effects on electrochemical properties of ionic liquid electrolytes for rechargeable aluminum batteries,” *J. Mater. Chem. A*, vol. 3, no. 45, pp. 22677–22686, 2015, doi: 10.1039/c5ta06187c.

[37] K. Shahzad and I. I. Cheema, “Aluminum batteries: Unique potentials and addressing key challenges in energy storage,” Jun. 15, 2024, *Elsevier Ltd*. doi: 10.1016/j.est.2024.111795.

[38] J. Bitenc *et al.*, “Electrochemical Mechanism of Al Metal–Organic Battery Based on Phenanthrenequinone,” *Energy Material Advances*, vol. 2021, 2021, doi: 10.34133/2021/9793209.

[39] F. Guo *et al.*, “Active cyano groups to coordinate AlCl2+ cation for rechargeable aluminum batteries,” *Energy Storage Mater*, vol. 33, pp. 250–257, Dec. 2020, doi: 10.1016/J.ENSM.2020.08.016.

[40] S. Wang *et al.*, “High-Performance Aluminum-Ion Battery with CuS@C Microsphere Composite Cathode,” *ACS Nano*, vol. 11, no. 1, pp. 469–477, Jan. 2017, doi: 10.1021/acsnano.6b06446.

[41] S. Wang *et al.*, “A Novel Aluminum-Ion Battery: Al/AlCl3-[EMIm]Cl/Ni3S2@Graphene,” *Adv Energy Mater*, vol. 6, no. 13, Jul. 2016, doi: 10.1002/aenm.201600137.

[42] C. Huang *et al.*, “Ultrahigh Capacity from Complexation-Enabled Aluminum-Ion Batteries with C70 as the Cathode,” *Adv. Mater.*, vol. 36, no. 6, p. 2306244, 2023, doi: 10.1002/adma.202306244.

[43] S. Wang, S. Huang, M. Yao, Y. Zhang, and Z. Niu, “Engineering Active Sites of Polyaniline for AlCl2+ Storage in an Aluminum-Ion Battery,” *Angewandte Chemie - International Edition*, vol. 59, no. 29, pp. 11800–11807, Jul. 2020, doi: 10.1002/anie.202002132.

[44] L. Geng, G. Lv, X. Xing, and J. Guo, “Reversible Electrochemical Intercalation of Aluminum in Mo6S8,” *Chem. Mater.*, vol. 27, no. 14, pp. 4926–4929, Jul. 2015, doi: 10.1021/acs.chemmater.5b01918.

[45] Y. Tong *et al.*, “Cation-synergy stabilizing anion redox of Chevrel phase Mo6S8 in aluminum ion battery,” *Energy Storage Mater*, vol. 37, pp. 87–93, May 2021, doi: 10.1016/j.ensm.2021.01.033.

[46] A. VahidMohammadi, A. Hadjikhani, S. Shahbazmohamadi, and M. Beidaghi, “Two-Dimensional Vanadium Carbide (MXene) as a High-Capacity Cathode Material for Rechargeable Aluminum Batteries,” *ACS Nano*, vol. 11, no. 11, pp. 11135–11144, 2017, doi: 10.1021/acsnano.7b05350.

[47] C. J. Pan *et al.*, “An operando X-ray diffraction study of chloroaluminate anion-graphite intercalation in aluminum batteries,” *Proc Natl Acad Sci U S A*, vol. 115, no. 22, pp. 5670–5675, May 2018, doi: 10.1073/pnas.1803576115.

[48] X. Huang, Y. Liu, C. Liu, J. Zhang, O. Noonan, and C. Yu, “Rechargeable aluminum-selenium batteries with high capacity,” *Chem Sci*, vol. 9, no. 23, pp. 5178–5182, 2018, doi: 10.1039/c8sc01054d.

[49] H. Lei, J. Tu, W. L. Song, H. Jiao, X. Xiao, and S. Jiao, “A dual-protection strategy using CMK-3 coated selenium and modified separators for high-energy Al-Se batteries,” *Inorg Chem Front*, vol. 8, no. 4, pp. 1030–1038, Feb. 2021, doi: 10.1039/d0qi01302a.

[50] H. Zhou, S. Zhu, M. Hibino, and I. Honma, “Electrochemical capacitance of self-ordered mesoporous carbon,” *J Power Sources*, vol. 122, no. 2, pp. 219–223, Jul. 2003, doi: 10.1016/S0378-7753(03)00439-7.

[51] W. Xing *et al.*, “Carbon-encapsulated CoSe nanoparticles derived from metal-organic frameworks as advanced cathode material for Al-ion battery,” *J. Power Sources*, vol. 401, pp. 6–12, Oct. 2018, doi: 10.1016/j.jpowsour.2018.08.079.

[52] T. Cai *et al.*, “Stable CoSe2/carbon nanodice@reduced graphene oxide composites for high-performance rechargeable aluminum-ion batteries,” *Energy Environ. Sci.*, vol. 11, no. 9, pp. 2341–2347, 2018, doi: 10.1039/c8ee00822a.

[53] L. Yao, S. Ju, and X. Yu, “Rational surface engineering of MXene@N-doped hollow carbon dual-confined cobalt sulfides/selenides for advanced aluminum batteries,” *J. Mater. Chem. A*, vol. 9, no. 31, pp. 16878–16888, 2021, doi: 10.1039/d1ta03465k.

[54] Z. Yuan, Q. Lin, Y. Li, W. Han, and L. Wang, “Effects of Multiple Ion Reactions Based on a CoSe2/MXene Cathode in Aluminum-Ion Batteries,” *Advanced Materials*, vol. 35, no. 17, Apr. 2023, doi: 10.1002/adma.202211527.

[55] K. Yuan, P. Hao, X. Hu, J. Zhang, and Y. Zhou, “Experimental and computational studies on S-decorated Ti3C2 MXene as anode material in Li-ion batteries,” *J Mater Sci*, vol. 57, no. 13, pp. 7001–7011, Apr. 2022, doi: 10.1007/s10853-022-06983-6.

[56] J. Liu, Z. Li, X. Huo, and J. Li, “Nanosphere-rod-like Co3O4 as high performance cathode material for aluminium ion batteries,” *J. Power Sources*, vol. 422, pp. 49–56, 2019, doi: 10.1016/j.jpowsour.2019.03.029.

[57] X. Zhang, G. Zhang, S. Wang, S. Li, and S. Jiao, “Porous CuO microsphere architectures as high-performance cathode materials for aluminum-ion batteries,” *J. Mater. Chem. A*, vol. 6, no. 7, pp. 3084–3090, 2018, doi: 10.1039/c7ta10632g.

[58] Parans Paranthaman, G. M. Brown, X. Sun, Jagjit Nanda, Arumugam Manthiram, and A. Manivannan, “A Transformational, High Energy Density Secondary Aluminum Ion Battery,” in *ECS Meeting Abstracts*, 2010. [Online]. Available: http://www.sc.doe.gov/bes/reports/files/EES_rpt.pdf

[59] J. Wei, W. Chen, D. Chen, and K. Yang, “Molybdenum Oxide as Cathode for High Voltage Rechargeable Aluminum Ion Battery,” *J. Electrochem. Soc.*, vol. 164, no. 12, pp. A2304–A2309, 2017, doi: 10.1149/2.0411712jes.

[60] S. Guo, M. Liu, H. Yang, X. Feng, Y. Bai, and C. Wu, “CoSnO3/C nanocubes with oxygen vacancy as high-capacity cathode materials for rechargeable aluminum batteries,” *Green Energy and Environment*, vol. 8, no. 3, pp. 883–892, Jun. 2023, doi: 10.1016/j.gee.2021.11.009.

[61] N. Zhu *et al.*, “Reversible Al3+ storage mechanism in anatase TiO2 cathode material for ionic liquid electrolyte-based aluminum-ion batteries,” *J. Energy Chem.*, vol. 51, pp. 72–80, 2020, doi: 10.1016/j.jechem.2020.03.032.

[62] J. Tu, M. Wang, Y. Luo, and S. Jiao, “Coral-Like TeO2 Microwires for Rechargeable Aluminum Batteries,” *ACS Sustain. Chem. Eng.*, vol. 8, no. 6, pp. 2416–2422, 2020, doi: 10.1021/acssuschemeng.9b06193.

[63] W. A. Appiah, H. Li, J. Lampkin, and J. M. García-Lastra, “Towards understanding aluminum sulfur batteries with imidazolium-based electrolytes: A phenomenological model,” *J Power Sources*, vol. 529, May 2022, doi: 10.1016/j.jpowsour.2022.231254.

[64] B. Tan, T. Lu, W. Luo, Z. Chao, R. Dong, and J. Fan, “A Novel MoS2-MXene Composite Cathode for Aluminum-Ion Batteries,” *Energy Fuels*, vol. 35, no. 15, pp. 12666–12670, Aug. 2021, doi: 10.1021/acs.energyfuels.1c01461.

[65] S. Wang *et al.*, “High-Performance Aluminum-Ion Battery with CuS@C Microsphere Composite Cathode,” *ACS Nano*, vol. 11, no. 1, pp. 469–477, Jan. 2017, doi: 10.1021/acsnano.6b06446.

[66] C. Zhang, X. Yang, L. Chai, W. Zhang, and Z. Li, “Novel Cu1.8Se carbon fiber composite for aluminum-ion battery cathode materials: Outstanding electrochemical performance,” *Compos B Eng*, vol. 249, Jan. 2023, doi: 10.1016/j.compositesb.2022.110411.

[67] H. Lei, M. Wang, J. Tu, and S. Jiao, “Single-crystal and hierarchical VSe2 as an aluminum-ion battery cathode,” *Sustain. Energy Fuels*, vol. 3, no. 10, pp. 2717–2724, 2019, doi: 10.1039/c9se00288j.

[68] C. Zheng, J. Tu, S. Jiao, M. Wang, and Z. Wang, “Sb2Te3 Hexagonal Nanosheets as High-Capacity Positive Materials for Rechargeable Aluminum Batteries,” *ACS Appl. Energy Mater.*, vol. 3, no. 12, pp. 12635–12643, 2020, doi: 10.1021/acsaem.0c02553.

[69] A. VahidMohammadi and Y. Gogotsi, “Passive Components in Next Generation Li-Ion Batteries,” *ECS Meeting Abstracts*, vol. MA2022-01, no. 1, p. 81, Jul. 2022, doi: 10.1149/MA2022-01181MTGABS.

[70] E. Zemlyanushin, B. Schwarz, and S. Dsoke, “Dissolution of Molybdenum Current Collector as Crucial and Undesired Process in Aluminum Batteries,” *J. Power Sources*, vol. 633, p. 236458, 2025, doi: j.jpowsour.2025.236458.

[71] Y. Oh, G. Lee, and Y. Tak, “Stability of Metallic Current Collectors in Acidic Ionic Liquid for Rechargeable Aluminum-Ion Batteries,” *ChemElectroChem*, vol. 5, no. 22, pp. 3348–3352, Nov. 2018, doi: 10.1002/celc.201800892.

[72] L. D. Reed and E. Menke, “ The Roles of V 2 O 5 and Stainless Steel in Rechargeable Al–Ion Batteries ,” *J Electrochem Soc*, vol. 160, no. 6, pp. A915–A917, 2013, doi: 10.1149/2.114306jes.

[73] M. Zunita and Y. J. Kevin, “Ionic liquids as corrosion inhibitor: From research and development to commercialization,” Sep. 01, 2022, *Elsevier B.V.* doi: 10.1016/j.rineng.2022.100562.

[74] S. Wang *et al.*, “Aluminum Chloride-Graphite Batteries with Flexible Current Collectors Prepared from Earth-Abundant Elements,” *Advanced Science*, vol. 5, no. 4, Apr. 2018, doi: 10.1002/advs.201700712.

[75] S. Wang *et al.*, “Aluminum Chloride-Graphite Batteries with Flexible Current Collectors Prepared from Earth-Abundant Elements,” *Adv. Sci.*, vol. 5, no. 4, p. 1700712, Jan. 2018, doi: 10.1002/advs.201700712.

[76] C. Toigo, M. Singh, B. Gmeiner, M. Biso, and K.-H. Pettinger, “A Method to Measure the Swelling of Water-Soluble PVDF Binder System and Its Electrochemical Performance for Lithium Ion Batteries,” *J Electrochem Soc*, vol. 167, no. 2, p. 020514, Jan. 2020, doi: 10.1149/1945-7111/ab68c2.

[77] H. Chen *et al.*, “Exploring Chemical, Mechanical, and Electrical Functionalities of Binders for Advanced Energy-Storage Devices,” Sep. 26, 2018, *American Chemical Society*. doi: 10.1021/acs.chemrev.8b00241.

[78] J. Smajic, A. Alazmi, and P. M. F. J. Costa, “The Role of the Binder/Solvent Pair on the Electrochemical Performance of Aluminium Batteries,” *MRS Adv.*, vol. 4, no. 14, pp. 807–812, 2019, doi: 10.1557/adv.2019.125.

[79] H. Wang *et al.*, “Binder-Free V2O5 Cathode for Greener Rechargeable Aluminum Battery,” *ACS Appl. Mater. Interfaces.*, vol. 7, no. 1, pp. 80–84, 2014, doi: 10.1021/am508001h.

[80] E. Zemlyanushin, A. L. Müller, T. Tsuda, and S. Dsoke, “Side-Reactions of Polyvinylidene Fluoride and Polyvinylidene Chloride Binders with Aluminum Chloride-Based Ionic Liquid Electrolyte in Rechargeable Aluminum-Batteries,” *J. Electrochem. Soc.*, vol. 171, p. 110507, 2024, doi: 10.1149/1945-7111/ad8a93.

[81] Z. Yang *et al.*, “Aqueous Binders Compatible with Ionic Liquid Electrolyte for High-Performance Aluminum-Ion Batteries,” *Chemistry - A European Journal*, vol. 29, no. 22, Apr. 2023, doi: 10.1002/chem.202203546.

[82] Y. Hu *et al.*, “A Binder-Free and Free-Standing Cobalt Sulfide@Carbon Nanotube Cathode Material for Aluminum-Ion Batteries,” *Adv. Mater.*, vol. 30, p. 1703824, 2018, doi: 10.1002/adma.201703824.

[83] G. A. Elia *et al.*, “Polyacrylonitrile Separator for High-Performance Aluminum Batteries with Improved Interface Stability,” *ACS Appl Mater Interfaces*, vol. 9, no. 44, pp. 38381–38389, Nov. 2017, doi: 10.1021/acsami.7b09378.

[84] W. Fu *et al.*, “Enhanced electrochemical performance of aluminum-ion batteries with novel polyimide nanofiber separators,” *Electrochim Acta*, vol. 523, May 2025, doi: 10.1016/j.electacta.2025.145903.

[85] L. Chai, X. Li, W. Lv, G. Wu, W. Zhang, and Z. Li, “Dual Protection Strategy by Constructing MXene-Coated Cu2Se–Cu1.8Se Heterojunction and CMK-3 Modification for High-Performance Aluminum-Ion Batteries,” *ACS Appl. Mater. Interfaces.*, vol. 14, no. 43, pp. 48780–48788, 2022, doi: 10.1021/acsami.2c15189.

[86] J. Qian, F. Sun, and L. Qin, "Hydrothermal synthesis of zeolitic imidazolate framework-67 (ZIF-67) nanocrystals," *Mater. Lett.*, vol. 82, pp. 220–223, Sep. 2012, doi: 10.1016/j.matlet.2012.05.077.

[87] T. S. Mathis *et al.*, "Modified MAX Phase Synthesis for Environmentally Stable and Highly Conductive Ti3C2 MXene," *ACS Nano*, vol. 15, no. 4, pp. 6420–6429, Apr. 2021, doi: 10.1021/acsnano.0c08357.

[88] W. Shao *et al.*, "Core-shell-structured MOF-derived 2D hierarchical nanocatalysts with enhanced Fenton-like activities," *J Mater Chem A Mater*, vol. 8, no. 6, pp. 3168–3179, Feb. 2020, doi: 10.1039/c9ta12099h.

[89] K. Ding *et al.*, "Confined N-CoSe2 active sites boost bifunctional oxygen electrocatalysis for rechargeable Zn–air batteries," *Nano Energy*, vol. 91, Jan. 2022, doi: 10.1016/j.nanoen.2021.106675.

[90] Z. Li, L. Y. Zhang, L. Zhang, J. Huang, and H. Liu, "ZIF-67-Derived CoSe /NC Composites as Anode Materials for Lithium-Ion Batteries," *Nanoscale Res. Lett.*, vol. 14, no. 1, 2019, doi: 10.1186/s11671-019-3194-5.

[91] Z. G. Pi, H. Ye, Z. Han, P. Yu, Z. Yin, and X. Ma, "Promising CoSe2-CNT composite catalyst for efficient photoelectrochemical hydrogen evolution reaction," *Front Mater*, vol. 9, Oct. 2022, doi: 10.3389/fmats.2022.1005221.

[92] A. L. Ryser, D. G. Strawn, M. A. Marcus, J. L. Johnson-Maynard, M. E. Gunter, and G. Möller, "Micro-spectroscopic investigation of selenium-bearing minerals from the Western US Phosphate Resource Area," *Geochem Trans*, vol. 6, no. 1, pp. 1–11, 2005, doi: 10.1063/1.1852751.

[93] J. T. Olegario, N. Yee, M. Miller, J. Sczepaniak, and B. Manning, "Reduction of Se(VI) to Se(-II) by zerovalent iron nanoparticle suspensions," *Journal of Nanoparticle Research*, vol. 12, no. 6, pp. 2057–2068, Aug. 2010, doi: 10.1007/s11051-009-9764-1.

[94] W. A. Appiah *et al.*, "Unveiling the plating-stripping mechanism in aluminum batteries with imidazolium-based electrolytes: A hierarchical model based on experiments and ab initio simulations," *Chemical Engineering Journal*, vol. 472, Sep. 2023, doi: 10.1016/j.cej.2023.144995.

[95] S. Wang *et al.*, "A novel dual-graphite aluminum-ion battery," *Energy Storage Mater*, vol. 12, pp. 119–127, May 2018, doi: 10.1016/j.ensm.2017.12.010.

[96] Z. Li, B. Niu, Y. Liu, J. Li, and F. Kang, "Prelithiation treatment of graphite as cathode material for rechargeable aluminum batteries," *Electrochim Acta*, vol. 263, pp. 68–75, Feb. 2018, doi: 10.1016/j.electacta.2017.12.166.

[97] N. Canever, F. R. Hughson, and T. Nann, "Solid-Electrolyte Interphases (SEI) in Nonaqueous Aluminum-Ion Batteries," *ACS Appl Energy Mater*, vol. 3, no. 4, pp. 3673–3683, Apr. 2020, doi: 10.1021/acsaem.0c00132.

[98] J. Robinson and R. A Osteryoung, “The Electrochemical Behavior of Selenium and Selenium Compounds in Sodium Tetrachloroaluminate Melts,” *J. Electrochem. Soc.*, vol. 16, p. 1202, 1978.

[99] F. Rahide *et al.*, “Modification of Al Surface via Acidic Treatment and its Impact on Plating and Stripping,” *ChemSusChem*, vol. 17, no. 5, Mar. 2024, doi: 10.1002/cssc.202301142.

[100] C. Xu, T. Diemant, S. Zhang, X. Liu, and S. Passerini, “Enhanced Cathode-Electrolyte Interphase for Prolonged Cycling Stability of Aluminum-Selenium Batteries Using Locally Concentrated Ionic Liquid Electrolytes,” *Angewandte Chemie - International Edition*, Apr. 2025, doi: 10.1002/anie.202500041.

[101] R. Fehrmann, N. J. Bjerrum, and H. A. Andreasen, “Critical Evaluation of Chemical and Physical Structural Information,” *inorganic chemistry* , vol. 14, no. 9, p. 706, 1975, [Online]. Available: https://pubs.acs.org/sharingguidelines

[102] T. L. Cottrell, *The Strengths of Chemical Bonds*. 1958.

[103] J. J. Sorensen, E. Tieu, and M. D. Morse, “Bond dissociation energies of diatomic transition metal selenides: ScSe, YSe, RuSe, OsSe, CoSe, RhSe, IrSe, and PtSe,” *Journal of Chemical Physics*, vol. 152, no. 12, Mar. 2020, doi: 10.1063/5.0003136.

[104] C. A. Bishop, “Process Diagnostics and Coating Characteristics,” *Vacuum Deposition Onto Webs, Films and Foils*, pp. 85–128, 2015, doi: 10.1016/B978-0-323-29644-1.00005-0.

[105] C. James, “The residual resistance of metals,” *Phys Educ*, 1967.

[106] B. Fellmuth and C. Gaiser, “Residual resistance ratio as indicator for the influence of impurities on fixed-point temperatures,” *Metrologia*, vol. 58, no. 3, Jun. 2021, doi: 10.1088/1681-7575/abeb56.

[107] V. Palenskis, “New Insight into Electric Force in Metal and the Quadratic Electrical Resistivity Law of Metals at Low Temperatures,” *Metals (Basel)*, vol. 14, no. 5, May 2024, doi: 10.3390/met14050526.

[108] T. Morimoto, T. Inaba, S. Yamazaki, K. Kobashi, and T. Okazaki, “Mechanism of the negative linear temperature coefficient of resistance in defective nanocarbon materials,” *Appl Phys Lett*, vol. 126, no. 17, Apr. 2025, doi: 10.1063/5.0250313.

[109] S. Ramjan, A. Khandelwal, L. S. S. Chandra, and M. K. Chattopadhyay, “Negative temperature coefficient of resistivity due to the itinerant spin fluctuations in metallic V$_{0.3}$Ti$_{0.7}$ alloy,” Mar. 2025, Accessed: Sep. 15, 2025. [Online]. Available: https://arxiv.org/pdf/2503.12245

[110] D. V. Else and T. Senthil, “Strange Metals as Ersatz Fermi Liquids,” *Phys Rev Lett*, vol. 127, no. 8, Aug. 2021, doi: 10.1103/PhysRevLett.127.086601.

[111] P. D. of D. College and OpenStax, “ Resistance and Resistivity,” in *Douglas College Physics 1104 Custom Textbook – Winter and Summer* , 2020.

[112] M. Naguib *et al.*, "One-step synthesis of nanocrystalline transition metal oxides on thin sheets of disordered graphitic carbon by oxidation of MXenes," *Chemical Communications*, vol. 50, no. 56, pp. 7420–7423, Jun. 2014, doi: 10.1039/c4cc01646g.

[113] M. Rahman and M. S. Al Mamun, "Future prospects of MXenes: synthesis, functionalization, properties, and application in field effect transistors," Dec. 11, 2023, *Royal Society of Chemistry*. doi: 10.1039/d3na00874f.

[114] C. Xu, F. Xiong, Y. Wang, J. Nai, and W. Zhang, "Improving the intrinsic activity of ultrathin 2D-2D heterostructures by bridge-bonded Ni-O-Ti ligands for efficient oxygen evolution," *Nanotechnology*, vol. 34, no. 25, Jun. 2023, doi: 10.1088/1361-6528/acc743.

[115] M. Magnuson and L. Å. Näslund, "Local chemical bonding and structural properties in Ti3AlC2MAX phase and Ti3C2Tx MXene probed by Ti1sX-ray absorption spectroscopy," *Phys Rev Res*, vol. 2, no. 3, Sep. 2020, doi: 10.1103/PhysRevResearch.2.033516.

[116] M. R. Lukatskaya *et al.*, "Cation intercalation and high volumetric capacitance of two-dimensional titanium carbide," *Science (1979)*, vol. 341, no. 6153, pp. 1502–1505, 2013, doi: 10.1126/science.1241488.

[117] C. Bizot *et al.*, "Aluminum current collector for high voltage Li-ion battery. Part I: A benchmark study with statistical analysis," *Electrochem commun*, vol. 126, May 2021, doi: 10.1016/j.elecom.2021.107013.

[118] K. Zhang *et al.*, "Properties of CoS 2 /CNT as a Cathode Material of Rechargeable Aluminum-Ion Batteries," *Electron. Mater. Lett.*, vol. 15, p. 3, 2019, doi: 10.1007/s13391-019-00169-0.

[119] M. Naguib *et al.*, "Two-dimensional transition metal carbides," *ACS Nano*, vol. 6, no. 2, pp. 1322–1331, Feb. 2012, doi: 10.1021/nn204153h.

[120] L. Somlyai-Sipos and P. Baumli, "Wettability of Metals by Water," *Metals (Basel)*, vol. 12, no. 8, Aug. 2022, doi: 10.3390/met12081274.

[121] M. Jiang *et al.*, "Challenges and Strategies of Low-Cost Aluminum Anodes for High-Performance Al-Based Batteries," *Adv. Mater.*, vol. 34, no. 2, 2021, doi: 10.1002/adma.202102026.

[122] D. R. Lide *et al.*, "CRC Handbook of Chemistry and Physics Editor-in-Chief."

OFFICE OF THE ELECTROCHEMICAL FAILURE INVESTIGATION UNIT

STRAßE AM FORUM 4

REPORT OF INVESTIGATION BY INVESTIGATION UNIT

DECEDENT Aluminum Battery AGE 20 Cycles

HOME ADDRESS Post-Lithium straße, 2 OCCUPATION Energy storage

TYPE OF DEATH: Thermal Runaway ☐ Electrolyte Leakage ☐
Capacity Fade ☑ Dendritic Short ☐

Investigating Agent: Eliana Fuentes Mendoza

Marks and wounds Cathode material degrades rapidly due to the dissolution and migration of active species. These species deposit on the anode, impeding uniform plating and stripping, ultimately leading to capacity loss.

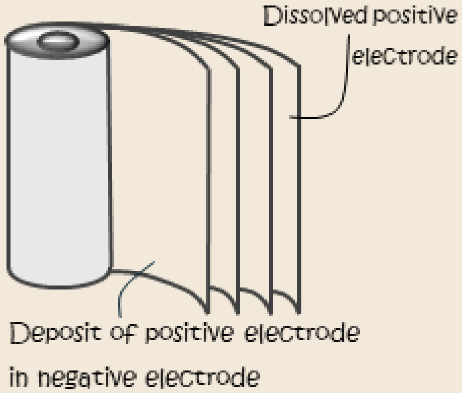

PROBABLE CAUSE OF DEATH	MANNER OF DEATH	DISPOSITION OF CASE
Irreversible Cathode degradation	Check one only Accident ☐ Unknown ☐ Natural ☑ Pending ☐	

I hereby declare that after receiving notice of the battery described herein, I took charge of the cell and conducted a full examination. All findings are true and correct to the best of my knowledge and expertise in electrochemical pathology.

Date	Place of investigation	Signature of Investigating Agent
21.07.2025	KIT	Eliana Fuentes Mendoza